The Dissertation Committee for Ali Afsharpoor Certifies that this is the approved version of the following dissertation:

Pore-Scale Modeling of Viscoelastic Flow and the Effect of Polymer Elasticity on Residual Oil Saturation

Committee:

Matthew Balhoff, Supervisor

Gary Pope

Chun Huh

Roger Bonnecaze

Maša Prodanović

Pore-Scale Modeling of Viscoelastic Flow and the Effect of Polymer Elasticity on Residual Oil Saturation

by

Ali Afsharpoor, B.S.; M.S.P.E.

Dissertation

Presented to the Faculty of the Graduate School of

The University of Texas at Austin

in Partial Fulfillment

of the Requirements

for the Degree of

Doctor of Philosophy

The University of Texas at Austin

December 2014

Dedication

To my lovely parents

Maliheh and Hassan

And to my dear brother

Keivan

Acknowledgements

Accomplishing this study definitely cannot be done without an assistance and support of many individuals. I would like to express my greatest appreciation to my supervisor Dr. Matthew Balhoff for his guidance, kindness, and patience. He was always supportive, encouraging and willing to share his ever more fascinating ideas which were crucial to the success of this work. I would like to thank my dissertation committee, Dr. Gary Pope, Dr. Chun Huh, Dr. Roger Bonnecaze, and Dr. Maša Prodanović for their advices through completion of this study. Financial support of sponsors of the Chemical EOR Industrial Associates Project at The University of Texas at Austin is greatly appreciated.

I am also grateful to Dr. Roger Terzian, Frankie Hart and Heather Felauer for their support to facilitate our academic life at the Petroleum and Geosystems Engineering Department. I would like to extend my gratitude to Joanna Castillo for her assistance with conference posters and presentations in Chemical EOR Joint Industry Affiliation workshop.

I would like to thank you my colleagues in the office 4.132 CPE to make a friendly environments and for their helpful discussions. I explicitly would like to thank Dr. Peixi Zhu, Dan Ehrenfried, Yashar Mehmani, and Daniel Sanchez for their helpful discussion and helps toward accomplishing this study. At the end, I express all my appreciation to my lovely family for the endless love which warms my hearts all the time.

Pore-Scale Modeling of Viscoelastic Flow and the Effect of Polymer Elasticity on Residual Oil Saturation

Ali Afsharpoor, Ph.D.
The University of Texas at Austin, 2014

Supervisor: Matthew T. Balhoff

Polymers used in enhanced oil recovery (EOR) help to control the mobility ratio between oil and aqueous phases and as a result, polymer flooding improves sweep efficiency in reservoirs. However, the conventional wisdom is that polymer flooding does not have considerable effect on pore-level displacement because pressure forces would not be enough to overcome trapping caused by capillary forces. Recently, both coreflood experiments and field data suggest that injecting viscoelastic polymers, such as hydrolyzed polyacrylamide (HPAM), can result in lower residual oil saturation. The hypothesis is that the polymer elasticity provides several pore-level mechanisms for oil mobilization that are generally not significant for purely-viscous fluids. Both experiments and modeling need to be performed to investigate the effect of polymer elasticity on residual oil saturation. Pore-scale modeling and micro-fluidic experiments can be used to investigate pore-level physics, and then used to upscale to the macro-scale. The objective of this work is to understand the effect of polymer elasticity on apparent viscosity and residual oil saturation in porous media.

Single- and multi-phase pore-level computational fluid dynamics (CFD) modeling for viscoelastic polymer flow is performed to investigate the dominant mechanisms at the pore level to mobilize trapped oil. Several interesting results are found from the CFD results. First, the elasticity of the polymer results in an increase in normal stress at the pore-level; therefore, the

normal stresses exerted on a static oil droplet are significant and not negligible as for a purely-viscous fluid. The CFD results show that viscoelastic fluid exerts additional forces on the oil-phase which may help mobilize trapped oil out of the porous medium. Second, due to the elasticity of polymer, the viscoelastic polymer has some level of pulling effect; while passing above a dead-end pore it can pull out the trapped oil phase and then mobilize it. However, both CFD modeling and micro-fluidic experiments show the pulling-effect is not likely the main mechanism to reduce oil saturation at pore-level. Third, dynamic CFD simulations show less deformation of the oil phase while viscoelastic polymer is displacing fluid compared to purely viscous fluid. It may justify the hypothesis that polymer elasticity resists against snap-off mechanism. As a result, when viscoelastic polymer displaces the oil ganglia, , the oil phase does not snap off, and the oil phase remains connected, and therefore easier to move in porous media compared to disconnected oil. For single phase flow, a closed-form flow equation has been developed based on CFD modeling in converging/diverging ducts representative of pore throats. The pore-level equations were substituted into a pore-network model and validated against experimental data. Good agreement is observed.

This study reveals important findings about the effect of polymer elasticity to reduce the residual oil saturation; however, more experiments and simulations are recommended to fully-understand the mobilization mechanisms and take advantage of them to optimize the polymer-flooding process in the field.

Table of Contents

List of Tables

List of Figures

Glossary

D	rate-of-deformation tensor
De	Deborah number
D_p	particle diameter
f	external force vector
f	drag coefficient
g	gravity vector
$G^{/}$	storage moduli
$G^{//}$	loss moduli
H	viscosity level parameter
L	length
K	consistency factor
n	power-law index
N_1	first normal stress difference
N_2	second normal stress difference
p	pressure
Q	flow rate
Re	Reynolds number
S_{or}	residual oil saturation
Sr	recoverable stress
T	extra-stress tensor
T_1	elastic component of extra-stress tensor
T_2	purely-viscous component of extra-stress tensor
T_r	Trouton number
v	velocity vector

v_x	velocity component in x-direction
v_y	velocity component in y-direction
v_z	velocity component in z-direction
We	Weissenberg number
ρ	density
η	viscosity
η_0	zero-shear rate viscosity
η_∞	infinite-shear rate viscosity
η_{max}	infinite-shear rate viscosity
η_E	extensional viscosity
$\dot{\gamma}$	shear rate
λ	relaxation time
λ^*	the longest relaxation time
σ	interfacial tension
σ_{xy}	steady shear stress
ψ_1	first normal-stress coefficient
ψ_2	second normal-stress coefficient
λ_{est}	estimated relaxation time
$\boldsymbol{\varepsilon}$	strain
$\dot{\boldsymbol{\varepsilon}}$	strain rate
η_E	uniaxial extensional viscosity
$\dot{\gamma}_w$	critical shear rate

Chapter 1: Introduction

The flow of viscoelastic fluids in porous media is important in many applications including composite manufacturing in fibrous materials (Skartis et al., 1992; Preziosi et al., 1996), filtration of polymer solutions (Koziki and Kuang, 1994), removal of liquid pollutants in soils (Londergan et al., 2001; Sochi, 2009), blood flow in capillaries (Thurston, 1974; Canic et al., 2006; Rojas, 2007), and enhanced oil recovery (EOR). Polymers are used in enhanced oil recovery (EOR) to control the mobility ratio between displaced fluids (oil) and displacing fluids (water or brine).

Oil recovery from a hydrocarbon-producing reservoir includes up to three phases: primary, secondary, and tertiary recovery (enhanced oil recovery (EOR)). In primary recovery, the driving force to extract hydrocarbon comes from the natural reservoir energy, reservoir natural pressure and reservoir fluid gravity, through these natural forces hydrocarbons are drawn toward the production well and artificial lift techniques (such as pumps) are used to bring the oil to the surface. Depending on the reservoir type and driving force in reservoir, about 10 percent of a reservoir's original oil in place (OOIP) is produced during primary recovery. After the reservoir is depleted with reservoir natural forces, the next phase is secondary recovery which extends the productive life of the reservoir by injecting water or gas to displace oil. Generally, secondary recovery results in an additional 20 to 40 percent of the original oil in place. The final phase is tertiary or enhanced oil recovery (EOR), techniques that offer prospects for ultimately producing 30 to 60 percent, or more, of the reservoir's original oil in place. EOR can be categorized in three main groups: thermal, gas and chemical injections. Thermal recovery is used to introduce heat into reservoir and fluids less viscous which can flow easier into production wells including steam injection. In gas injection processes, different gases are injected into the reservoir to maintain the

reservoir pressure and push the fluids towards the producing well. Some gases are miscible with crude oil, such as CO_2, which sweep the reservoir even more. Chemical methods include the injection of chemicals into the reservoir (such as polymer and surfactant) to control the displacing fluid mobility and lower the interfacial tension between phases, respectively.

The high, shear-dependent viscosity of polymers offer several benefits in chemical EOR including high sweep efficiency and reduced pressure drop near wells, making injection easier. Some polymers used, such as hydrolyzed polyacrylamide (HPAM), exhibit strong elastic effects. Viscoelasticity adds some additional challenges to EOR (Seright et al., 2008). For many years, improving sweep efficiency was considered the only significant mechanism to increase the oil recovery using polymer. Recently, however, experimental studies (Wreath, 1989; Lu, 1994; Wang et al., 2001; Huh and Pope, 2008) and field data (Putz et al, 1988; Wang et al., 2001; Huifen et al., 2004) suggest that viscoelastic polymers such as hydrolyzed polyacrylamide (HPAM) improve displacement efficiency as well and reduce the residual oil saturation.

The objective of this work is to model and understand single-phase and multiphase viscoelastic fluid flow in porous media. Flow of viscoelastic polymers has been studied experimentally and numerically in the literature in a succession of contraction-expansion ducts. Strong increase in apparent viscosity, i.e., a thickening behavior has been observed beyond a critical flow rate which is not observed for viscoelastic fluids measured with a laboratory rheometer. The onset and magnitude of this thickening behavior has been shown to be dependent on geometry and fluid properties (Gupta and Sridhar, 1985). The results are interpreted as an increase in extensional viscosity associated with a stretching of the deformable macromolecules (Marshall and Metzner, 1967; Magueur et al., 1985; Wreath, 1989). Extensional flow is a class of flow having the velocity gradient parallel to the flow direction.

Recent experimental works and field data show that in multiphase systems of oil and water-based polymer, the residual oil saturation is often surprisingly low after viscoelastic polymer displacement (Putz et al., 1988; Wreath, 1989; Wang et al., 2001). This contradicts decades of belief that polymer improves the sweep efficiency as a result of mobility reduction mechanism, but does not have any effect on residual oil saturation (Lake, 1988; Sorbie, 1991; Willhite and Green, 1998).

At the pore-scale, capillary forces prevent the non-wetting phase from flowing, cause snap off, and the unconnected oil phase is difficult to mobilize. If the pressure gradient were sufficiently high, the oil droplet would stretch out toward the adjacent pore, squeeze through the constriction, and then flow to the next pore, but it is generally believed the pressure force across the oil droplet in water or polymer flooding is not high enough to overcome the capillary pressure forces (Peters, 2012). Consider a typical water-wet reservoir (contact angle, $\theta = 0°$), relative permeability (k_w) of 100 mD, and a 1 cp viscosity (μ) fluid flowing at a Darcy velocity (v_w) of 1 ft/day and calculated the applied pressure gradient would be less than 0.1 psi/ft. For a typical pore geometry as shown in figure 1.1 with length 50 μm, throat radius of 10 μm, pore body radius of 50 μm, and surface tension (σ) of 30 dynes/ cm, the required pressure gradient to mobilize the residual oil is approximately 4000 psi/ft; about 4-5 orders of magnitude higher than the applied pressure gradient. Using a more viscous fluid (EOR polymers are usually 10-100 cp) would provide additional pressure gradient, but it would still be at least two orders of magnitude less than required to reduce residual oil saturation (Stegemeier, 1974). Figure 1.2 shows a schematic capillary desaturation curve for porous media. The *x*-axis depicts capillary number which is a dimensionless number defined as the ratio of viscous to capillary forces. In flow through the porous medium, to reduce the residual saturation on non-wetting phase, the capillary

number must be increased to a value greater than the non-wetting critical capillary number (~10^{-5}). However, a typical water/polymer-flooding range the capillary number is much less than 10^{-6}, nowhere near the critical value.

Despite these fundamental calculations for viscous flow, some experimental and field observations show viscoelastic polymer flooding in EOR can reduce the residual oil saturation, improving the recovery by an additional 20% (Putz et al., 1988; Wreath, 1989; Wang et al., 2001). A theoretical study is needed to explain these observations and to determine under what (if any conditions) polymer elasticity can help mobilize trapped oil.

In this study, computational fluid dynamics (CFD) modeling of single-phase viscoelastic fluid flow has been performed, and pore-network simulators for single-phase viscoelastic flow have been developed and validated with experiments. CFD modeling for multi-phase viscoelastic and purely-viscous fluids has been performed to either prove or disprove several hypotheses for residual oil saturation (S_{or}) reduction during polymer flooding. The hypothesis of the additional force due the polymer elasticity, and also the polymer pulling effect in dead-end pores has been tested through modeling. In addition, since in experiments, the additional recovery due to polymer elasticity has been observed in secondary flooding rather than tertiary; the hypothesis that viscoelasticity prevents snap off of oil ganglia has been tested using modeling in a single pore and the results are discussed.

In chapter 2 of the dissertation, a background and literature review on viscoelastic fluid flow in porous media and its effect on residual oil saturation are discussed from both an experimental and simulation perspective. Chapter 3 discusses the development of a single-phase pore-network model and compares the network modeling simulation results to experiments. Chapter 4 explains static (steady-state) CFD modeling viscoelastic flow around an oil droplet

and investigates the elasticity of fluid on the stationary oil droplet. Chapter 5 focuses on the pulling-effect mechanism both numerically and experimentally and discusses the CFD simulation of multiphase flow at which both aqueous phase and oleic phase are modeled. Finally, chapter 6 summarizes the findings and conclusions; and recommends the future work for this topic.

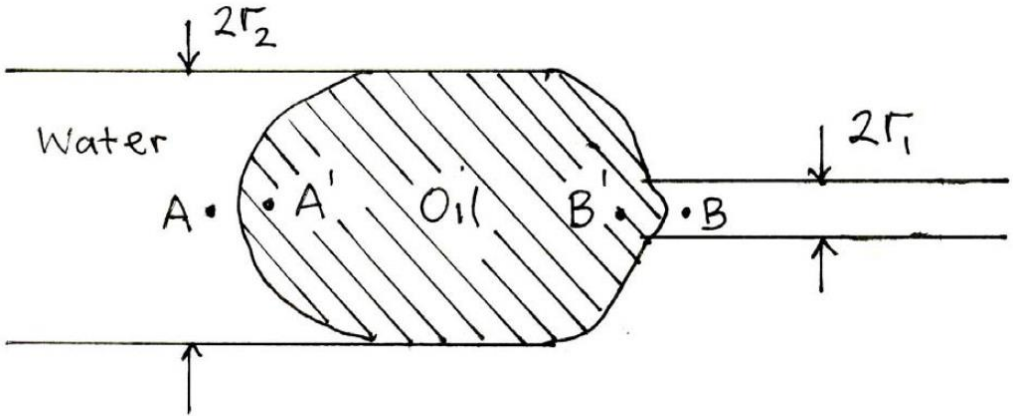

Figure 1.1 Trapped oil blob (Peters, 2012)

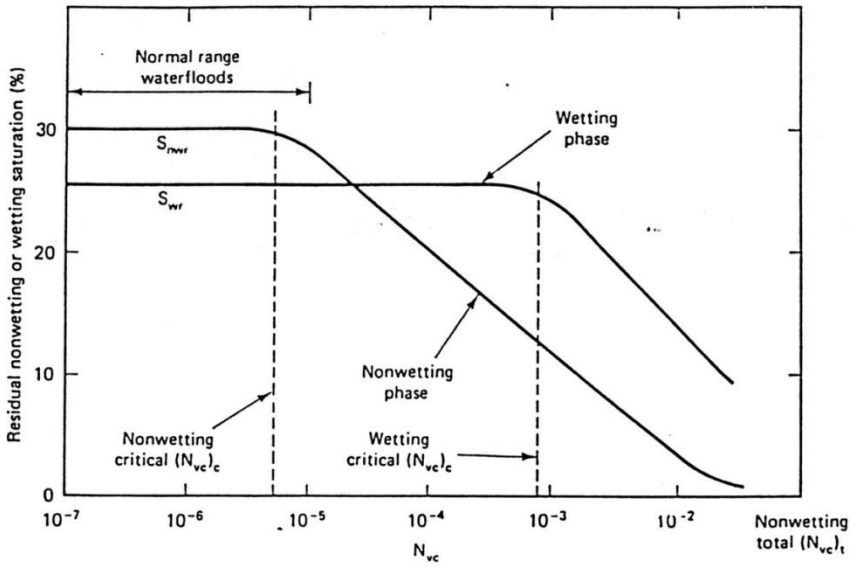

Figure 1.2 Schematic capillary desaturation curve (Lake, 1988)

Chapter 2: Background and Literature Review

Viscoelastic fluids have been studied numerically and experimentally in many applications including those for the oil and gas industry. One of viscoelastic fluid applications in oil and gas industry is for enhanced oil recovery (EOR). In chemical enhanced oil recovery, polymer flooding is a method applied to improve the sweep efficiency in oil reservoirs.

2.1 Non-Newtonian Flow

2.1.1 Rheology and Rheological Models

The proper selection of a fluid rheological model is one of the most important aspects in the simulation of flow of non-Newtonian fluids. One needs to always consider both the fluid and the flow; a particular constitutive equation is valid for a given fluid in a given type of flow.

2.1.1.1 Fluid Rheological Properties

The rheology of a material describes its deformation and affects its flow behavior. Non-Newtonian fluids exhibit shear-dependent viscosity. Several constitutive equations have been proposed to describe the relationship between shear stress (or viscosity) and shear rate for purely viscous fluids such as the power-law (Ostwald, 1925), Carreau (Carreau et al., 1979), and Ellis (Bird et al., 1987) models. As is well known, the range of validity of the Newtonian constitutive equation is limited to low-molecular weight, homogeneous liquids. The flow phenomena observed with polymers, for example, cannot be predicted by the classical Navier-Stokes equations. Non-Newtonian behavior has many rheological complexities such as the shear-rate dependence of the shear viscosity, the presence of normal stresses in viscometric flows, high resistance to elongational deformation, and memory effects associated with the elasticity of the fluid. Non-Newtonian inelastic flows exhibit a shear-rate dependence of the shear viscosity, but other phenomena are characteristics of viscoelastic flows (Bird, 1987; Barnes, 1989).

The momentum equations, the mass conservation (continuity) equation, and (for non-isothermal flows) the energy equation describe the system for both elastic and inelastic fluids. The form of the momentum equations is

$$-\nabla p + \nabla \cdot \boldsymbol{T} + \boldsymbol{f} = \rho \boldsymbol{g} \tag{2.1}$$

where p is pressure, $\boldsymbol{T}$ is extra-stress tensor, $\boldsymbol{f}$ is external force vector acting on fluid, ρ is density, and $\boldsymbol{g}$ is gravity vector. The incompressible continuity equation is

$$\nabla \cdot \boldsymbol{v} = 0 \tag{2.2}$$

where $\boldsymbol{v}$ is velocity vector. In this study all simulations are for isothermal flows, so the energy equation is not necessary (Bird, R., Stewart, W., Lightfoot, E., 2006).

For an inelastic, non-Newtonian fluid, the constitutive equation has the form,

$$\boldsymbol{T} = 2\eta \boldsymbol{D} \tag{2.3}$$

where $\boldsymbol{D}$ is the rate-of-deformation tensor and η is the viscosity which can be function of local shear rate ($\dot{\gamma}$). The local shear rate is defined as

$$\dot{\gamma} = \sqrt{2tr(\boldsymbol{D}^2)} \tag{2.4}$$

In a simple shear flow, $\dot{\gamma}$ reduces to the velocity gradient.

Several constitutive equations are available for inelastic non-Newtonian fluids. First, Newtonian fluids have a constant viscosity (η_0) referred to as the Newtonian or zero-shear rate viscosity, and viscosity is not a function of shear rate as shown in figure 2.1(a).

$$\eta = \eta_0 \tag{2.5}$$

For power-law fluids, viscosity is

$$\eta = K(\dot{\gamma})^{n-1} \tag{2.6}$$

where *K* is the consistency factor, and *n* is the power-law index, which are properties of a given material, the schematic rheological behavior of power-law fluids is shown in figure 2.1(b).

The power law model is commonly used to describe the rheological characteristics of polymers. However, it is not a good model for the entire range of shear rates and it fails at low shear rates. If the behavior at low shear rates is in the range of interest as well, the Bird-Carreau model will capture the plateau zone of the viscosity curve for low shear rates better than the power law.

In the Bird-Carreau model, viscosity is defined as

$$\eta = \eta_\infty + (\eta_0 - \eta_\infty)(1 + (\lambda\dot{\gamma})^2)^{\frac{n-1}{2}} \tag{2.7}$$

where η_∞ is infinite-shear rate viscosity, η_0 is zero-shear-rate viscosity, λ is natural time (i.e., inverse of the shear rate at which the fluid changes from Newtonian to power-law behavior), and *n* is power-law index, the rheology of Bird-Carreau is shown in figure 2.1(c).

2.1.1.2 Flow Rheological Properties

Depending on the kinematics of the system, several types of flow exist: steady simple shear flow, steady extensional flow, oscillatory shear flow, transient shear flow, and transient extensional flow. The first three are discussed here.

<u>Steady Simple Shear Flow</u>

Steady simple shear flow is characterized by a horizontal velocity field, illustrated in Figure 2.2 and defined as follows:

$$v_x = \dot{\gamma} y \tag{2.8}$$

$$v_y = 0 \tag{2.9}$$

$$v_z = 0 \tag{2.10}$$

where v_x, v_y, v_z are velocity component in the *x*, *y*, and *z* direction, respectively, and $\dot{\gamma}$ is the constant shear rate which equals U/h as shown in figure 2.6. To study different flow rheological properties, the following fundamental flow properties need to be defined: steady shear stress ($\sigma_{xy}(\dot{\gamma})$), steady shear viscosity (η), first normal-stress difference (N_1), second normal-stress difference (N_2),first normal-stress coefficient (ψ_1), second normal-stress coefficient (ψ_2), recoverable stress (*Sr*), estimated relaxation time (λ_{est}).

$$\eta(\dot{\gamma}) = \frac{\sigma_{xy}(\dot{\gamma})}{\dot{\gamma}} \tag{2.11}$$

$$N_1(\dot{\gamma}) = \sigma_{xx}(\dot{\gamma}) - \sigma_{yy}(\dot{\gamma}) \tag{2.12}$$

$$N_2(\dot{\gamma}) = \sigma_{yy}(\dot{\gamma}) - \sigma_{zz}(\dot{\gamma}) \tag{2.13}$$

$$\psi_1(\dot{\gamma}) = \frac{N_1(\dot{\gamma})}{\dot{\gamma}^2} \tag{2.14}$$

$$\psi_2(\dot{\gamma}) = \frac{N_2(\dot{\gamma})}{\dot{\gamma}^2} \tag{2.15}$$

$$Sr(\dot{\gamma}) = \frac{N_1(\dot{\gamma})}{2\sigma_{xy}(\dot{\gamma})} \tag{2.16}$$

$$\lambda_{est}(\dot{\gamma}) = \frac{Sr(\dot{\gamma})}{\dot{\gamma}} \tag{2.17}$$

Steady Extensional Flow

Steady extensional flow can be uniaxial, biaxial, or planar. For example, uniaxial extensional flow is illustrated in Figure 2.3 and defined as follows:

$$v_x = \dot{\varepsilon} x \tag{2.18}$$

$$v_y = \frac{-\dot{\varepsilon} y}{2} \tag{2.19}$$

$$v_z = \frac{-\dot{\varepsilon} z}{2} \tag{2.20}$$

where $\dot{\varepsilon}$ is a constant elongational strain rate. The corresponding stress distribution can be written as

$$\sigma_{xx}(\dot{\varepsilon}) - \sigma_{yy}(\dot{\epsilon}) = \sigma_{xx}(\dot{\varepsilon}) - \sigma_{zz}(\dot{\epsilon}) = \dot{\epsilon}\eta_E(\dot{\epsilon}) \tag{2.21}$$

$$\sigma_{xy}(\dot{\epsilon}) = \sigma_{xz}(\dot{\epsilon}) = \sigma_{yz}(\dot{\epsilon}) = 0 \tag{2.21}$$

where η_E is the uniaxial extensional viscosity.

Oscillatory shear flow

It is often needed to examine the response of a viscoelastic material to a small-amplitude oscillatory shear rate. This flow allows one to investigate the linear viscoelastic behavior of the material, and yields the storage and loss moduli, G' and G''. In a viscoelastic fluid, the storage module (G') represents the elastic behavior of the fluid by amount of energy stored in the material, and the loss module (G'') represents the viscous behavior of the fluid by amount of energy which is dissipated as heat. The storage and loss moduli, G' and G'', are obtained from a dynamic frequency test. The dynamic frequency test is a technique used to study the fluid behavior, specifically viscoelastic polymer. In this method, stress applies on the fluid and then the strain in the fluid will be measured; the results interpret the elastic behavior of the fluid.

2.1.1.3 Viscoelastic Models

For viscoelastic fluids the total stress tensor consists of $\boldsymbol{T_1}$ (elastic component) and $\boldsymbol{T_2}$ (purely viscous component). $\boldsymbol{T_1}$ is different for various viscoelastic models depending on which physics are added to the model.

$$\boldsymbol{T} = \boldsymbol{T_1} + \boldsymbol{T_2} \tag{2.22}$$

Each viscoelastic model defines $\mathbf{T_1}$ differently. $\mathbf{T_2}$ is computed from equation 2.23 and for some viscoelastic models is an optional component since it is negligible compared with the $\boldsymbol{T_1}$ component for viscoelastic fluid when the elastic effect is significant.

$$\boldsymbol{T_2} = 2\eta_2 \boldsymbol{D} \tag{2.23}$$

where $\boldsymbol{D}$ is the rate-of-deformation tensor and η_2 is the viscosity factor for the Newtonian (i.e., purely viscous) component of the total stress tensor. The viscoelastic models are categorized in three different classes (Roylance, 2001).

First, the Upper-Convected Maxwell (UCM) and Oldroyd-B models are the simplest viscoelastic constitutive equations; they incorporate a constant viscosity and are usually used when little information exists about the rheology or only qualitative analysis is needed. The Oldroyd-B model is a good option for high extensional viscosity and includes purely-viscous stress component, however in the UCM model, the purely-viscous stress component is neglected. In fact, the UCM is the Oldroyd-B model without purely-viscous component of stress. Eqn. 2.24 is the Upper-Convected Maxwell model used in this study given by,

$$\boldsymbol{T} + \lambda\left(\frac{\partial}{\partial t}\boldsymbol{T} + \boldsymbol{v}\cdot\nabla\boldsymbol{T} - \left((\nabla\boldsymbol{v})^T\cdot\boldsymbol{T} + \boldsymbol{T}\cdot(\nabla\boldsymbol{v})\right)\right) = 2\eta\boldsymbol{D} \tag{2.24}$$

where $\boldsymbol{v}$ is fluid velocity. The purely viscous component of the total tensor ($\mathbf{T_2}$) is zero for the UCM model (i.e., $\mathbf{T}=\mathbf{T_1}$ and $\mathbf{T_2}=0$); however it computed for Oldroyd-B model from equation 2.23. The constitutive equation assumes linear elasticity. Although most real fluids are non-linear, the model is widely used to gain physical insight to viscoelastic behavior because of its relative simplicity.

Second, the White-Metzner, Phan-Thien-Tanner (PTT), Johnson-Segalman, and Giesekus models are more complex; they include a shear-thinning viscosity in the viscous component of

the model. By conducting shear viscosity experiments, these models would be able to model the shear-thinning behavior of polymers and can be used when shear-degradation is modeled. With the White-Metzner model, it is possible to reproduce shear-thinning features. When experimental data are available for the shear viscosity and the first normal-stress difference, the material parameters for the White-Metzner model can be obtained easily by curve fitting. Although it is interesting to capture shear-thinning behavior, the White-Metzner model may encounter some difficulty in its numerical behavior at high shear rates (Bird et al., 1987). In the White-Metzner model, the relaxation time (λ) and the viscosity (η) can be constant or represented by the power law or the Bird-Carreau law for shear-rate dependence. The Phan-Thien-Tanner (PTT), Johnson-Segalman, and Giesekus models are the most realistic viscoelastic models. In particular, they exhibit shear thinning and a non-quadratic first normal-stress difference at high shear rates (Guenette, 1995).

Third, the FENE-P, POM-POM and Leonov models are based on molecular theories and are good models for dilute solutions. The POM-POM model was specifically proposed for branched polymers. More complex viscoelastic models can capture more complexities (Inkson et al., 1999; Clemeur et al., 2003). FENE-P (Finitely Extensible Non-Linear Elastic Dumbbells – Peterlin) model is derived from molecular theories and is based on the assumption that the material behaves as a series of dumbbells connected by springs. The FENE-P model requires only four parameters. It predicts a realistic shear thinning of the fluid and a first normal-stress difference that is quadratic for low shear rates. It has been observed in practice that viscometric properties of several fluids can often be accurately modeled. The FENE-P model is appropriate for simulating the rheological behavior of dilute solutions (Chambers, 1992). POM-POM model was introduced by McLeish and Larson (1998). The concept of the pom-pom structural

molecules makes the model suitable for describing the behavior of branched polymers. From the point of view of morphology, Leonov model is a good choice for macromolecules which are rest and trapped by particles of carbon black, via electrostatic van der Waals forces (Leonov, 1992; Simhambhatla, 1994 and 1995). Leonov model is capable of modeling trapped and free molecules.

2.1.2 Viscoelasticity

Viscoelastic fluids have a memory and partially return to their initial state after deformation. To determine an appropriate model for a problem, one needs to first collect as much data as possible about the fluid properties. Typical information includes (1) steady viscometric properties (shear viscosity η and first normal-stress difference N_1). These data characterize the fluid in the presence of large deformations, (2) oscillatory viscometric properties (storage and loss moduli G' and G'') they correspond to small deformations, and (3) elongational viscosity. In addition to the characteristic time of fluid which is important to study a fluid dynamics problem, studying the characteristics of the flow is required as well. In many situations, the flow can be characterized by a critical shear rate ($\dot{\gamma}_w$) at which elasticity of viscoelastic fluid becomes significant and shear-thickening behavior observed. For example, in a planar flow shown in figure 2.4, the critical shear rate ($\dot{\gamma}_w$) defined as

$$\dot{\gamma}_w = \frac{3Q}{L^2} \tag{2.25}$$

where Q is flow rate and L is a characteristic length.

In addition to flow behavior and geometry, quantification of the fluid elasticity is necessary. This can be investigated by evaluation of the fluid's characteristic relaxation time. When the oscillatory functions storage and loss moduli (G' and G'', respectively) are available,

their intersection ($\dot{\gamma}_i = \frac{1}{\lambda_{estimated}}$ as shown in figure 2.5) is a reasonable choice for selecting a relaxation time. For shear rates below $\dot{\gamma}_i$, flow is dominated by viscous forces; however viscoelastic effects play an important role in shear rate region higher than $\dot{\gamma}_i$. Importantly, due to the technological limitations of some rheometers, it is not always possible to obtain viscoelastic data in the range of shear rates where the fluids flow. In this case, the only option is to extrapolate experimental data for higher shear. The selection of a particular model for such a case will be more qualitative due to lack of rheometer data.

Relaxation time is a fluid property that controls the fluid elastic behavior; it is the time fluid relieves stress under constant strain. The reason the polymer elasticity is obtained in porous media is due to small transit time of polymer solution compared with relaxation time (Sorbie, 1990). To quantify the elasticity of the fluid, a dimensionless group called Deborah number is defined (Metzner et al., 1966)

$$De = \frac{fluid\ relaxation\ time}{flow\ charactristic\ time} = \frac{\lambda}{t_{flow}} \tag{2.26}$$

As *De* number increases, the flow becomes more elastic, meaning the solid-like behavior is more dominant than viscous fluid behavior. *De* number is defined as the ratio of elastic forces to viscous forces. Several definitions have been proposed for Deborah number (Metzner et al. 1966; Jones et al. 1987; Choi 1991; Choi & Kim 1992; Rubinstein and Colby 2003). At large *De*, first normal stress differences play an important role in flow behavior. Extensional viscosity dominates over shear viscosity (Macosko, 1994). This increased (extensional) viscosity is often attributed as the cause of the apparent shear thickening behavior observed in converging/diverging geometries, such as porous media. Measurement of extensional viscosity is

historically difficult (Makosko, 1994) but advanced rheometers (Solomon and Muller, 1996; Sridhar et al., 1991) have been developed to estimate extensional effects.

Another typical dimensionless number (related to Deborah number) used in the literature to estimate the viscoelastic character of a flow is the Weissenberg number (*We*). Deborah and Weissenberg numbers are not different conceptually; different authors name either of those for the product of relaxation time by typical shear rate. *"We"* is the product of the relaxation time (λ) and a typical shear rate $\dot{\gamma}$.

$$We = \lambda\dot{\gamma} \tag{2.27}$$

When *We* is low, inelastic non-Newtonian models are sufficient to describe the flow; only at higher values of *We* are viscoelastic models required to characterize memory effects. A high value of *We* means that a problem is difficult to solve numerically, because of the nonlinear nature of the system.

Several researchers use the longest relaxation time (λ^*) for λ. However, the longest relaxation time (λ^*) can be used to represent non-Newtonian behavior; the relaxation time is changeable with shear rate in a porous medium. Using the longest relaxation time can overestimate Deborah number at given shear rate. Normal stress difference is the evidence of viscoelastic behavior for polymer solution. The relaxation time can be estimated from normal stress difference (Rubinstein & Colby 2003; Choi 1991; Choi & Kim 1992).

$$\lambda \cong \frac{N_1}{2\dot{\gamma}\tau} = \frac{N_1}{2\eta\dot{\gamma}^2} \tag{2.28}$$

Therefore for different for geometry models, *De* number defined as below. First, for a capillary bundle model

$$De = \frac{N_1}{2\eta\dot{\gamma}^2}\dot{\gamma}_{eff} = \frac{N_1}{2\eta\dot{\gamma}_{eff}} = \frac{N_1}{2\tau} \tag{2.29}$$

where τ is shear stress. Second, for a single pore throat

$$t_{flow} = \frac{\varepsilon}{\dot{\varepsilon}} \tag{2.30}$$

where ε is strain and $\dot{\varepsilon}$ is strain rate, therefore Deborah number defined as

$$De = \frac{N_1 \dot{\varepsilon}}{2\eta \dot{\gamma}^2 \varepsilon} \tag{2.31}$$

And Jones (1987) proposed

$$\dot{\gamma} = C_1 \dot{\varepsilon} \tag{2.32}$$

Therefore,

$$De = \frac{N_1}{2C_1 \eta \dot{\gamma} \varepsilon} = \frac{N_1}{2C_1 \varepsilon \tau} \tag{2.33}$$

The solid-like elasticity exhibited in tortuous porous media at which fluid experiences compression and expansion while travelling through converging/diverging pore structure. As a result, fluid undergoes normal stress (stretches stress) in addition to shear stress. The thickening behavior depends on both shearing and stretching mechanism. The proportionality between extensional and shear viscosity is defined as Trouton number.

$$T_r = \frac{\eta_E}{\eta} \tag{2.34}$$

Where η_E is extensional viscosity and η is shear viscosity. Extensional (or elongational) viscosity is a viscosity when applied stress is normal stress. In opposite shear viscosity is a viscosity coefficient when applied stress is shear stress. For a Newtonian fluid which the viscosity is not shear dependent, the Trouton number is 3. Since the extensional viscosity depends on strain rate ($\dot{\varepsilon}$) and shear viscosity on shear rate ($\dot{\gamma}$) for non-Newtonian fluids. In general terms, the Trouton number is defined as

$$T_r = \frac{\eta_E(\dot{\varepsilon})}{\eta(\dot{\gamma})} \tag{2.35}$$

Jones et al. (1987) advocated using of equation 2.5 for Trouton number, since a value of 3 was obtained for all inelastic fluids and any departure from the value 3 corresponding to viscoelasticity.

$$T_r = \frac{\eta_E(\dot{\varepsilon})}{\eta(\sqrt{3}\dot{\varepsilon})} \tag{2.36}$$

Note that the Deborah number (or equivalently Weissenberg number) is probably not the best indicator for viscoelastic models with several relaxation times or if there is shear thinning in the flow. In such cases, a useful dimensionless number is the recoverable shear *Sr* defined as the ratio of the first normal-stress difference $N_1$to twice the steady shear stress σ_{xy}.

$$Sr = \frac{N_1(\dot{\gamma})}{2\sigma_{xy}(\dot{\gamma})} \tag{2.37}$$

2.2 Single Phase Flow in Porous Media

2.2.1 Experimental Observations

Some polymers, such as hydrolyzed polyacrylamide (HPAM), exhibit elastic effects which lead to shear-thickening behavior at high shear rates. Magueur et al. (1985) studied the flow of dilute viscoelastic polymer solutions in successive contractions and expansions (as shown in figure 2.6) and evaluated the effect of converging/diverging geometry on polymer rheology. They experimentally demonstrated shear-thickening behavior for a number of tests and were able to correlate it with several geometric properties. They reported an abrupt increase in apparent viscosity beyond a critical flow rate. They observed the geometry (e.g.; number of contraction-expansions, ratio of length to radius of constricted geometry) and polymer properties have an effect on the onset of shear-thickening behavior. They observed for the geometry in figure 2.6 that the shear-thickening behavior is more pronounced as the ratio between length and

radius of the capillary decreases (figure 2.7). They suggested that shear thickening was due to end effects. They analyzed the reason to increase elongational viscosity of polymer solution is governed by stretching of the deformable macromolecules.

Later Chauveteau and Moan (1981) and Chauveteau (1986) extended the work of Maguer et al. (1985) to investigate the relationship between macromolecular properties and flow behavior of high molecular weight, water-soluble polymer solution through porous media. For high deformation rate flow, thickening behavior was interpreted at a molecular level and shown to depend on stretched molecule to pore size ratio. Figure 2.8 compares the apparent viscosity as a function of shear rate for various contraction-expansion configurations; they observed as the ratio of maximum radius to minimum radius increases, or more successive converging-diverging sections added to the geometry, the fluid shows more shear-thickening behavior. Figure 2.9 shows the effect of polymer concentration on thickening behavior. They show as the polymer concentration increases the shear-thickening behavior is larger. In addition, the effect of salinity on thickening properties has been studied. As shown in figure 2.10, as the salinity increases the critical shear rate at which the thickening begins are delayed. However there is a thickening region which is believed to be originating from the dominance of extensional flow over shear flow at high rate of strain. This behavior is observed in tortuous porous media and the geometry of converging-diverging shape shown in figure 2.11.

During core flood experiments, the pressure calculated across the core and apparent viscosity is calculated with Darcy's equation. For low shear rate (and therefore low flow rates) Newtonian behavior is observed followed by shear-thinning response, and at high enough flow rate eventually the pressure build-up and shear-thickening behavior exhibited is as shown in

figure 2.11. This behavior results from the stretch-relaxation transition of the polymer molecules as they flow through the converging-diverging pore structures in tortuous porous media.

Dauben et al. (1967) investigated the elastic properties of polymers experimentally. They showed the secondary normal stress difference is much smaller than primary normal stress difference. They reported that viscoelastic polymers show shear-thinning behavior in a laboratory rheometer, but in the core-flood experiments, at high flow rate, the flow resistance is higher due to the interaction of polymer molecule and the walls and fluid elasticity in porous media. Several other authors observed the same behavior (Sadowski, 1963; Park, 1972; Yuan, 1981; Vogel and Pusch, 1981; Balhoff and Thompson, 2004; Huifen et al., 2004).

2.2.2 Modeling and Theoretical Considerations

A threshold value of Deborah number exists beyond which viscoelasticity effect plays an important role and below which the flow is mainly viscous. However, Heemskerk and Rosmalen (1984) indicated that the threshold Deborah number can only be used to give a first estimate of the onset of shear thickening behavior because of the difficulty in evaluating the stretch rates that exists in a porous medium. Gupta and Shidhar (1985) also concluded that viscoelastic behavior cannot be predicted by *De* alone but also by the ratio of maximum and minimum diameters of pore structure. They showed the pore geometry is important in examining viscoelastic behavior of fluid flow.

Heemskerk and Rosmalen (1984) showed that the steep increase in pressure beyond a specific flow rate is a direct consequence of viscoelasticity with respect to the unsteadiness of the flow field in a porous medium. They concluded that the onset of shear thickening in terms of critical flow rate shifts towards higher values with increasing permeability, temperature and

salinity and with decreasing molecular weight and polymer concentration at which polymer has less elastic behavior.

Many constitutive equations have been proposed for viscoelastic fluids that exhibit strong extensional flow effects to relate shear stress and rate, such as the Maxwell, Phan-Thien-Tanner, Giesekus, and Oldroyd-B models as discussed in detail previously in this chapter. The differences between various viscoelastic models are how they modeled the behavior of purely-viscous fluid and solid-like phenomena.

Figure 2.11 illustrates the rheology of a viscoelastic fluid in a porous medium. At low apparent shear rates, the fluid exhibits a Newtonian plateau followed by the shear-thinning region, and at high shear rate shear-thickening is observed (Magbagbeola, 2008).

Several authors have studied viscoelastic fluids experimentally and numerically. Marshall and Metzner (1967) presented a model for viscoelastic flow. The drag coefficient-Reynolds number relationships for purely viscous laminar flow is

$$f \cdot Re = 1.0 \tag{2.38}$$

where *f* is the drag coefficient, and *Re* is the Reynolds number and they are defined for packed beds and purely viscous non-Newtonian as below (Bird, Stewart, and Lightfoot, 1960):

$$f = \frac{\Delta P D_p \varepsilon^3 \rho}{L G^2 (1-\varepsilon)} \tag{2.39}$$

$$Re = \frac{D_p G^{2-n} \rho^{n-1}}{150 H (1-\varepsilon)} \tag{2.40}$$

where *H* corresponding for a viscosity level parameter and defines as:

$$H = \frac{K}{12}\left(9 + \frac{3}{n}\right)^n (150\, k\varepsilon)^{(1-n)/2} \tag{2.41}$$

where K is usual consistency index, n is power index for power-law fluids, D_p is particle diameter and ε is fraction of void volume. They observed the deviation from the drag coefficient-Reynolds number relationships for a purely viscous fluid at the critical value of *De* which depends on different variables such as homogeneity. They used the *De* number definition for packed beds of spheres as follows:

$$De = \frac{\lambda v}{D_p} \tag{2.42}$$

Where λ is relaxation time, v is interstitial velocity, and D_p is particle diameter. They performed experimental tests in packed beds of spheres and supported the analysis. Wissler (1971) showed using a perturbation analysis that the purely viscous force acting on a converging-diverging section must be multiplied by a factor to account for viscoelastic effects

$$f \cdot Re = [1 + A(De)^2] \tag{2.43}$$

where A is a constant which seems to be of order 10. The proposed correction factor agrees well with experimental data reported by Marshall and Metzner (1967) as shown in figure 2. 12. They predicted shear-thickening behavior in porous media. However, their model was only valid for low *De* and simple geometries. Also, the value of "*A*" was dependent on the geometry and could not be determined *a priori*.

Deiber and Schowalter (1981) used the method of geometric iteration to solve the momentum equations along with Maxwell constitutive model for the fluid rheology in sinusoidal ducts. They observed a higher flow resistance than expected from purely viscous fluids at high flow rate, and this effect is attributed to the fluid elasticity. However, at high enough flow rates secondary flow affects appear. They showed the flow depends on media geometry characteristics defined as aspect ratio (ratio of maximum and minimum radius of the pore throat). Also, they validated their numerical results with experimental work for the same geometry. Later, Gupta

and Sridhar (1985) analytically evaluated the stresses of polymer solutions through a tube having a periodically varying diameter. They found that if the deformation rate is assumed constant, the stress depends not only upon the Deborah number, but also on the aspect ratio.

Khuzhayorov et al. (2000) used a homogenization technique, i.e. upscaling the heterogeneity scale description. They took advantage of following model (equation 2.44) to derive a general filtration law describing the flow of a linear viscoelastic fluid in porous media. However, the model is only valid under low Reynolds and Deborah number.

$$\vec{v} = -\frac{k}{\mu}\left(1 + \lambda\frac{\partial}{\partial t}\right)\overrightarrow{\nabla p} \tag{2.44}$$

Other authors have studied extensional effects of viscoelastic fluids with numerical methods in planar and axi-symmetric contraction/expansions (Rajagopalan, 1990; Fan, 1999; Alves, 2003; Binding et al., 2006; Aguayo, 2010) and reported shear-thickening behavior. In addition, several attempts have been done to overcome convergence issues for this highly nonlinear problem to reach a higher *De* number. For instance, Huang et al. (1995) used Polyflow software to simulate the viscoelastic fluid flow around the sphere placed in cylindrical tube. They used an EVSS (elastic-viscous stress split) as discussed in chapter 4 formulation for stress and unstructured triangle meshing to reach *De* ~ 2.5.

For simplicity, the Upper-Convected Maxwell (UCM) model has been used to describe the rheological properties of polymer solutions. However, this model considers only viscosity and elasticity of a fluid without including the non-Newtonian shear-thinning behavior. Yin et al. (2006) presented a modified Upper-Convected Maxwell (MUCM) model to take into account this property.

Binding et al. (2006) studied the Olydroyd-B model for 4:1 contraction, and 4:1:4 cases and the pressure drop is calculated using Polyflow software for both planar and axisymmetric cases. They used the EVSS formulation for stress calculation. They observed that the pressure drop initially reduces as the elasticity increases. Then as *De* number is further increased, it eventually rises significantly above the Newtonian value. However before Binding, several authors reported the same trend. Webster (2004) conducted the simulations for Olydroyd-B and PTT model and shows linear declining with increasing De. Szabo (1997) studied Olydroyd-B and FENE model and observed the similar result. Cartalos and Piau (1992) study investigated the viscoelastic behavior experimentally and their outcome was in agreement with Binding's work.

Delshad *et al*. (2008) presented the unified apparent viscosity model that can be used for the entire range of apparent shear rate includes Newtonian, pseudo-plastic or shear-thinning and dilatant or shear-thickening regimes. In this model, the apparent viscosity of the polymer is a summation of the shear dominating viscosity and the elongational-dominating viscosity. The Carreau model applied for the shear-dominating viscosity and an empirical model was used to describe the shear-thickening viscosity.

$$\eta = \eta_\infty + \left(\eta_0 - \eta_\infty\right)\left[1+\left(K\dot{\gamma}\right)^2\right]^{\frac{n-1}{2}} + \eta_{\max}\left[1-\exp\left(\left(-\lambda_2\tau_r\dot{\gamma}\right)^{n_2-1}\right)\right] \tag{2.45}$$

where η_∞, η_0, λ, n and α are empirical constants that will be obtained from the Carreau model fit to the polymer's bulk viscosity data. The semi-empirical model shows good agreement with several sets of core-flood data as shown in figure 2.13. However, it is not derived from fundamental physics. The model coefficients can be obtained from fitting to experimental data for a specific polymer and porous medium.

2.3 Multiphase Flow in Porous media

2.3.1 Experimental Observations

Viscoelasticity and extensional viscosity are typically presumed to be responsible for polymer solution behavior in porous media (Sorbie, 1990). Conventional wisdom on the effect polymer viscoelasticity was not recognized as important in terms of microscopic sweep efficiency, but recent researches on polymer viscoelasticity show evidence that residual oil can be changed with the injection of polymer (Wreath 1989; Wang 2000; Wu 2007; Huh and Pope 2008). Kamaraj et al. (2011) describes the effect that residual oil saturation reduction in viscous oils could have on potential recovery of heavy oils. Wu (2007) reports that polymer viscoelasticity can influence oil recovery, including the mobilization of residual oil. Huh and Pope (2008) show that the viscoelasticity of polymer can reduce residual oil saturation in secondary polymer floods, but not in a tertiary mode.

Wreath (1989) conducted core-flood experiments in Berea and Antolini sandstone, and measured the rheological properties of each polymer used in the experiment. Xanthan and HPAM were used in his experiments with different concentrations and salinity in order to investigate a wide range of polymer viscosity and elasticity. Xanthan is a biopolymer produced by the micro-organism *Xanthomonas Compestris* (Sorbie, 1991). Xanthan was chosen by Wreath (1989) in his study because of its low relative elasticity compared with HPAM. In contrast, partially hydrolyzed polyacrylamide (HPAM) is a synthetic chain of acrylamide monomers which partially have been hydrolyzed. HPAM has a complex behavior and shows different rheological behavior at different range of shear rate (Magbagbeola, 2008). HPAM has been used by Wreath (1989) because of its high elastic characteristic in this experimental condition. Wreath (1989) did not observe oil recovery increment in tertiary polymer flooding, however for some

cases, he reported around 6 percentage S_{or} reductions in secondary HPAM flooding in Antolini sandstone.

Wang M. (1995) extended Wreath's (1989) work and conducted more core-floods for light and heavy oil. He reported the S_{or} reduction of around 3% for secondary Xanthan flood compared with about 8% S_{or} reduction for HPAM. For example, in the experiment AN-1 in Antolini sandstone, he reported about 20% reduction in average oil saturation in the cores shown in figure 14. Wang M. (1995) investigates the effect of various parameters in residual oil saturation. He reported the higher the permeability, the more reduction in S_{or} by polymer-flooding, within the experimental range investigated. A polymer slug size of one pore volume is nearly enough to reduce S_{or} to that of a continuous polymerflood. Several other researcher performed experimental results and observe Sor reduction during HPAM secondary flooding, but not in tertiary (Urbissinova, Trivedi, & Kuru, 2010).

Several other papers published on laboratory and field studies have reported S_{or} reduction (Wang et al., 2000 and 2001). Wang et al. (2000, 2001) provides many glycerin and HPAM polymer results in a wide range of viscosity and elasticity by making polymer solution with different polymer concentration and salinity percentage. They reported about 5-8% increment for the glycerin tertiary after waterflood followed by additional 6% increase for HPAM flooding. They performed tertiary polymer flooding with non-elastic glycerin polymer, to reduce the core oil saturation to residual oil saturation and swept the bypassed area. Afterward, they injected viscoelastic HPAM, and observe about 6% more recovery. They claim the additional 6% recovery is due to elasticity of polymer.

They also conducted micro-fluidic experiments and visualized experiments to investigate the effect of viscoelastic polymer in residual oil saturation in pore-scale (Wang et al., 2010). The

main observations from visualized core data are discussed here. First, they categorized the residual oil saturation in three main groups: “Film” type (figure 15 and 16), “Column” type (figure 17), and “Droplet” type (figure 18), and show no matter which type of residual oil saturation is, the additional micro-forces due to polymer elasticity first pushes on the interface between phases and protruding portions of the residual oil blobs. Some of the oil from the interface will move to the protruding portion making the protruding portion bigger (the direction and magnitude of the change in velocity of the driving fluid will also become larger) and with a larger radius (smaller capillary force), the larger pushing force deforms the protruding portion more, and as shown in figures 15-18, after deforming, gets larger and larger until the protruding part detaches from the oil blob and form a new oil droplet that can be driven forward. This process continuous until the oil blob divided into many small movable oil droplets or until oil blob gets too small which forces acting on its protruding portion cannot gather enough oil from behind it to form a shape with enough radius (and small capillary retention force) to form another individual droplet, then the macro and micro driving forces reach an equilibrium with the capillary retention forces, a new smaller oil blob is formed which not movable. The cumulative effect of the above phenomena is to have lower residual oil saturation. Second, it shows that polymer solution pulls out the oil which is trapped in dead-end geometry as shown in figure 2.19. They show interesting results which are very convincing regarding the effect of polymer elasticity on S_{or} reduction, however the details of study are not reported and therefore the experiments are not repeatable.

Wang et al. (2010) performed experiments in weak oil-wet artificial homogenous cores. They showed that only the first normal force differential and its corresponding Weisenberg number (or equivalently Deborah number) affect the shape of the flow lines. Other elastic

properties such as second normal force difference and the viscosity of the driving fluid do not affect flow lines; therefore they do not affect the E_D either. Wang et al. (2010) predicted the capillary number and viscoelasticity both influence the displacement efficiency and residual oil saturation.

Recently, Ehrenfried (2013) conducted a series of core-flood experiments in several different sandstones using displacing fluid with wide range of fluid elasticity from none to those with extremely high relaxation times. He used three different sandstone cores for the core-flood experiments: moderate permeability Berea outcrop rock, Boise sandstone cores with a high degree of heterogeneity, and the homogenous Bentheimer sandstone which has a high permeability. Different types of polymer solution were used in his study including: (1) Glycerin which is a small molecular substance that also exhibits a Newtonian response to shear rate, (2) HPAM polymer solution which is a synthetic chain of acrylamide monomers, some portion of which have been hydrolyzed; HPAM with fairly complex rheology, and (3) Xanthan gum with low elasticity. The results were inconclusive with some experiments showing additional oil recovery which may be due to elastic mechanisms. Most experiments showed no significant difference between elastic and non-elastic floods when experimental parameters were controlled within narrow limits.

Ehrenfried (2013) concludes from his core-flood experiments that viscoelastic polymers may reduce residual oil saturation in water-wet sandstones, but found the results to be difficult to reproduce. Some experimental evidence shows support for an elastic effect. Other evidence either contradicts the premise or showed little difference between elastic and non-elastic displacement fluids. In most cases where results could suggest elastic effects as the cause, alternative explanations for the additional oil recovery are possible. The big challenge is keeping

other parameters constant (except polymer elasticity) to be able to make a conclusion on the effect of the polymer elasticity on residual oil saturation. Variations in fluid rheology, core heterogeneity, initial oil saturation, relative permeability, in-situ viscosity, and in-situ elasticity all change from experiment to experiment. This makes their individual contributions to recovery difficult to isolate.

2.3.2 Modeling Approaches

At the pore-scale, capillary forces play an important role and can prevent the non-wetting phase from flowing. Capillary force by a snap-off mechanism makes the oil phase unconnected and difficult to mobilize. It is believed trapped oil is restricted from being drawn out of the tight pores because the pressure force across the oil droplet in water or polymer flooding is not high enough to overcome the capillary pressure forces. If the pressure gradient were sufficiently high, the oil droplet would stretch out toward the adjacent pore, squeeze through the constriction, and then flow to the next pore. However, it is believed that the additional viscosity of polymers would not provide nearly enough pressure-drop to overcome capillary forces and mobilize a significant amount of residual oil. This is true for a purely viscous Newtonian fluid and can be demonstrated using simple calculations as shown in the introduction (Chapter 1).

Normally, when analyzing driving forces to determine the displacement efficiency (E_D) during flooding, only viscous forces, which are proportional to the macro pressure gradient (*dp/dl*), are considered, and micro forces in pores are neglected because micro forces are negligible compared to macro forces for the fluids without elastic characteristics. There are two important micro forces: first, the normal force caused by the change in shape of the flow lines in pores; second, the kinetic force caused by the change in momentum, which is due to the change in flow lines in pores too. Both of these two micro forces are caused by the change in flow lines,

the larger the change in flow lines, the larger the two micro forces. Analysis, calculations and experiments show that the flow lines in pores are different between viscoelastic and Newtonian fluids. Flow lines in pores of viscoelastic fluids, compared to Newtonian fluids, look more like and "expanding" and "contracting" piston flow. For viscoelastic fluids, micro forces in pores are much larger than that for Newtonian fluids and must be considered when analyzing the displacement efficiency (Wang et al., 2007).

There are a few hypotheses (Wang et al., 2001; Huh and Pope, 2008) to justify the residual oil reduction by viscoelastic polymer flooding such as accelerated drainage of oil films on rock surfaces, scoured oil in dead-end pores, and trapped oil pulled out in stable oil threads as shown in figures 2.15 to 2.19. The fundamental physics of viscoelastic flow at the pore-scale is still not well understood. However, several hypotheses for improved oil recovery are proposed by several authors (Wang et al., 2001; Huh and Pope, 2008). Wang et al. (2000) showed higher molecular weight, and higher concentrations result in higher elasticity. They hypothesized that higher molecular weight causes a reduction in peak velocity, so velocity gradient at the wall increases which results in stripping off oil from the wall. In addition, at the dead-end pore, the elasticity of polymer causes to drag oil from dead-end pores and reduces the residual oil saturation as shown in figures 2.20 and 2.21 (Wang et al., 2010).

Lu (1994) performed history match simulations on the core flood experiments done by Wang M. (1995) in order to understand the primary reasons for the observed increase in oil recovery. He reported a history match in good agreement with the experiments when the S_{or} reduction was applied in the simulations; this implies that the viscoelastic polymer did in fact reduce residual oil saturation. Zhang et al. (2010) developed a viscoelastic model for flow

through porous media and concluded that polymers can increase both the macroscopic and the microscopic sweep efficiencies.

2.3.2.1 Mobilization of Residual Oil Phase

Oil phase will be trapped when the pressure gradient required to mobilize oil phase is not high enough. For a simple geometry shown in figure 1.1, the local pressure gradient required to mobilize the oil blob is given by (Peters, 2012)

$$\frac{P_A - P_B}{L} \geq \frac{2\sigma \cos\theta}{L}\left(\frac{1}{r_1} - \frac{1}{r_2}\right) \tag{2.46}$$

Where P_A is the pressure at point A, P_B is the pressure at point B, σ is interfacial tension, L is the blob length, r_1 and r_2 is the pores radius. As seen in equation 2.46, as the interfacial tension between two phases becomes higher, more pressure gradient is needed to overcome the entry capillary force and mobilize the oil droplet.

Osher and Sethain (1988) developed level-set method for front propagation with curvature dependent speed. Level set methods are numerical techniques to compute the position of propagating interfaces. They rely on an initial value partial differential equation for a propagating level set function. Level set method has been originated for tracking interface by Prodanovic and Bryant (2006) which can handle complicated geometry.

Using the level set method for basic navigation of interface in 2-D works as described below. First, a level set function is defined $\Phi(x, y, t)$ which is a contour of given value of Φ, for instance $\Phi = 0$. It means a set of points such that $\Phi = 0$ for all times. In such a simple case, we assume the interface moves normal to itself at speed F. the speed function is defined such that it accounts for capillary pressure (P_c) and interfacial tension (σ).

$$F = P_c - \sigma\kappa(x, y, t) \tag{2.47}$$

where κ is interface curvature changing with time. The governing partial differential equation (PDE) to control the level set function is as follows:

$$\phi_t + F|\nabla\emptyset| = 0 \tag{2.48}$$

The level set function asymptotically approaches steady-state corresponding to mechanical equilibrium. Steady-state physically means the capillary pressure balances with interfacial tension.

$$F = 0 \rightarrow P_c = \sigma\kappa\,; Young - Laplace\ equation \tag{2.49}$$

2.3.2.2 Free Surface and Free Boundary Tracking

In transient flows of two phases, the movement of an interface occurs. Accurately capturing the interface and tracking the movement and deformation of the free interface is a challenge in all numerical Finite-Element Methods (FEM). In general there are two methods to capture the free surface: Eulerian and Lagrangian methods. We briefly introduce them here.

In Eulerian flow fields and mesh techniques, meshes are stationary and fixed. The mesh nodes are fixed and material flows through the mesh. Eulerian coordinates of nodes are fixed and coincide with spatial points, and spatial coordinate of material points vary with time as shown in figure 2.22.

The material point at a given quadrature point changes with time which makes it difficult to deal with history-dependent materials. Boundary nodes and material boundaries may not coincide. Therefore, boundary conditions and interface conditions are difficult to apply. There is no mesh distortion because the mesh is fixed in space. However, the domain that needs to be modeled is larger compared with Lagrangian approach because the body cannot leave the

domain. In contrast, in Lagrangian flow fields and mesh technique, the mesh is moving and attached to the material as shown in figure 2.23.

Lagrangian coordinate of nodes moves with the material and the material coordinate of material points are time invariant. No material passes through the elements. Element quadrature points remain coincident with material points. More importantly, boundary nodes remain on the boundary in order to keep track of interface more precisely. Therefore, boundary conditions and interface conditions are easily applied. The disadvantage of this method is that severe mesh distortions can occur because the mesh deforms with the material. To overcome the mesh distortion, a re-meshing technique can be applied. The purpose of a re-meshing technique is to relocate internal nodes according to the displacement of boundary nodes. Re-meshing techniques control mesh deformation in order to avoid unacceptable element shapes. There are different re-meshing methods according to the physics of the problem. Elastic re-meshing methods has been selected for this study. The Arbitrary Lagrangian-Eulerian (ALE) method takes advantage of both Lagrangian and Eulerian approaches. The mesh movement is arbitrary to have an optimum shape of element to track the boundaries and interfaces precisely. It can model the wettability; however, it cannot simulate capillary pressure like when a droplet is immersed in another liquid. The limitation of this method is that it is not good for abrupt topology changes and when a single interface divided into multi interfaces. All dynamic (transient) simulations in this study used ALE method (Ansys Polyflow User's Guide, 2012).

2.4 Pore-Network Modeling

2.4.1 Single Phase Flow

To model flow through porous media, CFD (computational fluid dynamics) can be used to solve first-principle equations (e.g. Momentum equations and Continuity equation), and can

give accurate results. Performing CFD modeling for an entire porous medium is computationally expensive and with current computational facilities is not possible especially for viscoelastic flow which is highly non-linear case. An alternative method to study pore-level flow in pores and throats and upscale macroscopic parameters, is pore-network modeling.

Network modeling is a technique to approximate a porous medium as an interconnected network of pores and pore throats. Hence, computational simulation of the network is required to understand the flow behavior of these systems. Network models have been used to study important behavior regarding flow and transport, but were limited to qualitative studies using simple 2-D or 3-D lattices. More recently, Bryant et al., 1993 developed quantitative techniques to model behavior in porous media for single-phase Newtonian flow and Baake and Oren, 1997 developed the multiphase pore-network model. Afterward, Lopez et al., 2003; Balhoff and Thompson, 2004 developed pore-network model for non-Newtonian flows. Physically-representative network models are mapped directly from a rigorous description of some original well-described porous medium (Bryant et al., 2003), and consequently they retain important morphological and spatial correlations necessary for obtaining quantitative and predictive results.

The first step in characterizing the pore structure is to obtain an accurate numerical description of the porous medium. X-ray computed micro-tomography (XMT) (Liang et al., 2000; Lindquist et al., 2000; Al-Raoush et al., 2003) is used to extract the 3-D pore structure of real, naturally occurring media. The high-resolution images obtained through XMT are digitally represented as voxels which (in a binary image) define the pore and grain space. In addition, computer-generated methods offer an alternative to high resolution imaging of porous media as used in this study; however, all of the methodology used for computer-generated pore-network can be applied to image-based networks as well. These methods include stochastic approaches

(Liang et al., 2000; Lindquist et al., 2000; Al-Raoush et al., 2003; Adler et al., 2002) in which the porous medium is reconstructed using statistical properties, and process-based approaches that attempt to simulate the geological process by which the medium was formed. Regardless of the method used to digitally represent the medium, the second step is conversion to a network model of pores and throats. Grain-based methods are usually tied to approaches that represent grain positions in porous media. For example, a Delaunay tessellation (Bryant at al., 1993; Al Raoush et al., 2003) can be used to generate pores and interconnected throats, creating a physically-representative network model. Figure 2.24 illustrates the creation of a physically-representative model from a sphere packing. For voxel data obtained from imaging, the medial-axis (Adler et al., 1992; Lindquist et al., 1996) can be used to thin the void space, from which one can map out the pores and throats in the network.

The generated network model is a digitalized version of the porous media including pores and throats which can be used to simulate many transport problems by requiring mass conservation at every pore and solving fundamental equations of momentum and mass in the connecting throats. Early network modeling done by Bryant et al., 1993; Lopez et al., 2003 assumed pore throats as a simple capillary tubes or transformed the throats into equivalent capillaries. Advancements continue to be made to account for the actual irregular geometry of these throats. Balhoff and Thompson (2004, 2005) uncovered closed-form flow equations for non-Newtonian fluids in converging/diverging ducts (which are more representative of the true throat geometry) by solving the momentum equations numerically. The advancements resulted in up to a 20% change in predicted properties. The goal of predictive network modeling is to upscale macroscopic properties (such as apparent viscosity) that can be obtained without tedious and time consuming experimental tests.

The main approach for pore-network modeling in porous media is to solve the mass conservation equation for each pore and the momentum equation for each throat simultaneously. For a simple case of incompressible and Newtonian fluid, the Hagen-Poiseuille equation has been used as a transport equation for throats.

$$q_{ij} = \frac{g_{ij}}{\mu} \Delta P \tag{2.50}$$

where g is hydraulic conductivity and for capillary tube defined as

$$g_{ij} = \frac{\pi r^4}{8L} \tag{2.51}$$

and the mass conservation for each pore needs to be satisfied.

$$\sum q_{ij} = 0 \tag{2.52}$$

where, $q_{i,j}$ is volumetric flow rate comes to pore i , from neighbor pore j.

The system of equations is linear for incompressible Newtonian fluids; however, it is highly nonlinear for non-Newtonian fluids, specifically for viscoelastic fluids because the volumetric flow rate equation versus pressure drop for pore throats is not linear. The pressure at each pore will be calculated by solving this system of equations; afterward, the flux at each throat can be evaluated.

Most of the network modeling studies of non-Newtonian flow deals with shear-thinning fluids that exhibit no elastic effects. Sorbie and Clifford (1989) modeled the flow of a Carreau fluid using 2-D networks; Shah and Yortsos (1995) extended their work to 3-D networks to model the flow of power-law fluids. They presented qualitative results for the steady flow, which show that flow patterns are more sensitive to the throat-size distribution than for the case of Newtonian fluids. Physically representative networks has been used to model shear-thinning

fluids in porous media, and showed good agreement with existing experimental data (Lopez et al., 2003).

The flow of yield-stress fluids has also been investigated. Sahimi (1993) modeled general nonlinear behavior in square (2-D) and cubic (3-D) networks, which included modeling piecewise linear transport within a network that contained thresholds for bond conductivities. The flow of a Bingham fluid in 2-D pore-networks has been studied by Shah et al. (1995). Balhoff and Thompson (2004) modeled the flow of Bingham fluids in physically-representative networks. They reported the importance of correct pore-throat flow equations which can be capture from FEM modeling. Sochi and Blunt (2008) developed the model for Herschel-Buckley fluid by extending Balhoff and Thompson (2004) work.

Few attempts have been performed using pore-network models for viscoelastic flow in porous media. Recently, Sochi (2009) did model a Bautista-Manero fluid using a network model and qualitatively predicted shear-thickening behavior. They modified the Tardy algorithm (Tardy, 2005) for effect of converging/diverging geometry on the steady state viscoelastic flow. Sochi (2009) used the modified Bautista-Manero model which successfully describes elasticity, thixotropic time dependency and shear-thinning for modeling the flow of viscoelastic materials which also show thixotropic attributes. This is a relatively simple model that combines the Oldroyd-B constitutive equation for viscoelasticity and the Fredrickson's kinetic equation for flow-induced structural changes usually associated with thixotropy. Sochi's work was a qualitative study of viscoelastic flow, they used averaging and simplifications which make it less accurate than solving the equations thoroughly using FEM, which would capture complex physics occurs in viscoelastic flow. Moreover, they did not compare their results to experimental data or extend their work to multiphase flow. The CFD modeling that has been done in this study

leads to capture complex viscoelastic behavior without simplifying the conservation equations, and the obtained universal flow equation for viscoelastic flow leads to reduce the computational cost in pore-network simulations rather than discretizing each pore throat in the pore network model.

2.4.2 Multiphase Network model

Pore-network models for multi-phase flow are categorized into quasi-static and dynamic models. Quasi-static models are mostly used when the capillary effects dominate, and are computationally less expensive than dynamic models. In quasi-steady models, the simulation for a given time is a steady-state problem for an imposed capillary pressure, and time-dependency is not taken into account (Flemming, 1983; Wilkinson and Willemesen, 1983; Heiba, 1984). Through computational advancements, dynamic multi-phase pore-network models have been developed which are more predictive and include more details about the physics of flow. Both viscous and capillary effects are included in this model (Dias and Payatakes, 1986; Al-Gharbi and Blunt, 2005; Joekar-Niasar et al., 2010). In dynamic models, the phase conductivity for each throat is assigned, and the pressure and flow rate is evaluated by solving the system of equations. In addition, development of pore-network models for viscoelastic multi-phase flow is needed to understand the reason for the apparent observed residual oil saturation reduction in polymer flooding.

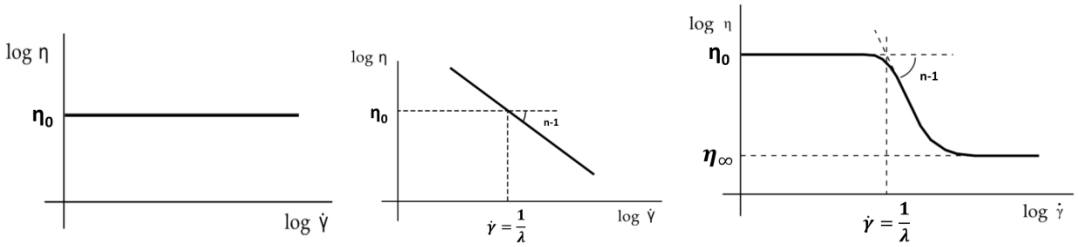

(a) **(b)** **(c)**

Figure 2.1 (a) Newtonian fluid rheology curve, constant (not shear rate dependent) viscosity; (b) Power-law fluid rheology curve; (c) Bird-Carreau fluid rheology curve (Ansys Polyflow User's Guide, 2012)

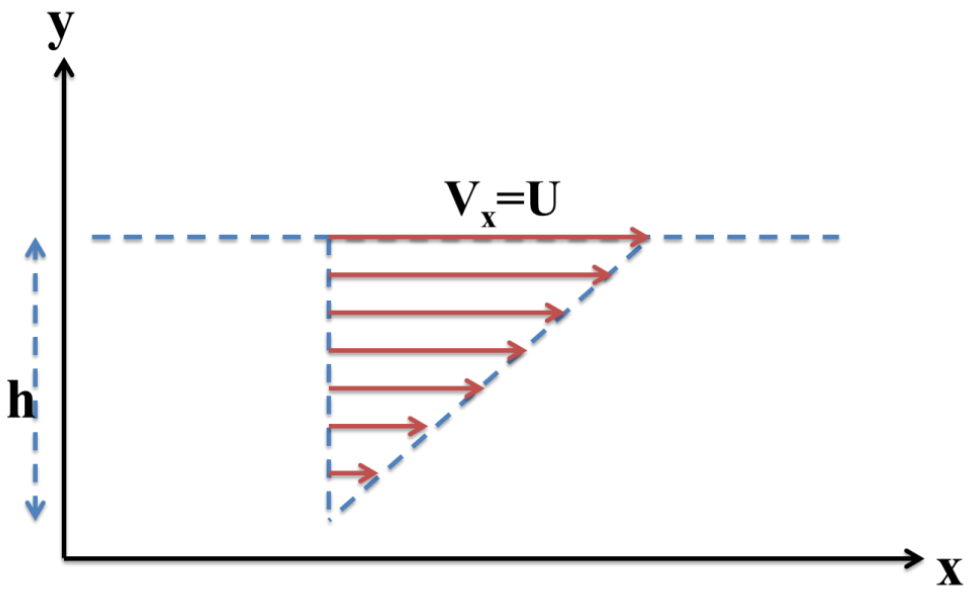

Figure 2.2 Steady simple shear flow

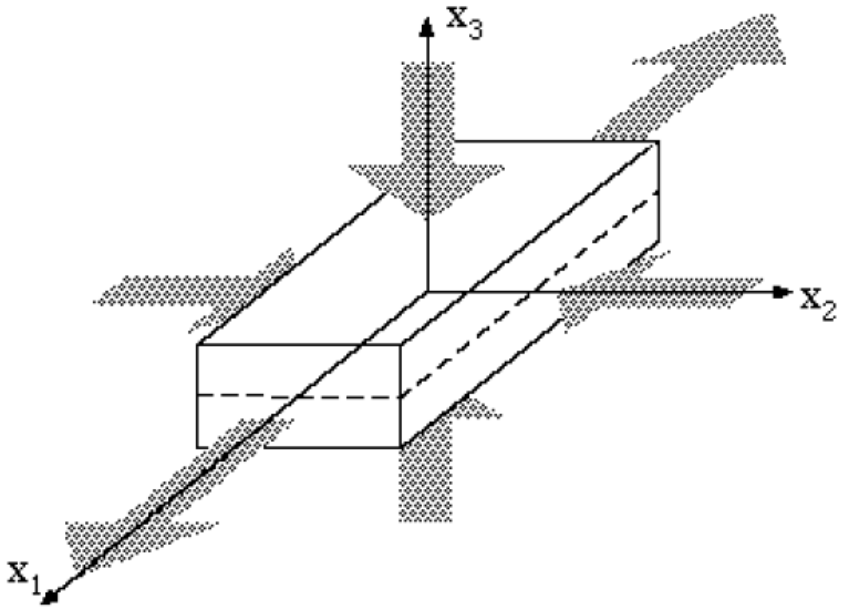

Figure 2.3 Uniaxial extensional flows (Ansys Polyflow User's Guide, 2012)

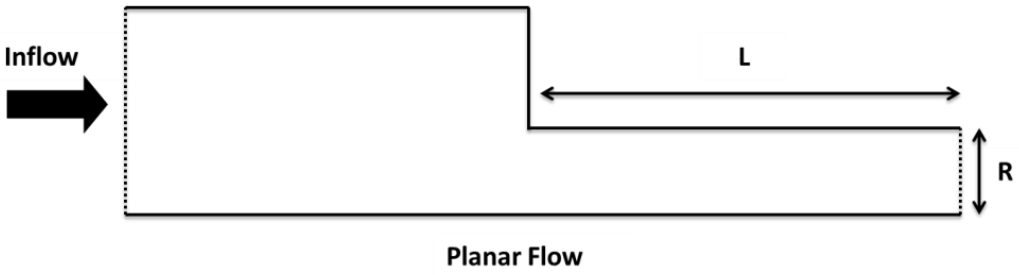

Figure 2.4 Contraction flow

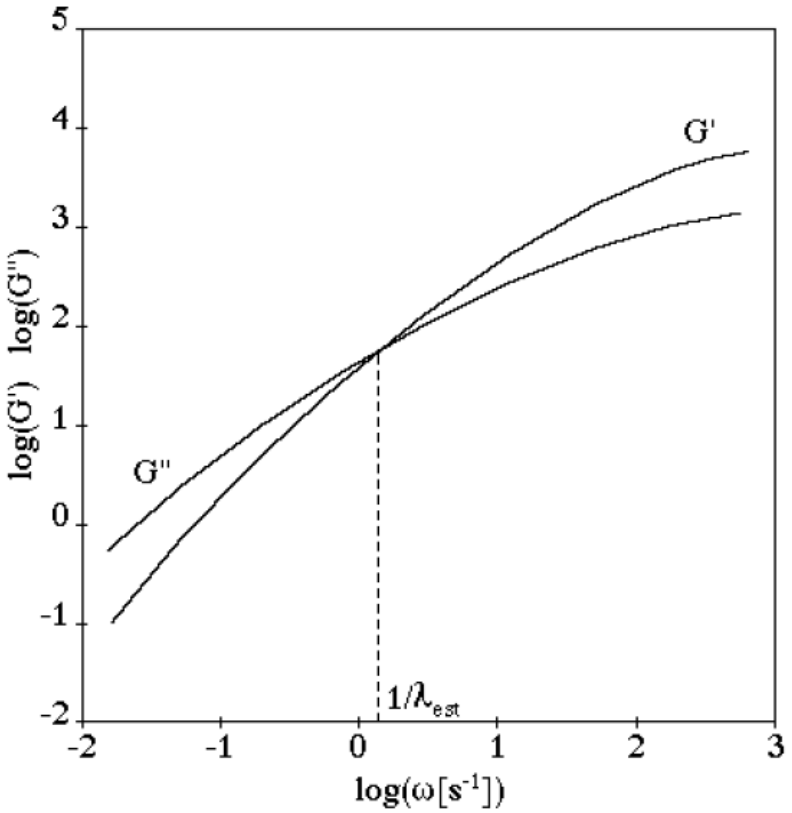

Figure 2.5 Storage and loss moduli curves (Ansys Polyflow User's Guide, 2012)

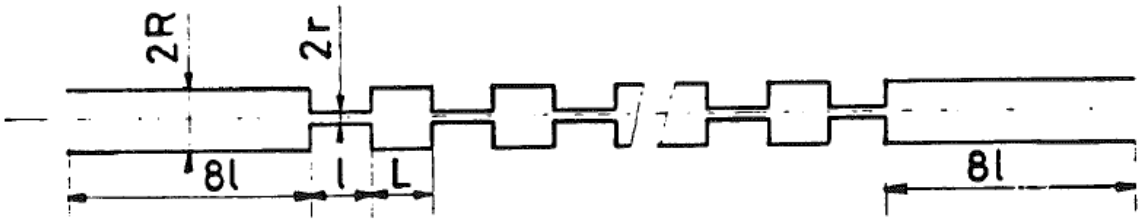

Figure 2.6 Schematic successive contraction-expansion geometry to analyze shear-thickening behavior of viscoelastic polymer (Magueur et al.,1985)

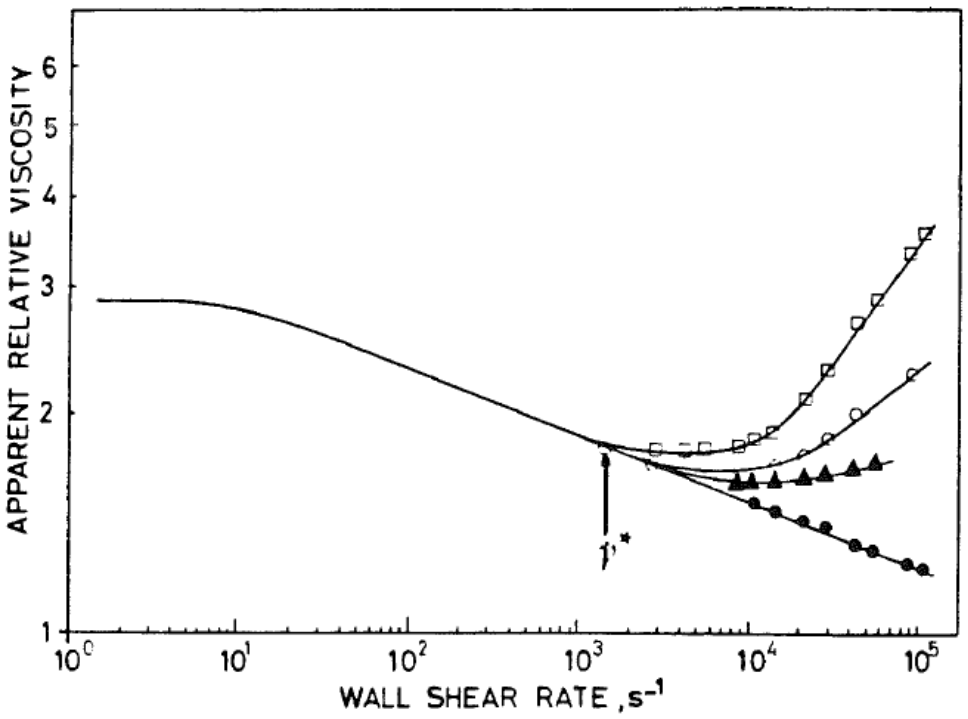

Figure 2.7 Apparent viscosity as a function of shear rate for various length-to-radius of capillary (Magueur et al., 1985)

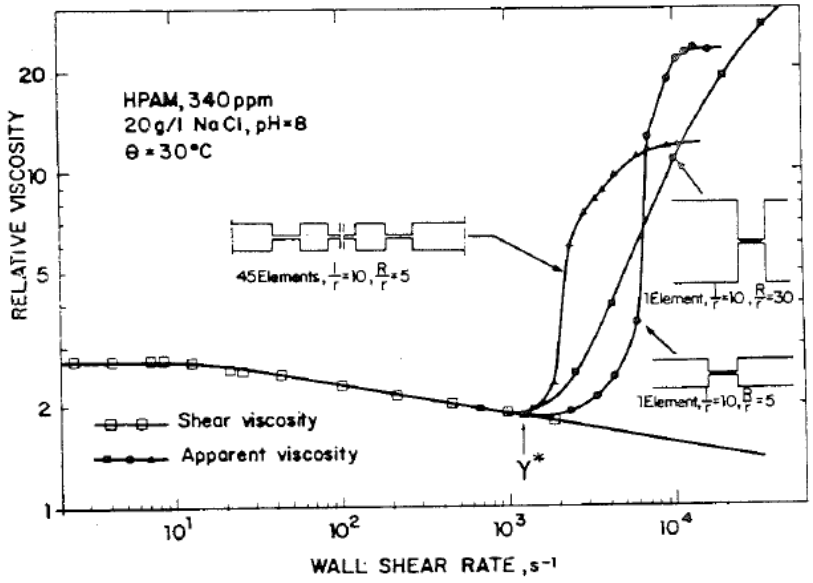

Figure 2.8 Relative viscosities as a function of shear rate for various geometry configurations (Chauveteau, 1986)

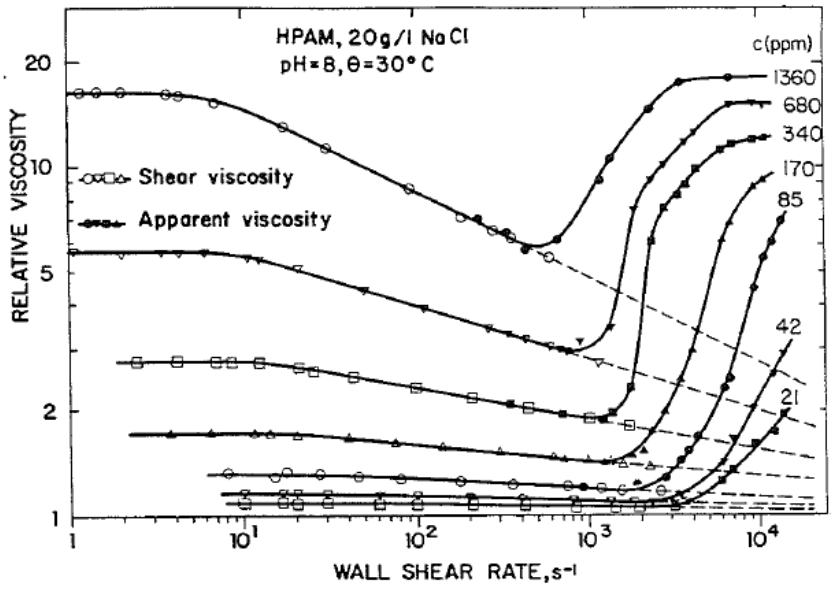

Figure 2.9 Relative viscosities as a function of shear rate for different polymer concentration (Chauveteau, 1986)

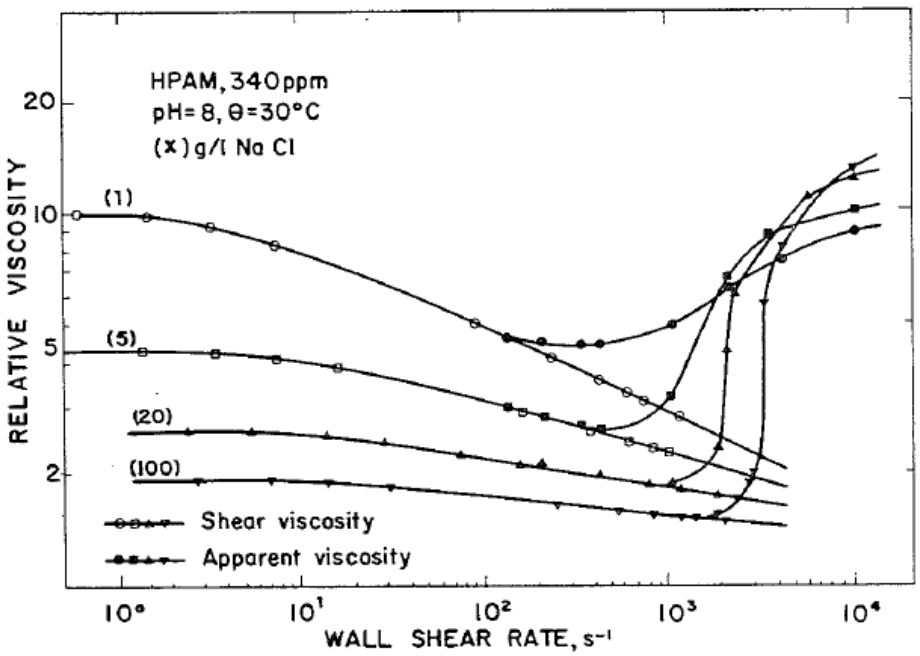

Figure 2.10 Relative viscosities as a function of shear rate for different salinity level (Chauveteau, 1986)

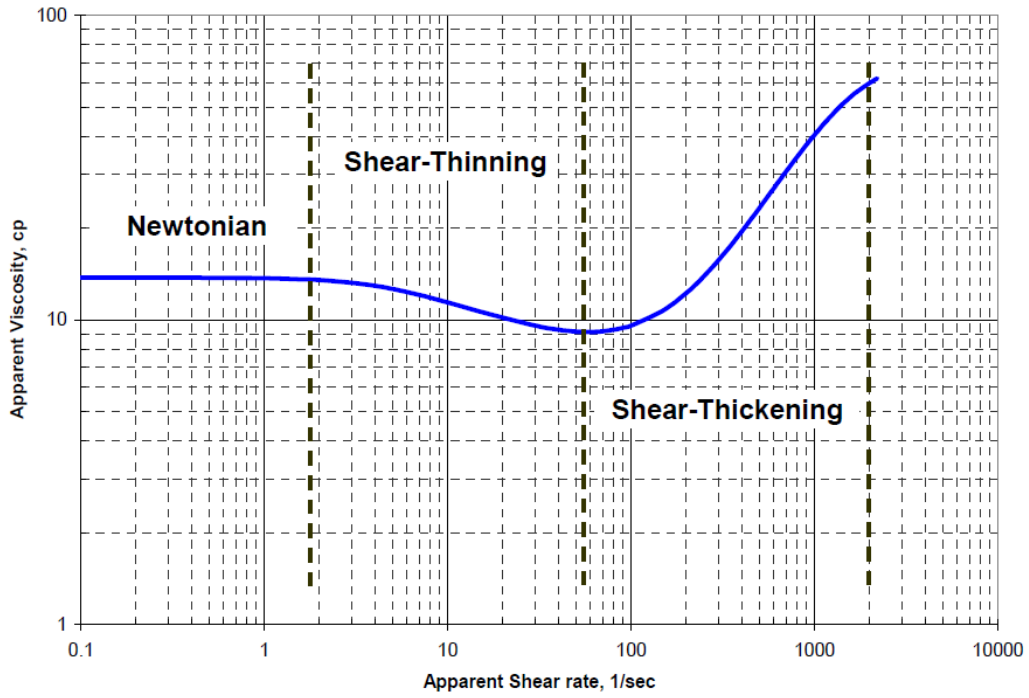

Figure 2.11 Schematic of shear rate dependence of polymer (HPAM) apparent viscosity (Magbagbeola, 2008)

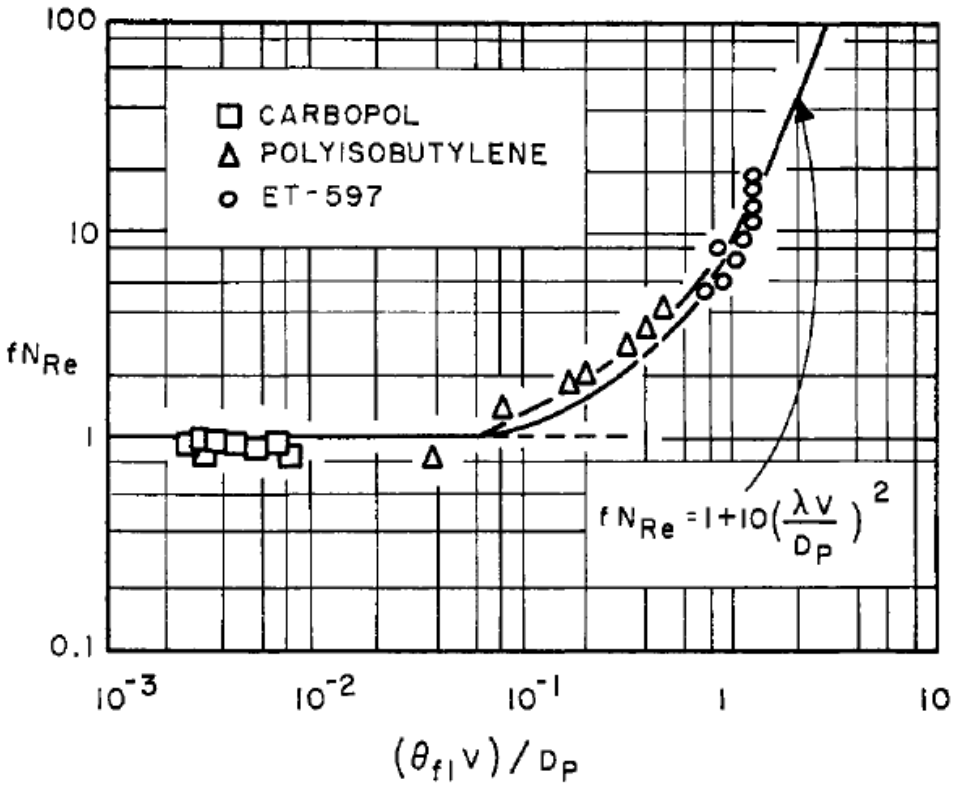

Figure 2.12 Dependence of viscoelastic effect (*f.Re* > 1.0) on the Deborah number, Note: θ_f and λ are relaxation time, only from different references (Wissler, 1971)

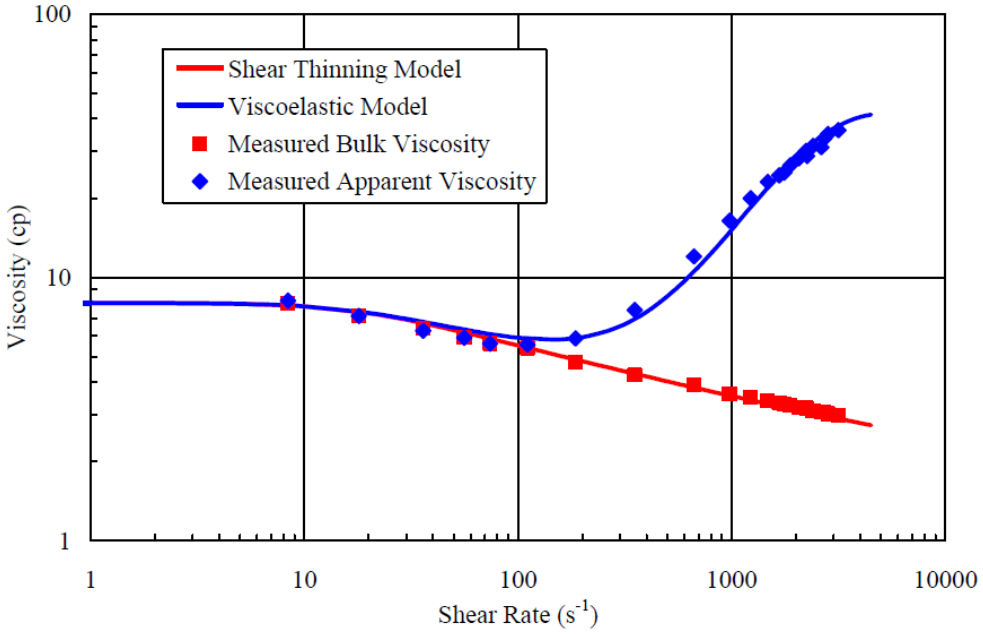

Figure 2.13 Viscoelastic model fit to 1000 ppm Pusher 700in 1% NaCl (Delshad, 2008)

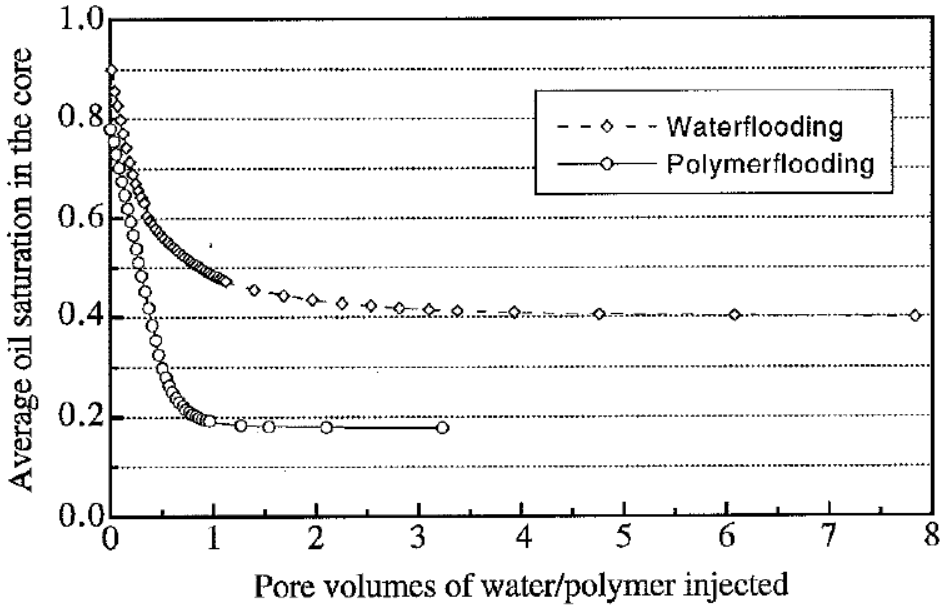

Figure 2.14 Comparison of waterflood and polymerflood, average oil saturation in core as a function of pore volumes of water/polymer injected (Wang M., 1995)

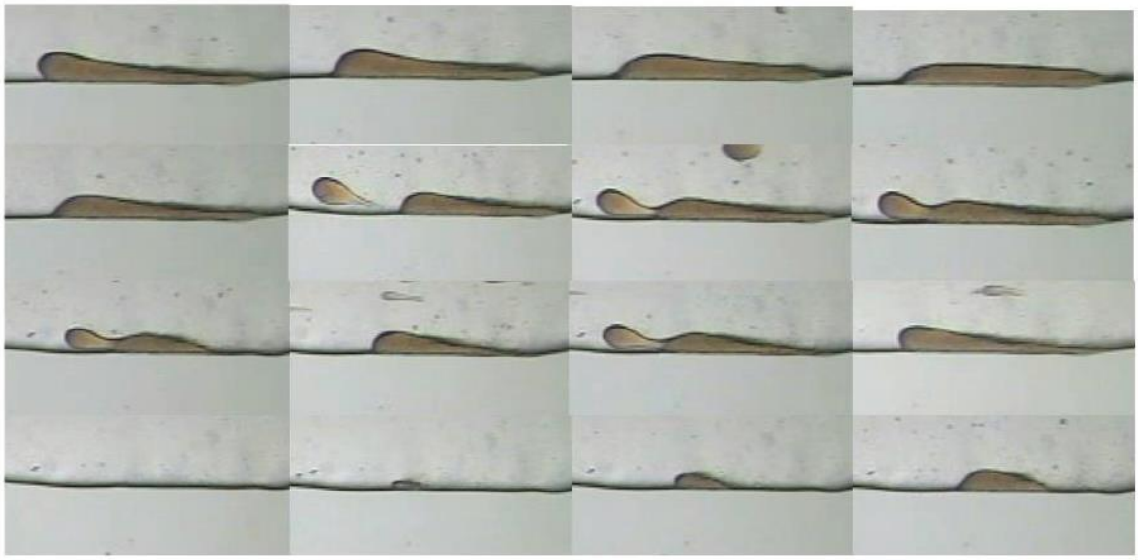

Figure 2.15 Mobilization of film-type residual oil (Wang et al., 2010)

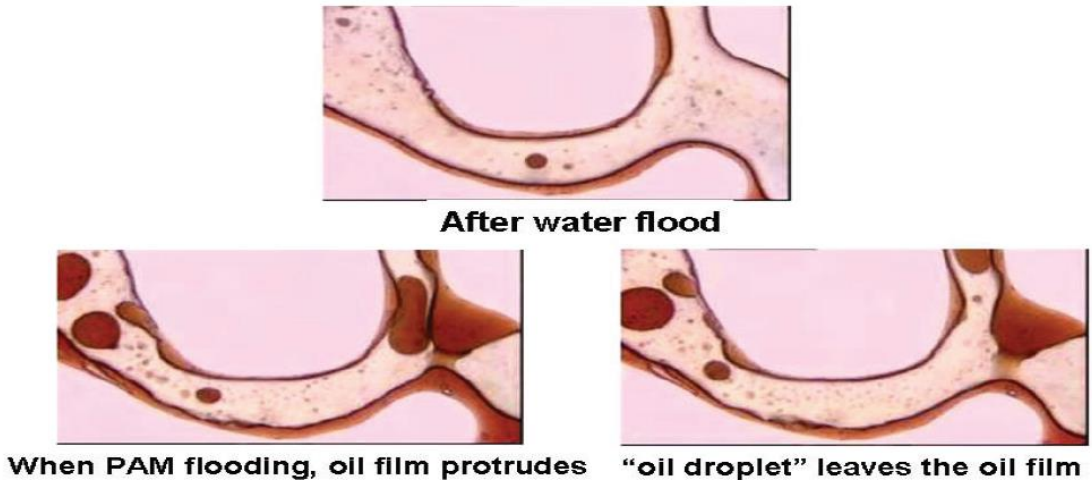

Figure 2.16 Polymer fluid displacing oil-film type residual oil (Wang et al., 2010)

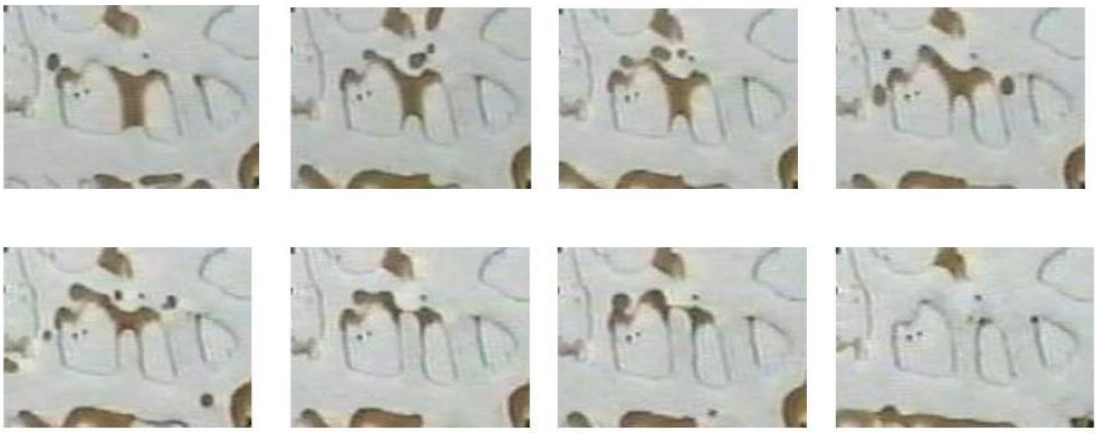

Figure 2.17 Mobilization of column-type residual oil in oil-wet pores (Wang et al., 2010). The flow direction for each snapshots is from botton to top. The sequentioal of snapshotps starts from top row from left to righ, followed by bottom row from left to right.

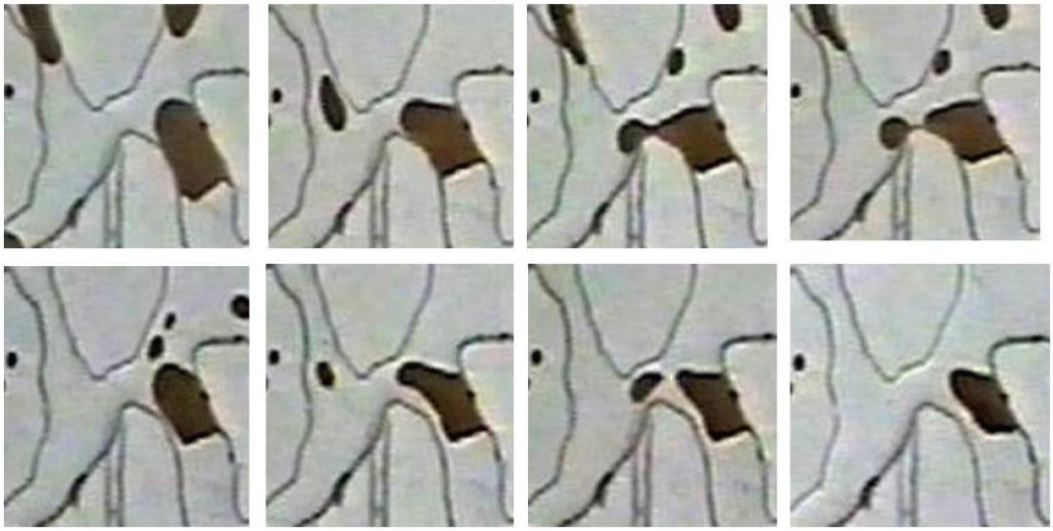

Figure 2.18 Mobilization of oil droplet in water-wet pores (Wang et al., 2010). The flow direction for each snapshots is from botton to top. The sequentioal of snapshotps starts from top row from left to righ, followed by bottom row from left to right.

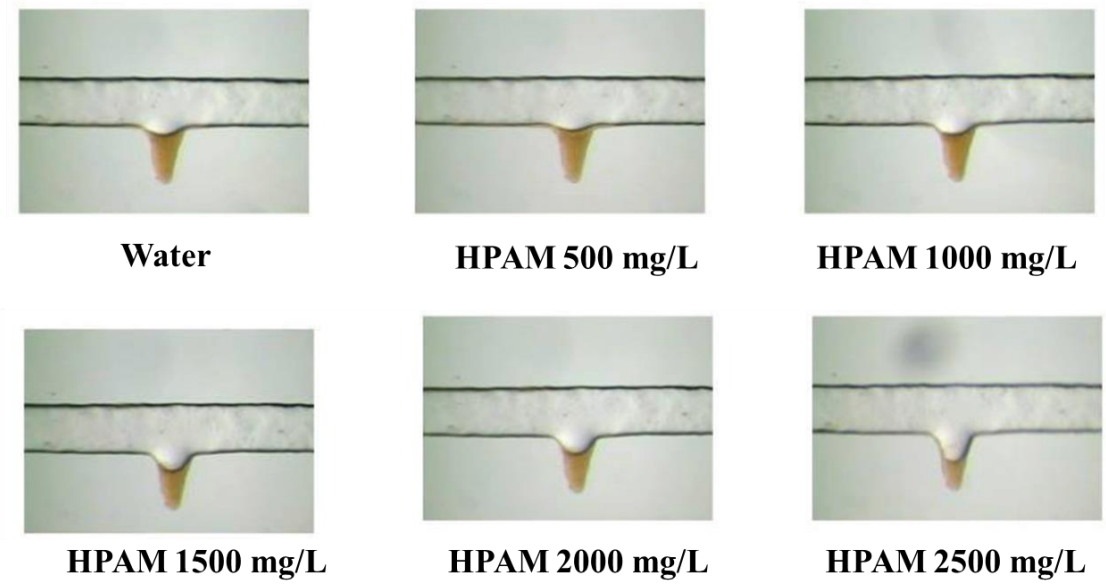

Figure 2.19 Residual oil after continuous flooding by water and HPAM polymer by different concentrations (Wang et al., 2010)

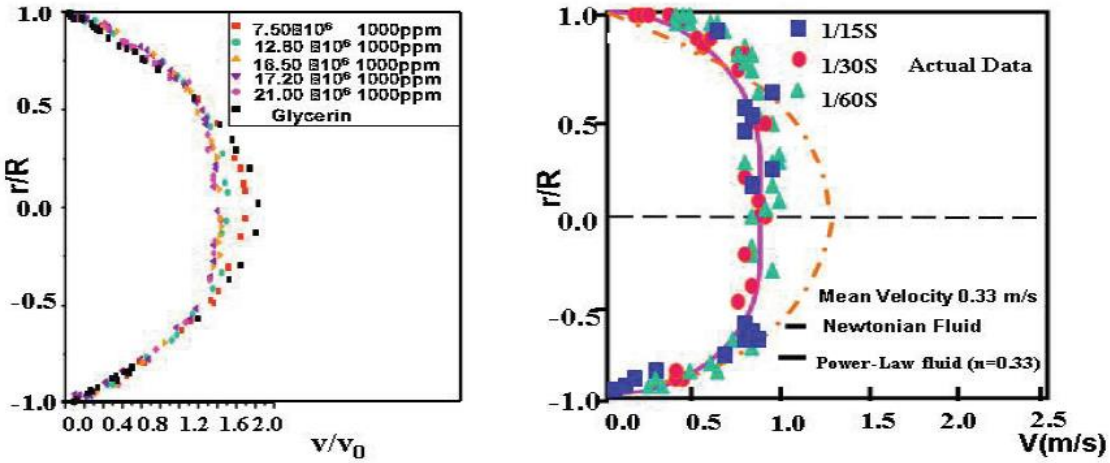

Figure 2.20 Velocity profile of different fluids in micro tube (Wang et al., 2010)

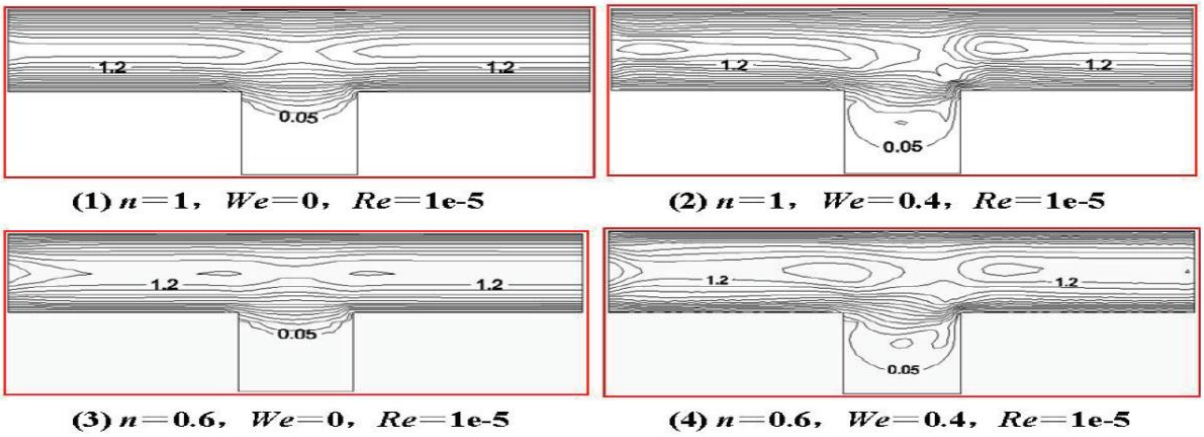

Figure 2.21 The velocity contours of viscoelastic fluid in pores with dead end (Wang et al., 2010)

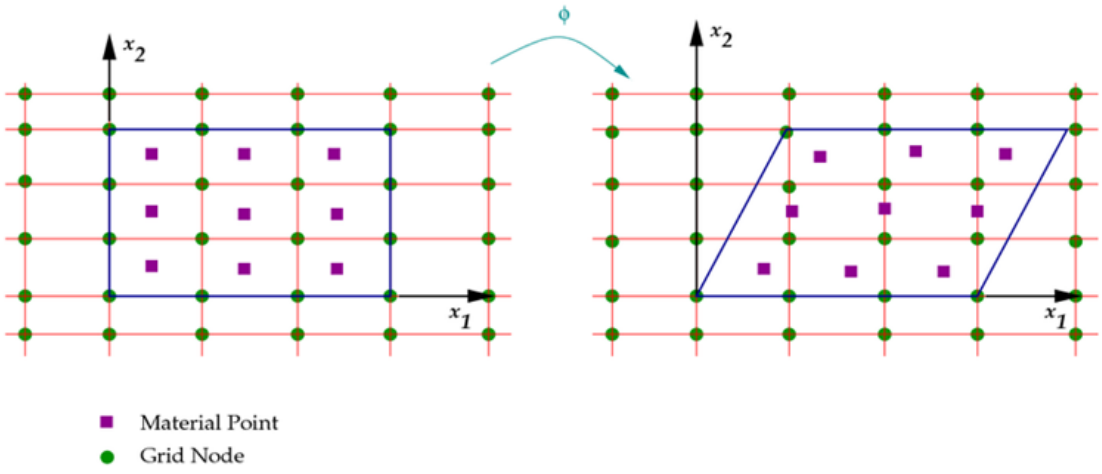

Figure 2.22 Eulerian flow fields and mesh techniques (Ansys Polyflow User's Guide, 2012)

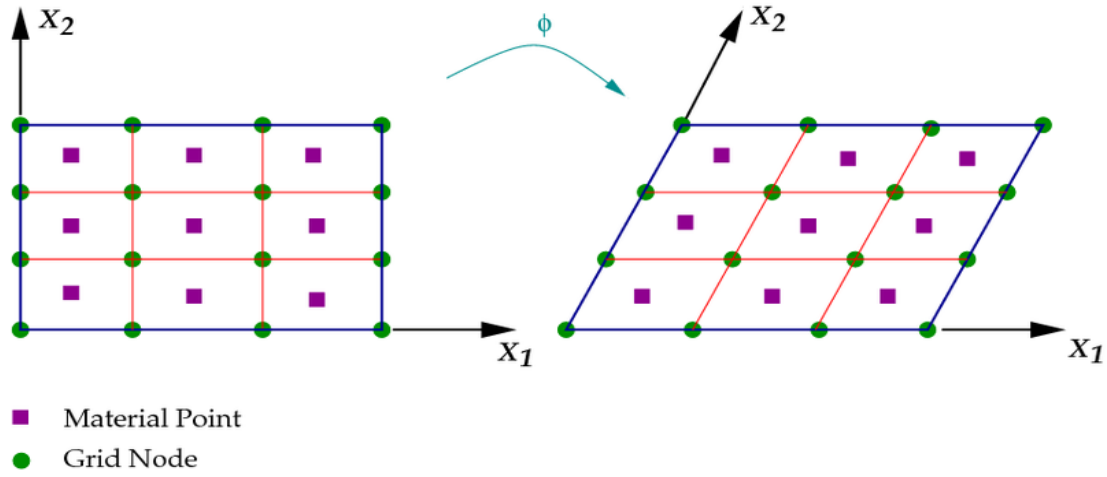

Figure 2.23 Lagrangian flow fields and mesh techniques (Ansys Polyflow User's Guide, 2012)

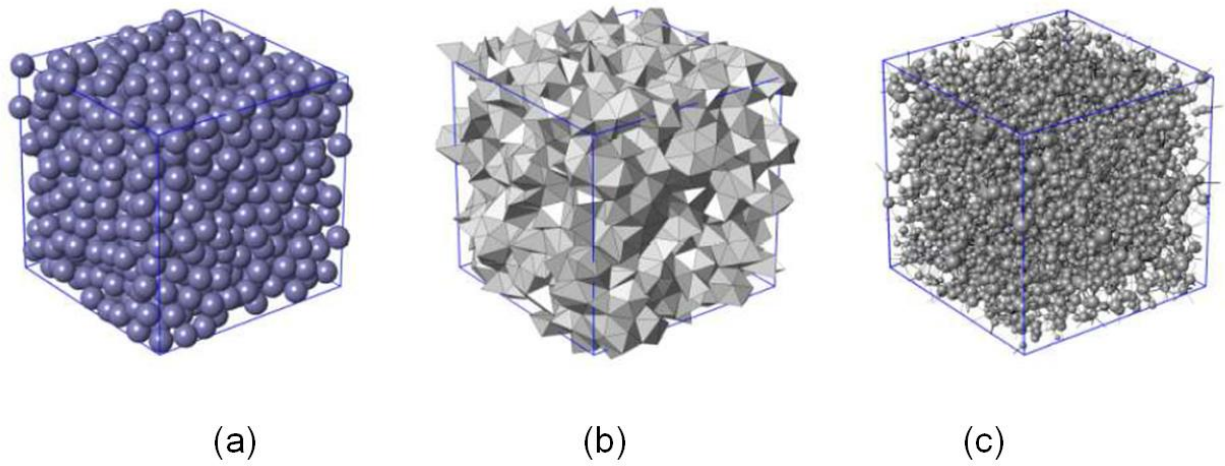

Figure 2.24 Transformation of a random packing into a physically representative network. (a) 1,000-sphere periodic random packing; (b) 3-D periodic Delaunay tessellation; (c) 3-D periodic network generated using the tetrahedron-merging algorithm (Balhoff and Thomson, 2004)

Chapter 3: Single-Phase Pore-Scale Network Modeling of Viscoelastic Flow through Porous Media

Quantitative and predictive behavior of viscoelastic flow in porous media is studied using a pore-scale network model in this chapter. Computational fluid dynamics (CFD) modeling is first performed for an Upper-Convected Maxwell (UCM) model with a shear-thinning component in converging/diverging geometries representative of pore throats. These simulations are used to develop closed-form expressions for pressure drop as a function of fluid rheology and throat geometry. The equations are used as inputs to pore-network models physically-representative of real porous media and network simulations are used to obtain macroscopic results of apparent viscosity versus apparent shear rate. Comparison between these results to experimental data of partially hydrolyzed polyacrylamide (HPAM) polymer in bead packs show good agreement.

3.1 Model Development

3.1.1 Modeling of Viscoelastic Flow in Converging/Diverging Ducts

It is often desired to have closed-form expressions for flow rate as a function of pressure drop of in capillary tubes, converging/diverging ducts, or complex porous media. For creeping, Newtonian flow the relationship is linear,

$$q = \frac{g}{\mu_{eff}} \Delta P \tag{3.1}$$

where g is the hydraulic conductivity of the duct. For straight capillary tubes, the conductivity is simply $\pi R^4/8L$ and equation 3.1 is the well-known Hagen-Poiseulle equation. For non-Newtonian fluids, analytical relationships are only available for simple models and geometries. An alternative for more complex geometries is to develop semi-empirical relationships by

numerically solving the momentum equations coupled with a constitutive rheological model and the continuity equation. An closed-form model can then be fit to the numerical results as was done by Lopez et al. (2003) and Balhoff and Thompson (2004; 2006).

Here, the goal is to study geometries representative of pore throats and since the variation of the aspect ratio in a constriction pore can affect the shear-thickening behavior of viscoelastic fluids, we study converging/diverging, sinusoidal channels. A schematic of a typical geometry is depicted in Figure 3.1, where the wall of the channel is a sinusoidal function. These geometries maintain numerical simplicity (2D axisymmetric) while preserving the important characteristics of a pore throat relevant to viscoelastic flow (converging/diverging). For consistency to other authors who studied similar geometries (Deiber and Schowalter, 1981, Balhoff and Wheeler, 2009), the sinusoidal wall function is given by

$$r = h - \varepsilon \cos\left(\frac{2\pi z}{l}\right) \tag{3.2}$$

Two dimensionless quantities are used to describe the aspect ratio of the geometry are defined as

$$\alpha = \varepsilon/h = (r_{\max} - r_{\min})/(r_{\max} + r_{\min}) \tag{3.3}$$

and

$$\Lambda = 2\pi h/l = \frac{\pi(r_{\min}+r_{\max})}{2l} \tag{3.4}$$

The definitions of the parameters in equations 3.2 through 3.4 are also shown in figure 3.1.

Mathematically we solve the momentum equations (2.1) coupled with continuity equation (2.2) to obtain a steady-state velocity field in the geometry described above.

Equation 2.1 requires an input for the constitutive rheological model for stress tensor, $\boldsymbol{T}$. Many constitutive equations have been proposed for viscoelastic fluids that exhibit strong extensional flow effects to relate shear stress and rate, such as the Maxwell, Phan-Thien-Tanner, Giesekus, and Oldroyd-B models. The Upper-Convected Maxwell (UCM) model is chosen as the viscoelastic model in this work due to its relative simplicity.

The constitutive equation assumes linear elasticity. Although most real fluids are non-linear, the model is widely-used to gain physical insight to viscoelastic behavior because of its relative simplicity. Yin et al. (2006) proposed common viscoelastic fluids such as HPAM could be described by equation 2.24, if a shear-thinning model is employed for the viscosity term, η.

The boundary conditions are described as no slip at the wall (equation 3.5) and axial symmetry (equation 3.6) along with constant pressure drop across the entire channel. The periodic boundary condition has been used for inlet and outlet. The periodic boundary condition been used since the objective of this study is to simulate the viscoelastic flow through porous media which is consecution of pore throats.

$$r = h - \varepsilon \cos\left(\frac{2\pi z}{l}\right), \ \boldsymbol{u} = 0 \tag{3.5}$$

$$r = 0, \ \ \boldsymbol{u} = 0 \tag{3.6}$$

The geometry has two extended part on both inlet and outlet (1000 μm length for each side) to let the viscoelastic fluid have time to have a full-developed profile at inlet and outlet. To calculate pressure drop for converging-diverging section, the total pressure drop from inlet to outlet calculated from CFD simulation, then the pressure drop for extended parts (capillary tube) subtracted from the total pressure drop, in this way the pressure drop for converging-diverging part calculated.

All CFD modeling was performed using Polyflow, a finite element package of ANSYS. The approximate minimum fill (AMF) direct solver was used due to its robustness compared to some other solvers such as multi-grid iterative solver. The DEVSS SU (discrete elastic-viscous split stress streamline-upwind) interpolation technique for stresses was chosen to improve convergence (Guenette and Fortin, 1995). A schematic of the mesh is shown in figure 3.2. Sensitivity analysis has been performed to determine mesh refinement such that further refinement does not affect the solution. The number of elements and mesh configurations are different for different geometries.

The problem is numerically difficult to solve in terms of stability and convergence (Huang et al. (1995); Hulsen et al. (2005)). The reason is that current mathematical formulations of viscoelastic flow lead to a highly non-linear problem and in most practical cases exhibits strong singularities, especially when the fluid exhibits high elasticity, i.e., at large λ or large shear rate. To overcome stability and convergence difficulty of viscoelastic fluid flow an evolution technique is used here. The solution in a previous step (smaller λ) is used as a first guess for the next calculation (higher λ). When the elastic effects are more pronounced and λ is too high, the problem becomes extremely difficult to converge and the simulation is abandoned.

3.1.2 Network Modeling

Network modeling is an efficient way to investigate flow in porous media at the microscopic level. Network models have been shown to be quantitative and predictive in certain instances (Bryant et al., 1993; Baake and Oren, 1997, Blunt, 2001; Lopez et al., 2003; Balhoff and Thompson, 2004, 2006), but in order to so the models must (1) be physically-representative of the morphology of the porous medium from which it is mapped and (2) first-principle flow equations that correctly describe the physics in each pore throat must be utilized as inputs.

Here, the porous media studied are packed beds of granular media. Computer generated media are formed using a collective rearrangement algorithm as described by Balhoff and Thompson (2004; 2006). The porosity and grain size can be defined *a priori*. Boundaries can be periodic or fixed, and here the boundaries are periodic to minimize edge effects. The porous medium is mapped to a network model via a Delaunay tessellation algorithm as described by Al-Raoush et al. (2003). The resulting network model is made up of pores connected by throats. The connectivity in the network varies and the volume of each pore and throat conductivity, g, is unique and dependent on the pore/throat geometry. The conductivities are computed as defined by Al-Raoush et al. (2003). Information about the pore and throat radii, aspect ratio, etc. are also extracted which allows for calculation of geometric parameters described in equations 3.2-3.4 for a sinusoidal-varying duct. Capturing the converging-diverging nature that occurs in porous media is essential for proper modeling of complex fluid flow; in particular, for viscoelastic fluids, the contraction/expansion channel give rise to extension in the direction of the flow and brings out fluid elasticity that is responsible for the viscosity thickening behavior. The porous media studied in this work were computer-generated random sphere packs.

The general approach to pore-network modeling is to impose mass conservation on the N pores and obtain pore pressures by solving the resultant system of $N \times N$ equations subject to specified boundary conditions (here a constant pressure drop is applied in one direction and periodic boundary conditions are imposed in the other two). For an incompressible fluid, mass conservation on pore i must be satisfied. For a simple case of Newtonian fluid, equation 3.1 applies and we get

$$\sum_j q_{ij} = \sum_j \frac{g_{ij}}{\mu}\left(P_i - P_j\right) = 0 \tag{3.7}$$

for each pore. q_{ij} in equation 3.7 is the volumetric rate of flow from an adjacent pore *j* into pore *i* through their interconnected throat, P_i is the pressure in pore *i*, and g_{ij} is the hydraulic conductivity for the pore throat that connects pore *i* and *j*. Equation 3.7 states that the net accumulation of fluid in pore *i* is zero.

For non-Newtonian fluids, a nonlinear system of equations must be solved and the appropriate flow equation in each pore is required (analogous to equation 3.1). For viscoelastic fluids in particular, the converging/diverging throat geometry affects flow.

3.2 Results and Discussion

3.2.1 CFD Modeling

CFD simulations were conducted of UCM fluids in sinusoidal ducts in more than fifteen different geometries by varying the dimensionless aspect ratios, α and Λ. The dimensions of these geometries are summarized in Appendix A. All simulations were performed at constant pressure drop across the ducts. To investigate the effect of fluid elasticity (varying *De*), steady-state solutions were obtained for a range of relaxation times λ from zero to 0.05 s. Streamline pressure and velocity fields are summarized in Appendix B (figures B1-B5) for selected cases.

Figure 3.3 plots the results from all simulations as dimensionless pressure drop versus *D*e. Dimensionless pressure is defined as the ratio of the measured pressure drop for the viscoelastic simulation to the value obtained for a Newtonian fluid with the same viscosity. The Deborah number here is defined as

$$De = \frac{Q\lambda}{\pi r_{\min}^3} \tag{3.8}$$

De is obtained a *posteriori* by calculating the flow rate *Q* from the results of CFD simulation. All simulations show the dimensionless pressure drop approaches unity at low *De*

(no elastic effects), an initial decrease in the dimensionless pressure drop with *De*, followed by the expected shear-thickening regime. The reduction in observed resistance (at moderate *De*) was surprising to the authors initially, since the viscous part of the UCM is constant-shear viscosity (i.e. the viscosity-thinning region cannot be explained due to the increase in shear rate of the fluid). However, this phenomena has been observed by many other authors (Aboubacar et al., 2002; Alves et al., 2003; Binding et al., 2006; Aguayo et al., 2010), although few explanations are provided in the literature.

3.2.1.1 Effect of Geometry

The results in figure 3.3 are largely controlled by the aspect ratio, α, of the channel geometry. As shown in figure 3.1, this dimensionless quantity is related to the ratio of the minimum and maximum radius. A value of $\alpha = 0$ corresponds to a straight channel that does not converge/diverge. In this case, the dimensionless pressure is 1.0 at all *De* because no stretching/relaxation occur in a straight tube.

For a constant Λ, we observe greater deviation from unity with increasing α, particularly at low *De*. The "shear-thinning" regime is more pronounced and the shear-thickening is delayed to larger *De*. This thickening scales with *De* approximately the same for all α. Close inspection of the flow streamlines at particular *De* for different geometries with fixed Λ shows the occurrence of more vortex with the increase of α, indicating higher flow elasticity (e.g. figure B4).

For constant α, the dimensionless pressure drop increase with increasing Λ. In addition, the onset of viscosity thickening shifts towards lower D_e. Since Λ is the ratio of average radius to pore length (equation 3.4), larger Λ means shorter relative residence time in the channel and elastic effects are pronounced.

3.2.1.2 Development of the Pore Flow Equation

Using the CFD simulations in 15 geometries, we developed a new, semi-empirical model for viscoelastic flow in converging/diverging ducts by fitting an equation to the simulation data shown in figure 3.3. The new equation is given by equation 3.9. Appendix C describes the fitting process shows fits for the models to the numerical simulations.

The results of the CFD models described in equations 3.8 are used to develop semi-empirical equations and then input to the network model. The closed-form viscoelastic flow equation for converging-diverging duct is given by

$$\Delta P_D = 1 + BDe^A + C\ln\left(1 + De\right) \tag{3.9}$$

In equation 3.9, the exponent $A = 3$ was found suitable in all simulations. The coefficients B and C are geometry-dependent and given by

$$C = 0.42\alpha \tag{3.10}$$

$$B = 0.000178\Lambda^{2.38}\alpha^{-0.655} \tag{3.11}$$

The multidimensional Newton-Raphson method is then used to solve the system of nonlinear equations.

A few important notes should be made about equations 3.8-3.10. First, in the limit that De approaches zero, the fluid becomes inelastic and equation reduced to $\Delta P_D = 1$, as expected. Also, the equation reduces to unity in the limit that α or Λ approach zero, where the converging/diverging geometry is simply a capillary tube. In a straight tube, no stretching or relaxation of the fluid occurs and no elastic effects are observed. Second, the first two terms of equation 3.9 is identical to the theoretical equation 2.43, proposed by Wissler (1971) and others. Here, we find the exponent, A, is 3. Wissler (1971) derived a value of 2, but experimental data (Calk and Machac, 1995; Tiu et. al., 1997; Bendova, 2009) has suggested values ranging from 1-

5. The third term in equation 3.9 accounts for the apparent reduction in pressure drop at moderate *De*, before thickening occurs (figure 3.3). At larger *De*, the equation is dominated by the second term and shear-thickening is observed. The equation suggests that the dimensionless pressure drop increases monotonically as *De* approaches infinity. In practice, as the *De* increases, the shear rate increases and shear degradation of the polymer would eoccur. The polymer molecules would break and the viscosity and elasticity would decrease, thus resulting in a decrease (or plateau) of the dimensionless pressure drop. This behavior is not accounted for in the CFD simulations or model equations (3.8-3.10).

3.2.1.3 Incorporation of a Shear-Thinning Model

Equations 3.8-3.10 are dimensionless and were developed by using a shear-independent viscosity (Newtonian) in the viscous portion of the Maxwell model (equation 2.24). In order to make the equation dimensional, the pressure drop is given as the dimensionless pressure drop, ΔP_D times the pressure drop for the equivalent inelastic fluid. For Newtonian flow, pressure drop is linear with flow rate, and we get:

$$\Delta P = \left(\frac{\mu}{g} q \right) \Delta P_D \tag{3.12}$$

For non-Newtonian, shear thinning fluids, the relationship between pressure drop and flow rate is nonlinear. If an analytical equation is amenable, e.g. power-law or Ellis fluids (Carreau et al., 1979), it can be substituted directly in to equation 3.12. More generally, a shear-dependent (or flow rate dependent) effective viscosity (μ_{eff}) replaces the Newtonian viscosity. For example, the Carreau model is popular because it accounts for Newtonian plateaus at low and high shear rates as well as the shear-thinning regimes. In equation 3.13, $\dot{\gamma}$ is the shear rate, *K* is the flow consistency index, *n* is the power index, μ_0 and μ_∞ are the viscosities at infinitely high shear and zero shear, respectively.

$$\mu_{eff} = \mu_{\infty} + \frac{\mu_0 - \mu_{\infty}}{\left[1+\left(K\dot{\gamma}_{eff}\right)^2\right]^{\frac{1-n}{2}}} \tag{3.13}$$

The effective viscosity is therefore a function of effective shear rate, which cannot be directly calculated for a non-Newtonian fluid in a tube. However, Lopez et al. (2004) suggested that the effective shear rate could be approximated as:

$$\dot{\gamma}_{eff} = \frac{Q}{KQ_c} \tag{3.14}$$

Where,

$$Q_{\mathrm{c}} = \frac{\pi\gamma_{\mathrm{c}}R_{\mathrm{eff}}^3}{3} \tag{3.15}$$

$$\gamma_{\mathrm{c}} = \left(\frac{\mu_0}{K}\right)^{\frac{1}{n-1}} \tag{3.16}$$

Lopez et al. (2004) further suggested that the effective radius, R_{eff}, could be back-computed using the Hagen-Poisseulle equation.

$$R_{\mathrm{eff}} = \left(\frac{8Lg}{\pi}\right)^{0.25} \tag{3.17}$$

Balhoff and Thompson (2006) performed numerical simulations of shear-thinning fluids in converging/diverging geometries and developed more complicated relationships for the effective radius. Their equations are implemented in here.

Equations 3.12-3.17 can then be combined to obtain a closed-form equation for a viscoelastic (Maxwell) fluid with a shear rate-dependent viscosity. Good agreement was obtained for the dimensionless pressure drop versus *De* against numerical simulations when the Carreau model was included with Maxwell equation. A more useful equation, at least for network modeling purposes, relates flow rate to pressure drop as shown in equation 3.18.

$$Q = \frac{g}{\mu_{\mathrm{eff}}} \frac{\Delta P}{\left[1 + BDe^3 + C\ln(1+De)\right]} \tag{3.18}$$

The expression is nonlinear and transcendental since both μ_{eff} and *De* are flow rate (*Q*) dependent. For a given pressure drop, the flow rate can be computed using Newton's method.

3.2.2 Pore Network Modeling

Pore-network modeling simulations were conducted and the results were compared against experiments by Yuan, which included Pusher, a viscoelastic HPAM solution in bead packs. The grain sizes (100 μm and 250 μm in diameter) and porosities of the Yuan's experiments are summarized in Table 3.1. They were used to develop physically-representative network models as outlined in the *Model Development* section.

Table 3.1 also summarizes the fluid and rheological parameters found by Yuan (1981). He fit steady shear data of viscosity versus shear rate to a Carreau shear-thinning model to obtain viscous rheological parameters. The relaxation time was found from the G', G" cross over point on an oscillatory shear test. Rheological parameters were substituted into equations 3.13-3.18 which were then substituted into the mass balance equations (equation 3.7) for the appropriate network model. A multidimensional Newton-Raphson algorithm was used to solve the nonlinear system of equations.

Figures 3.4 and 3.5 show the comparison between the network model and Yuan's experimental data. All are presented as μ_{app} versus $\dot{\gamma}_{\text{app}}$, where μ_{app} and $\dot{\gamma}_{\text{app}}$ are apparent viscosity and apparent rate in porous media, respectively, defined as follows:

$$\mu_{app} = \frac{k}{u}\frac{\Delta P}{L} \tag{3.19}$$

$$\dot{\gamma}_{app} = C'\left(\frac{3n+1}{4n}\right)\frac{u}{\sqrt{k\phi}} \tag{3.20}$$

Where the constant, C', is dependent on the medium by taken to be 6.0 here (Cannela, 1988). Figure 3.4 shows three data sets (a, b, and c) of HPAM Pusher polymer solution in packed beds of 100 μm beads. Figure 3.5 depicts three additional data sets (d, e, and f) in packed beds of 250 μm beads. Additional details about the fluids and porous medium properties are given in Table 3.1.

Figure 3.4 shows the histogram of aspect ratio for case d which has a grain size of 250 micron. As it shows the value of aspect ratio for this case is between 0.02 and o.54 which is in range of aspect ratio analyzed in single-phase CFD simulation. In figure 3.5 the histogram of the dimensionless length group (Λ) had been shown for case d which roughly in the range of 1 to 10. However, since the range of Λ is beyond the Λ-value analyzed in CFD simulation, the good agreement between pore-network results and experiments in figure 3.9 shows the closed-form equation (equation 3.9) still is valid for higher Λ-value. Figure 3.6 shows the histogram of pore-level Deborah number for macroscopic Deborah number of 10 for case 10. As it shows in figure 3.6 the pore-level De is in low range of pore-scale Deborah number compared to the figure 3.7 which the histogram of the pore-level De number for case d at the macroscopic De of 100. Figures 3.6 and 3.7 show as the macroscopic De number increase, there are more pore throat in pore-network simulation with high pore-level De, and more pore-throat will be in shear-thickening regime.

Figures 3.8 and 3.9 show good agreement between experimental measurements and predictions from the network model. No *ad hoc* adjustments were made to the model. The network model follows the trend of the data, which includes a Newtonian plateau at low shear rates (<10 1/s), shear-thinning behavior at intermediate shear rates (10-100+ 1/s) and extensional shear thickening at high shear rates (>1000 1/s). It should be noted that the pore-level equations

were developed using CFD simulations for De <12, but many pores in the model exceed this limit and we assume the equations are valid at all De. The network model seems to be sufficient even at high shear rates (and therefore, De).

There are some discrepancies between the network model and data. For example, in data sets c (figure 3.8), and d and e (figure 3.9), the network model under predicts the apparent viscosity, especially at the low shear rate region. This could be attributed to adsorption of polymers on the wall and plugging; Hirasaki and Pope (1974) showed that polymer adsorption can reduce the channel size and henceforth the permeability of the porous media, resulting in a higher flow resistance. However, since the difference between predictive apparent viscosity and that from Yuan's measurement is relatively small, adsorption or other permeability reduction effects may not be significant for these bead packs.

In data sets b (figure 3.8) and d (figure 3.9), the predictive curves overestimate the apparent viscosity at high apparent shear rate (above 10^3 s^{-1}). The pore-level equations (3.18) suggest that the flow resistance (or apparent relative viscosity) would tend to infinity with the flow rate (or apparent shear rate). However, some experiments showed that the apparent viscosity reached a plateau at high shear rates; this behavior that shear-thickening viscosity caused by elastic effect does not increase without bound (Kullcke and Haas, 1984). One plausible explanation for the plateau is that the polymer degrades at these high shear rates, thus reducing its viscosity and elasticity. Cases b and d correspond to Pusher solutions and it was reported by Yuan (1981) that the onset of shear rate for Pusher-700 degradation is at about 10000 sec^{-1}. For polymers that have slight shear degradation, such as Water Cut 110 (e) and Water Cut 160 (f), the prediction from modeling agrees much better against experiments at high shear rates.

3.2.3 Numerical Accuracy of DEVSS-SU

CFD simulation for viscoelastic problems at which the fluid elasticity is significant is challenging because in addition to velocity and pressure variables, the numerical methods are required to handle another variable called extra-stress tensor. The extra-stress tensor includes elastic and purely-viscous components. The combination all these variables make CFD simulation for viscoelastic flow highly non-linear. This combination of variables is called mixed-mixed elements, since continuity equation is the constraint for velocity, and velocity is the constraint for extra-stress tensor.

To solve this mixed-mixed element problems, several interpolation techniques have been proposed, which are usually geared to certain viscoelastic models and geometries. Several techniques tend to disappear from use in the literature because they are not stable, accurate, and/or robust for the selected problem. There is not one method which is valid and definitely robust for all cases. However, the selection of different methods depends on the type of flow at the investigated conditions. The parameters which are important to select the methods include geometry, boundary conditions, viscoelastic model, even matter at which Deborah number the methods is used. EVSS and DEVSS interpolation techniques are a robust technique which is widely used. In EVSS and DEVSS interpolation techniques, the extra-stress tensor is split into two parts: purely viscous and elastic components. The split form is replaced into the constitutive equation and will be solved. Then combing both elastic and purely-viscous component recovers the solution for total extra-stress tensor (Van Schaftingen and Crochet, 1984; Marchal and Crochet, 1987; Rajagopalan, 1990; Crochet, Delvaux, and Marchal, 1990; Crochet and Legat, 1992).

In the DEVSS method, the purely-viscous term is in terms of velocity unknowns rather than rate-of-deformation unknowns in momentum equation. This replacement does not change

the constitutive equation for viscoelastic problem, but reduces the level of non-linearity of the problem. The DEVSS method used bi-linear interpolation for rate-of-deformation and stress which make this method one of cheapest in terms of computational cost (Guenette and Fortin, 1995). In addition to the interpolation technique, depends on the problem different finite element discretization techniques can be selected for momentum equation, continuity equation and viscoelastic constitutive equations to make the numerical method more robust. These discretization methods include Galerkin, Streamline Up-winding (SU), Streamline Up-winding Petrov-Galerkin (SUPG), Discontinuous Galerkin methods among many others (Brooks, 1982; Marchal and Crochet, 1987; Luo, 1989; Rajagopalan, 1990, Kumar, 2014). For selected problem in this study at which elasticity plays an important role, and in presence of flow singularity, the SU method is found to be more robust due to the nature of SU method (Kumar, 2014). Notably, Discontinuous Galerkin may be more stable; however it requires additional variables at the interface between elements or some tricky algorithm for solving the discontinuity (Kumar, 2014).

In this study, a DEVSS-SU interpolation scheme has been used. In correspondence with the developer of FEM software package employed in this work (Ansys Polyflow), DEVSS-SU is a good choice for selected problems in this study, because of good balance between computational cost and accuracy. That is the reason it was originally implemented into Polyflow. DEVSS/SU has been largely used for 2D and 3D flows, on fixed domains as well as on moving geometries (Guenette and Fortin, 1995). There are other methods which may be better for a specific class of flows, but for which we do not know whether they will be as robust for other cases. There are also techniques which involve too many constraints, and which are thus impractical (Guenette and Fortin, 1995; Keuning, 2001; Kumar, 2014). Despite the discussion in

this section about the accuracy and robustness of DEVSS/SU for this problem, there is some evidence to the contrary, and the investigation on this problem is an area of future work of this study.

3.3 Conclusions

A predictive pore network model of single-phase viscoelastic flow was developed and compared to experimental data of polymer solutions in bead packs. The pore-level flow equations input to the model were found by fitting curves to CFD simulations of viscoelastic flow in converging/diverging, sinusoidal geometries. A few of the key conclusions of this work are as follows:

- CFD simulations of a viscoelastic upper-convected Maxwell (UCM) model showed an initial decrease in dimensional pressure drop with De, followed by a sharp increase that appears unbounded. The strong nonlinearities of the problem prevented simulations for De>12. The CFD simulations agreed qualitatively with simulations by other authors
- The geometry of the throat affected the relationship between pressure drop and flow rate in the CFD simulations. For larger dimensionless parameters (α and Λ) the geometry deviated more from a capillary tube and as a result the flow deviated more from linearity (Hagen-Poisseule flow).
- A new closed-form expression for dimensionless pressure drop versus De for viscoelastic flow in converging/diverging ducts was developed and matched well to CFD simulations in several geometries.

$$\Delta P_D = 1 + BDe^A + C\ln\left(1+De\right) \tag{3.8}$$

In the equation, B and C are dependent on the duct geometry (α and Λ) and $A = 3$. The first two terms agree with the theoretical derivation of Wissler (1971), although he found $A = 2$. The last term accounts for the decrease in resistance at moderate *De* observed here and by many other authors.

- Network model simulations mostly agreed well with experimental data of HPAM solutions in bead packs. No *ad hoc* adjustments were made. Some discrepancies between the model and experiments were noted which could be attributed to any number of factors including polymer adsorption and polymer degradation.

Table 3.1 Porous medium and fluid parameters (Yuan ,1981)

	a	b	c	d	e	f
Grain size (μm)	100	100	100	250	250	250
Porosity (%)	39	39	39	39	39	39
Permeability (D)	4.5	4.5	4.5	37.2	37.2	37.2
Polymer	Pusher-700	Pusher-700	Pusher-700	Pusher-700	W.C. 110	W.C. 160
concentration(ppm)	1000	500	1000	1000	500	500
Molecular Weight (g/mol)	5e6	N/A	5e6	5e6	N/A	N/A
% NaCl	1	1	0.1	1	0.02	0.02
%NaHCO3	N/A	N/A	N/A	N/A	0.005	0.005
μ_∞(cp):	1	1	1	1	1	1
μ_o(cp):	8	3	36	8.4	7.5	1.14
n:	0.75	0.77	0.591	0.73	0.63	0.057
K:	0.057	0.057	0.158	0.057	0.038	0.001
relaxation time (s)	0.035	0.031	0.066	0.035	0.002	0.0014

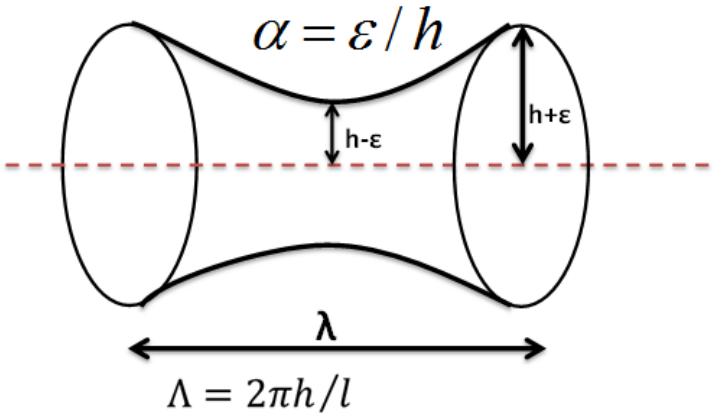

Figure 3.1 Schematic shape of sinusoidal duct used in CFD modeling

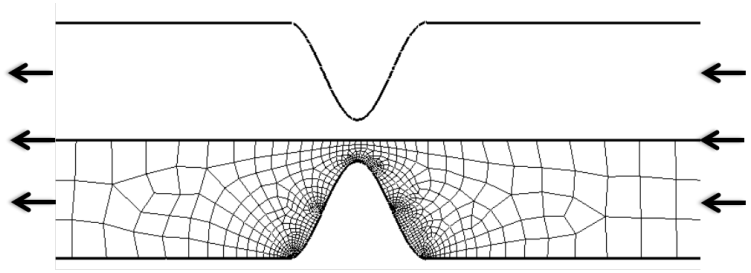

Figure 3.2 A schematic of the mesh applied to a converging/diverging sinusoidal channel

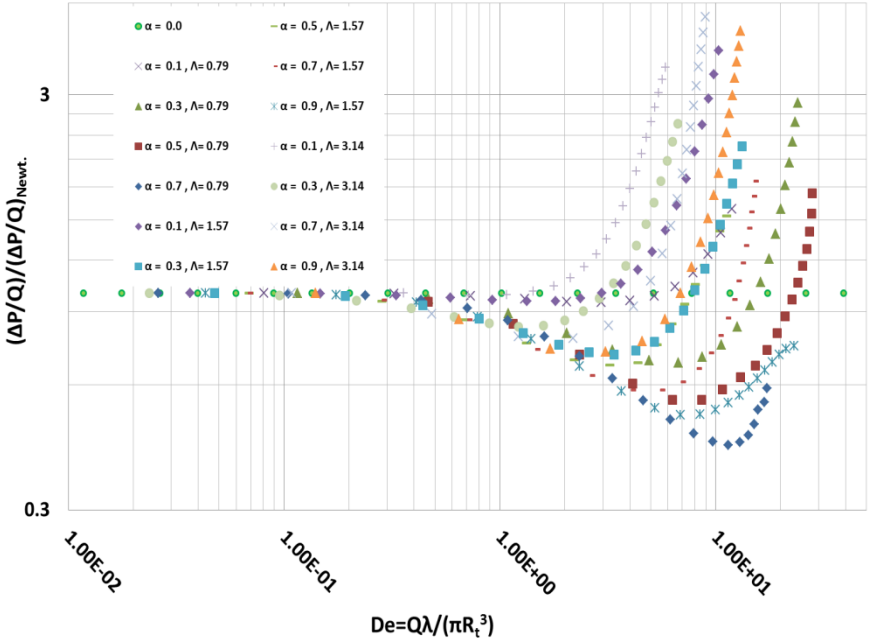

Figure 3.3 Apparent relative viscosity versus Deborah number for 15 sinusoidal channels investigated in this work

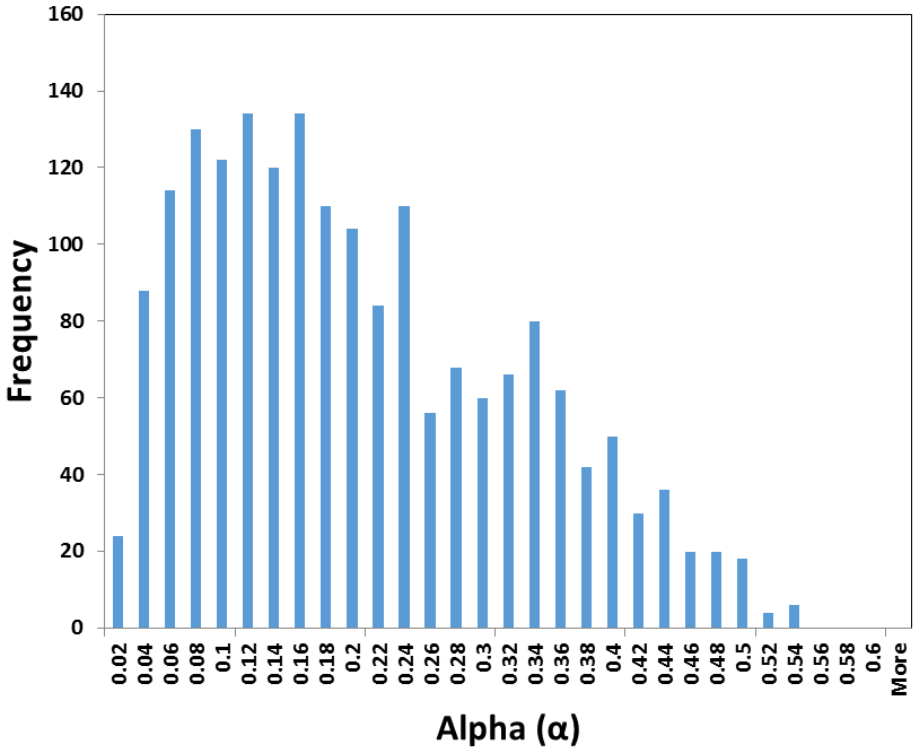

Figure 3.4 The histogram of geometry parameter (α) for grain size of 250 micron (case d)

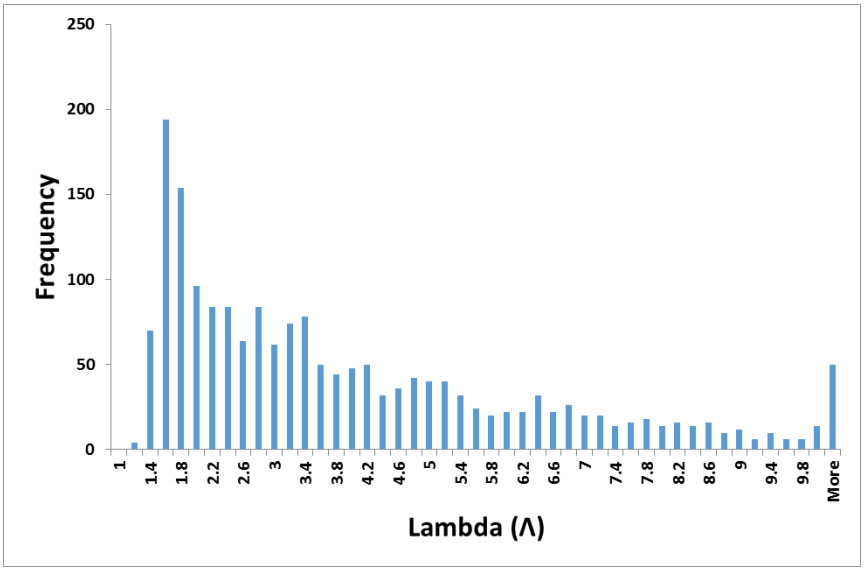

Figure 3.5 The histogram of geometry parameter (Λ) for grain size of 250 micron (case d)

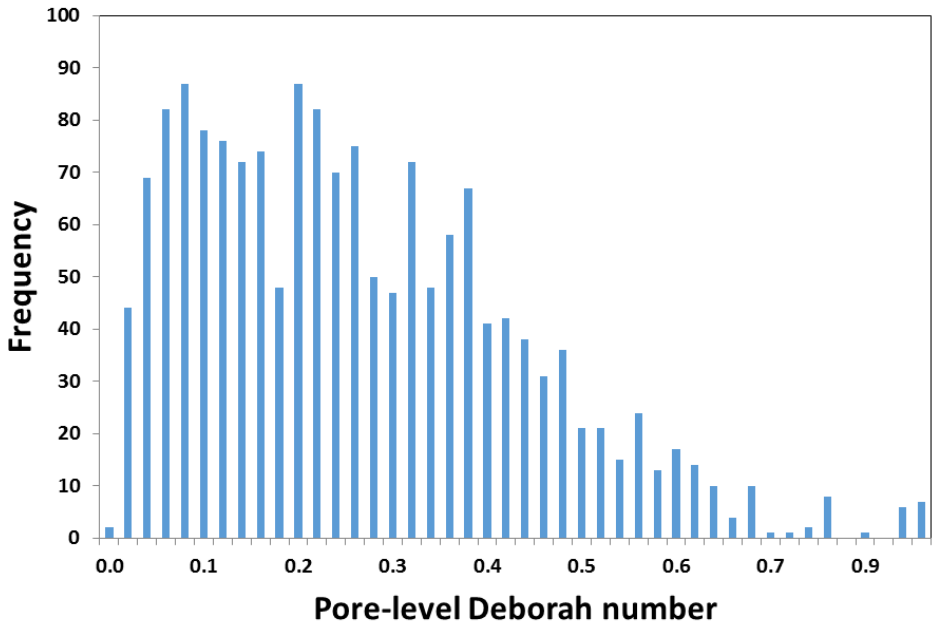

Figure 3.6 The histogram of pore-level Deborah number for macroscopic Debrah number of 10 (case d)

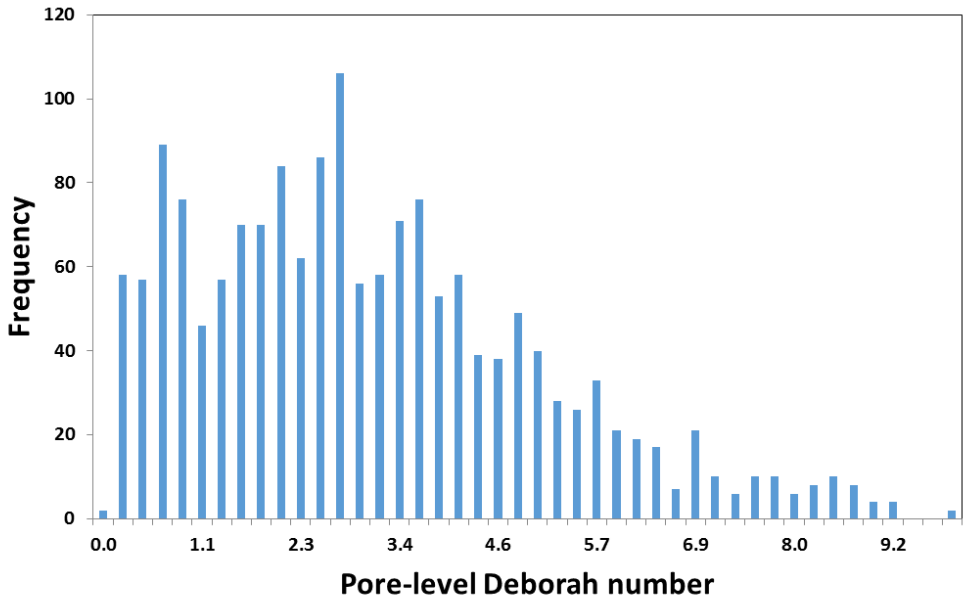

Figure 3.7 The histogram of pore-level Deborah number for macroscopic Debrah number of 100 (case d)

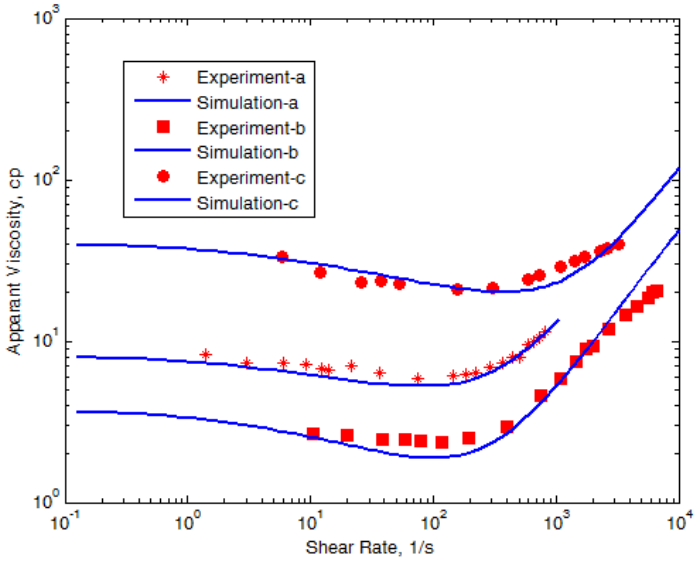

Figure 3.8 Apparent viscosity versus apparent shear rate for pore-network simulation (solid lines) and Yuan's (1981) experiments (bullets) of 100 mm bead-pack porous media. The three data sets correspond to polymer solutions of (a, star)1000 ppm Pusher-700 in 1% NaCl brine; (b, square) 500 ppm Pusher-700 polymer in 1% NaCl brine and (c, circle) 1000 ppm Pusher-700 polymer in 0.1% NaCl brine

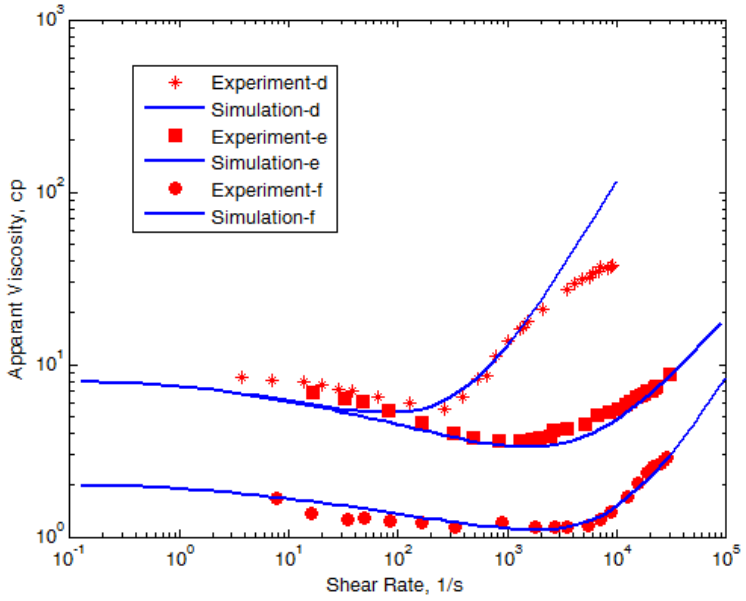

Figure 3.9 Apparent viscosity versus apparent shear rate for pore-network simulation (solid lines) and Yuan's (1981) experiments (bullets) of 100 mm bead-pack porous media. The three data sets correspond to polymer solutions of (d) 1000 ppm Pusher-700 polymer in 1% NaCl brine, (e) 500 ppm, Water Cut 110 in brine composed of 0.02% NaCl, 0.005% $NaHCO_3$ and 0.005% $CaCl_2$, and (f) 500 ppm, Water Cut 160 in brine composed of 0.02% NaCl, 0.005% $NaHCO_3$ and 0.005% $CaCl_2$

Chapter 4: Static CFD Modeling of Viscoelastic Fluid around an Oil Droplet[1]

The possible reasons to reduce the residual oil saturation during injection of viscoelastic polymer are discussed in Chapter 2; background and literature review. One of the hypotheses is that the forces acting on oil phase from displacing fluid is more significant for viscoelastic fluid compared to purely-viscous fluid.

In this chapter, CFD modeling is performed for fluid around a static (stationary) oil droplet. The oil droplet is stationary and it does not move and/or deform during the simulation and CFD simulations are performed for a fluid around the droplet. The forces acting on the oil droplet are evaluated for Newtonian fluid and viscoelastic fluid at different Deborah number. The results show that the forces calculated due normal stresses are significant for viscoelastic fluid compared to Newtonian, and then the total forces eventually may overcome the capillary pressure and displace the oil phase and pass it through the pore throat. In addition as the oil phase is positioned closer to the constriction part of geometry the magnitude of the force are even higher.

4.1 Mathematical and Numerical Approach

In order to better understand the observed decrease in residual oil in experiments and field data, CFD modeling is performed here for viscoelastic flow around stationary oil droplets. The hypothesis of this work is that large normal forces in viscoelastic fluid flow leads to formation of stable oil threads which draw the trapped oil out of the tight pore structure. Extra

[1] This chapter is published at the Journal of Petroleum Science and Engineering, Vol. 94-94, pp. 79-88, September 2012, Afsharpoor, A., Balhoff, M.T., Bonnecaze, R., Huh, C., "CFD Modeling of the Effect of Polymer Elasticity on Residual Oil Saturation at the Pore-Scale". Balhoff, M.T., Bonnecaze, R., Huh, C. have contributions on the main idea and the geometry has been studied.

normal forces due to normal stress may become significant for viscoelastic flow and push the trapped oil droplet. Only increasing the viscosity by adding polymer is insufficient to mobilize the trapped oil; therefore, other phenomena at the pore level must contribute to the observed mobilization of the oil. In porous media, the wetting phase (e.g., polymer-containing water) flows along the walls and non-wetting phase (e.g., oil phase) flows at the center of the pore. CFD modeling is used here to simulate two-phase flow in geometries approximating pore throats (sinusoidal ducts) to understand the fundamental physics of viscoelastic fluid dynamics at the pore level. This geometry keeps the model simple, but provides the required characteristics of a pore throat to investigate viscoelastic flow. In order to observe elastic effects, geometry with varying cross-section, perpendicular to the flow direction, is needed.

We define *De* here for converging/diverging ducts as follows:

$$De = \frac{Q\lambda}{\pi R_t^3} \quad , \tag{4.1}$$

where Q is volumetric flow rate, λ is the polymer molecule's relaxation time, and R_t is the narrowest radius of the pore throat. Elastic effects are negligible for $De \ll 1$; at large *De*, first normal stress differences play an important role, which leads to extensional viscosity effects that dominate over shear viscosity (Macosko, 1994). Extensional flows are those that occur as a result of normal stresses as opposed to shear stresses (which result in shear flows). The extensional viscosity is defined as the first normal stress difference divided by the rate of strain. The ratio (Trouton) of extensional viscosity to shear viscosity is 3 for simple fluids but can be much higher for fluids exhibiting nonlinear viscoelasticity. In this study the upper convected Maxwell (UCM) model (equation 2.24) is used to as the constitutive equation for the viscoelastic fluid.

It has been suggested that an UCM reasonably describes the rheology of HPAM. The goal of this work is not necessarily predictive in nature, but rather to obtain a fundamental

understanding of the micro forces on an oil droplet. This could be accomplished with any viscoelastic fluid; the UCM is chosen because of its relative simplicity.

The UCM rheological model (2.24) can be directly substituted into the momentum equations (2.1) and coupled with the continuity equation 2.2. With the exception of very simplified geometries and low *De*, these equations cannot be solved analytically. For more complex geometries (such as the sinusoidal pore throat used here), numerical methods such as the finite element method (FEM) must be implemented.

Figure 4.1 shows schematic figures of throat geometries used in this work. The geometry is 2D axisymmetric and the problems solved were steady state with both fixed inlet/outlet flow rates (both fixed pressure and flow rate boundary conditions have been tested). The fluid flows from top to bottom in figure 4.1 and different forces acting on the stationary oil droplet are evaluated in the results section. The geometry is sinusoidal, but with the in-flow and out-flow zone lengths extended to ensure fully-developed flow. Since the geometry is axisymmetric, only half of the domain is modeled and a symmetry boundary condition is employed at $r = 0$.

Solution of the momentum equations for viscoelastic flow is difficult because it is a highly nonlinear problem; in most practical cases ($De > 1$; converging/diverging geometry) the problem exhibits strong singularities. Therefore the problem is numerically difficult to solve in terms of both stability and convergence (Huang et al. (1995), Hulsen et al. (2005)). In this work, ANSYS Polyflow software has been used to solve this complicated numerical problem, DEVSS-SU interpolation technique has been used to overcome this difficulty.

Sensitivity analysis has been performed to determine mesh refinement such that further refinement does not affect the solution. The number of elements and mesh configurations are different for different cases as discussed in the results and discussion section. Among various

boundary conditions, fixed pressure and fixed volumetric flow rate have been tested for inlet and outlet. No-slip conditions for the pore wall and stationary oil droplet are applied.

4.2 Results and Discussion

Numerical simulations were performed with the geometries shown in figure 4.1. The fluid was described by the Upper-Convected Maxwell model (UCM) with rheological properties, λ = 0 to 0.25 s and μ = 40 cp (0.04 Pa-s). The *De* number can be controlled by either changing the relaxation time (done here) or inlet/outlet boundary condition values (pressure drop or flow rate) across the throat. Two locations of the oil droplet are studied: (1) in the center of a pore and (2) upstream of a constriction. The first geometry (depicted in figure 4.1a) is referred to as "pore-centered geometry" and is interesting because of the symmetry in the *z*- and *r*- directions. The second geometry (depicted in figure 4.1b) is referred to as "constriction geometry" and may be more realistic as it represents a droplet that requires force to be squeezed through a constriction.

In all simulations the oil droplet was stationary and of fixed size. This idealized case might correspond to a situation where capillary forces are so strong that the forces acting on the droplet (pressure or normal stress) are not significant and therefore are unable to mobilize the droplet or change the shape (even for the viscoelastic fluid). The geometry is hypothetical, but nonetheless provides the insight needed to understand the fundamental physics driving reduced residual oil saturation in the presence of fluids that are elastic.

4.2.1 Pore-Centered geometry

Figure 4.1(a) depicts the dimensions of the pore geometry. The first set of simulations involved fixed flow rate boundary conditions of $Q = 1\times10^{-14}$ m^3/s (approximate Darcy velocity of 1 ft/day). The mesh arrangement has 1798 nodes and 1647 elements for the simulations of this

geometry with a fixed flow rate boundary condition. The mesh configuration is shown in figure 4.1(a).

Figure 4.2 shows the pressure fields for both a Newtonian fluid (*De* = 0) and viscoelastic fluids (*De* = 0.4, 0.7, and 1.4 respectively). The results show that the pressure field for viscoelastic fluids is non-symmetric. This asymmetry increases with *De* and is due the elastic behavior of the fluid. Unlike a Newtonian fluid which instantaneously relaxes when a stress is imposed, viscoelastic fluids have memory; they require time to return their original shape. Past the droplet, a distorted pressure field for high *De* occurs. Further downstream, the pressure field is more symmetric because the fluid has sufficient residence time to relax.

For similar reasons, a low-pressure pocket exists ahead of oil droplet which results in the local pressure gradient across the oil droplet to be more than the average pressure gradient in the pore body along the symmetrical axis. The pocket ahead of oil droplet is due to secondary flow /eddies formed under elastic conditions. The fluid is unable to instantaneously relax as it passes the oil droplet. The flow streamlines are therefore more tangential to the pressure gradient and the lack of flow ahead of the droplet results in a low pressure. We note that the low-pressure pocket does not necessarily imply that the pressure force is higher for viscoelastic flow than Newtonian flow because the pressure force is the line integral of pressure over droplet surface. For this particular geometry and boundary condition, the pressure force is higher for higher *De* (Table 4.1), but in subsequent simulations the opposite behavior is observed.

Figures 4.3 and 4.4 show the velocity field and normal stress field, respectively, for the same *De* numbers as depicted in figure 4.2. The velocity field for viscoelastic fluids is non-symmetric and the velocity is higher near the center. The velocity field is distorted downstream of the oil droplet at higher *De*; this asymmetry is expected behavior and is a direct result of the

normal forces The normal stress is negligible for the Newtonian fluid compared to viscoelastic fluid, especially around the oil droplet; this effect is more pronounced as the *De* number increases. Normal stress forces for Newtonian fluids are typically neglected when determining local forces and equilibrium conditions on a droplet (Lake, 1989). However, for the viscoelastic fluid, normal forces are significant even at the relatively low *De* studied here. These normal forces are likely much more significant at the higher *De* observed in EOR processes. Unfortunately, the strong nonlinearities of the problem prevent modeling at *De* larger than performed here. Attempts to model viscoelastic fluids at higher *De* (or Weisenberg number) continues to be a challenge in all disciplines, and development of numerical algorithms to solve this nonlinear problem continue to be developed (Hulsen et al., 2004).

Table 4.1 compares the forces due to pressure and normal stress for the Newtonian and viscoelastic fluids. The table shows that both pressure and normal stresses increase with *De* for this geometry and therefore the total force imposed on the droplet increases with *De*. At the relatively low *De* investigated here (*De* <1.5), normal stress forces are still an order-of-magnitude smaller than pressure forces. However, the normal forces are increasing at a much faster rate than pressure forces. In the applications of EOR, a common range of shear rates (1-10 *1/s*) in pore throat and range of relaxation times (0.01-15 *s*) for polymers used in the field, the *De* number can be significant for a typical pore throat size of 1 μm (Heemskerk et al., 1984; Cannella et al., 1988; Masuda et al., 1992; Garrocuh and Gharbi, 2006; Delshad et al., 2008; Kim et al., 2009; Lee et al., 2010). It is likely that at this higher *De*, normal forces would dominate over pressure forces and could result in mobilization of residual oil. In the extreme case of near–wellbore flow, *De* = *O*(100) may be observed due to the very high velocities. Although the near-

wellbore region represents only a small portion of recoverable oil, extremely high *De* is observed.

4.2.2 Constriction Geometry

Simulation geometry is employed in which the oil droplet is bigger than the pore throat (figure 4.1b). Simulations in this geometry are numerically more challenging than the former (pore-centered geometry) because the fluid contraction at the narrowest radius representing the pore throat leads to high elasticity in that region and makes it numerically difficult to solve. The required mesh is extremely fine. Quadrilateral element shapes with 1960 nodes and 1790 elements was found to be an efficient mesh arrangement for this specific geometry.

Figure 4.5 shows the pressure field for a Newtonian fluid and viscoelastic fluids at different *De* numbers for a fixed flow rate boundary condition ($Q = 1\times10^{-15}$ m^3/s). As the *De* number increases, the overall pressure drop across the entire pore increases, and a low-pressure pocket starts to form in front of the oil droplet. Unlike the pore-centered geometry, the low-pressure pocket does not lead to more pressure force across the droplet for viscoelastic fluids at higher *De*. The summary of force balances are tabulated in Table 4.2.

It should be noted that the viscosity is the same (40 cp) for all simulations, regardless of whether the fluid is Newtonian or viscoelastic in order to isolate the effects of normal forces on the oil droplet. In practice, viscoelastic polymers are also much more viscous (by 1-2 orders of magnitude). Mobilization of oil by viscoelastic polymers may be a result of a combination effects, including additional pressure drop due to an increase in viscosity as well as normal forces that are not significant for purely viscous fluids.

Figure 4.6 shows the normal stress field (T_{rr}) for the same *De* utilized in figure 4.5. As expected the normal stresses are more pronounced as the *De* number increases; accordingly, the

normal forces are increasing as summarized in Table 4.2. Figure 4.7 compares the velocity profile for Newtonian and viscoelastic flow at different *De*; it shows that as the fluid becomes more elastic the velocities in the pore throat will be smallest at the center. Fundamentally, due to no-slip boundary condition, for Newtonian fluids, the velocity is higher at the center rather than near the wall; toward the center the velocity increases for Newtonian fluid. The no-slip condition is still imposed at the wall for viscoelastic flow, but the velocity is increasing near the throat center, further demonstrating the non-symmetric behavior of viscoelastic fluids.

The final simulations were conducted in the constriction geometry for a fixed pressure boundary condition (instead of fixed flow rate). Polymer injection can occur at constant rate or constant pressure conditions. At the pore-level the appropriate boundary conditions may be better represented by a constant rate or constant pressure gradient (regardless of the well constraint). Therefore, for completeness we also investigate constant pressure gradient across pore throats. The pressure drop across the throat utilized here is 10 Pa (corresponds to ~ 8 psi/ft) in all constant pressure simulations. Increasing the elasticity of the fluid (by increasing the relaxation time) results in an increase in resistance to flow. The mesh arrangement and numerical strategies are the same as the constant-flow simulations in figures 4.5-4.7. Figure 8 shows the pressure fields, which appear similar for all *De* across the geometry, but the pressures across the oil-droplet are different as listed in Table 4.3.

Figure 4.9 shows the normal stress (τ_{rr}) for the different *De* numbers, and as expected the higher the *De* number, the higher the normal stress, even though the flow rate is lower for higher *De* number case. Figure 4.10 compares the velocity profile for Newtonian and viscoelastic flow at different *De* number, which shows as the elasticity increases, the velocity profile at pore throat will be less at the center.

Figure 4.11 compares the pressure force and normal stress force as *De* increases for fixed flow rate boundary condition and constriction geometry. As *De* increases, the normal stress force increases, but the pressure force at *De* = ~3 starts to decline. However, the total force (which is the summation of pressure force and normal stress force) increases with *De*. The normal stresses increase by a factor of more than 200 and the total normal force increases by a factor of more than 20 between *De* = 0 and *De* = 5.0. Although it cannot be determined definitively, it is very possible that normal forces continue to increase at high *De*, dominate over pressure forces, and the total force continues to increase. These larger normal (and therefore total) forces may be enough to overcome capillary forces and mobilize residual oil in porous media. More likely, it is one of many synergistic factors mobilizing residual oil. For example, the additional viscosity of the polymer would add additional pressure drop and the asymmetry of the flow lines could lead to ganglion pulled off of the droplet.

Figure 4.12 shows the pressure force and normal stress force for the fixed pressure boundary condition in the constriction geometry. As shown, the normal stress force increases monotonically as *De* increases, but the pressure forces decrease. In figure 4.12 the total normal force is declining in the range of *De* studied, but if the normal force were to increase monotonically, it would eventually dominate the over pressure force, and total force would also increase. It should also be noted that as the droplet approaches the constriction it would in reality deform. The asymmetric forces on the deformable droplet may be large enough to pull the front end of the droplet into the constriction or tear off ganglion from the droplet. More advanced modeling would be required to study flow around a deformable droplet and test these hypothesis.

It should also be noted that the constant pressure boundary condition is less realistic than the constant rate boundary condition, since polymers are typically injected into wells at constant rates.

4.2.3 Oil Droplet Close to the Constriction

To analyze how various forces changes as the oil droplet moving toward the constriction, a new geometry has been evaluated which is similar to the constriction geometry except the stationary oil droplet is now closer to the constriction (figure 4.1 (c)). CFD modeling has been performed for the oil droplet close to the constriction geometry and the results are discussed below.

Figure 4.13 shows the normal stresses around an oil droplet (as a function of θ). Two geometries are depicted in figure 4.14; one has the droplet relatively far from the constriction and the other has a droplet much closer. In both cases, normal stress forces are larger for the viscoelastic fluid than for the Newtonian counterpart (figures 4.13 and 4.14). This is the same conclusion that normal forces on the droplet are significant when the invading fluid is elastic but insignificant for inelastic fluids. It is also shown here in figures 4.13 and 4.14 the stresses are orders-of-magnitude larger near for the droplet near the constriction. These stresses are especially large near $\theta = 180°$, which might suggest that the elastic nature of the polymer can mobilize the droplet by pulling the non-wetting fluid into the constriction.

4.2.4 Mixed-Wet Medium

All previous static simulations were performed for water-met media; to analyze the viscoelastic behavior for mixed-wet wettability, a new geometry is used as shown in figure 4.1 (d). CFD modeling been done for the mixed-wet geometry and the results are discussed below.

Figures 4.15 and 4.16 depict idealized sinusoidal geometries in mixed-wet systems (oil droplets are attached to the pore walls). Similar observations can be made here as for the water-wet media. In figure 4.15, the normal stresses are much more significant for the viscoelastic fluid (De = 1.5) compared to the Newtonian injecting fluid. The effect on the flow field is further evidenced in figure 4.16, which shows the pressure field in the two simulations.

4.3 Conclusions

Pressure gradient alone is not sufficient to overcome capillary forces and mobilize residual oil in reservoirs, even with the increased viscosity of polymers. The recent experimental and field observations that show reduced residual oil in the presence of polymers such as HPAM must be due to other factors, or more likely, combination of forces acting on the oil droplet. CFD simulations of viscoelastic flow around static oil droplets in pore throats show that normal stress forces are insignificant for Newtonian fluids, but increase dramatically with *De*. In some cases the total forces imposed on the oil droplet is much larger as a result of these normal forces, even at the moderate *De* studied here. It is possible that at higher *De*, normal forces dominate and the effective force is much larger than a Newtonian fluid with the same viscosity and flow rate. It is concluded that the observed reduced residual oil is a result of a combination of factors including pressure drop from the high polymer viscosity, normal stress forces in the viscoelastic fluid, and perhaps ganglion pulled off of the droplet due to asymmetry in the flow lines. Future work should focus on modeling these effects in geometries that allow for shape evolution of the droplet as well as complimentary experiments in microfluidics tubes representative of pore throats.

Additionally, CFD simulations were performed in geometries intended to represent mixed-wet medium. The additional forces present for an elastic fluid which could mobilize

trapped oil in mixed-wet medium which is consistent with water-wet medium. Moreover, as the droplet approaches the constriction, the normal forces on the droplet increase further.

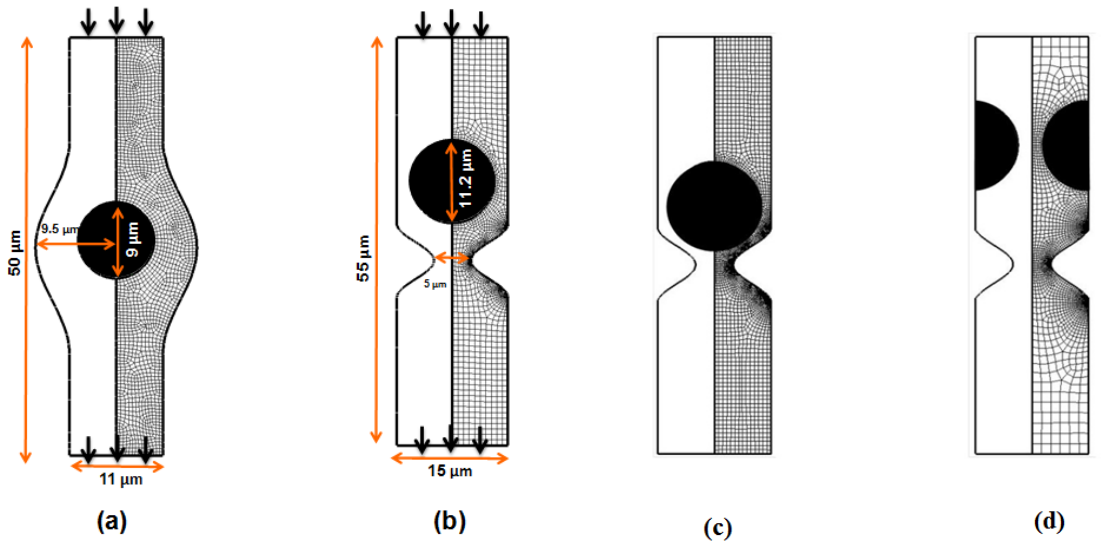

Figure 4.1 Schematic of simulation geometries and mesh arrangements for (a) pore-centered geometry, (b) constriction geometry, (c) oil droplet closer to the constriction compared with (b) with same geometry, (d) mixed-wet medium

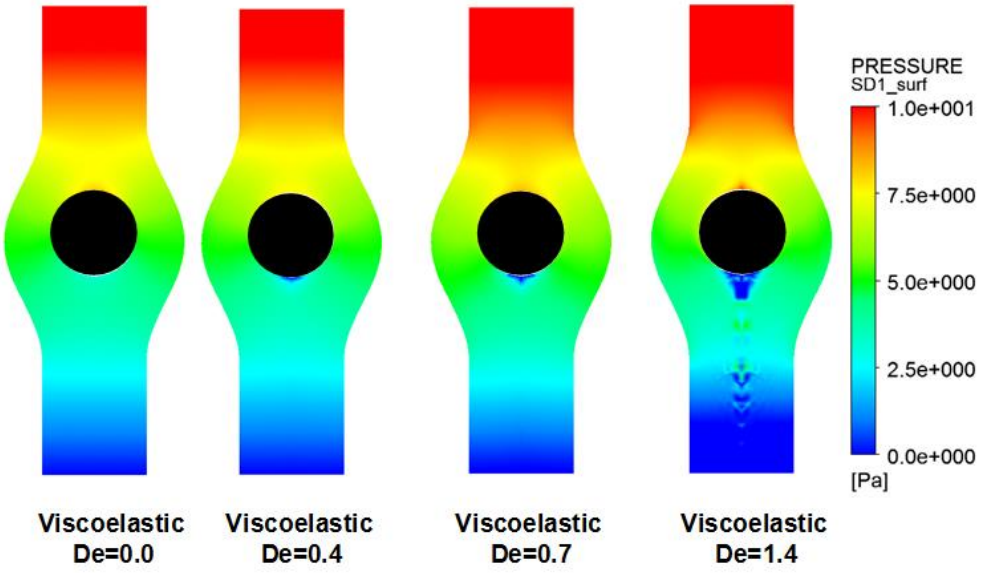

Figure 4.2 Pressure field in the pore throat for (a) Newtonian fluid (*De* = 0), (b) Viscoelastic fluid (*De* = 0.4), (c) Viscoelastic fluid (*De* = 0.7) (b) Viscoelastic fluid (*De* =1.4)

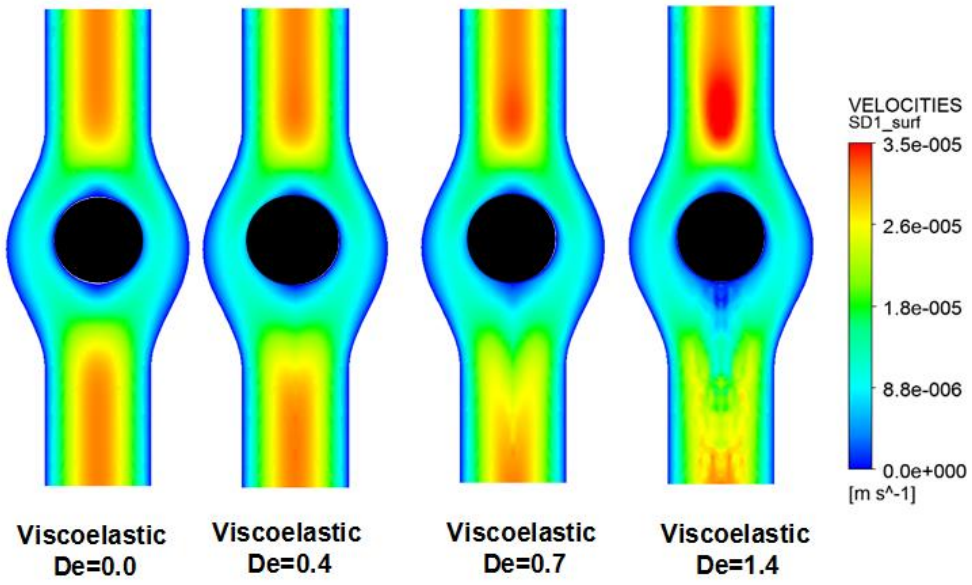

Figure 4.3 Velocity field in the pore throat for (a) Newtonian fluid (*De* = 0), (b) Viscoelastic fluid (*De* = 0.4), (c) Viscoelastic fluid (*De* = 0.7) (b) Viscoelastic fluid (*De* =1.4)

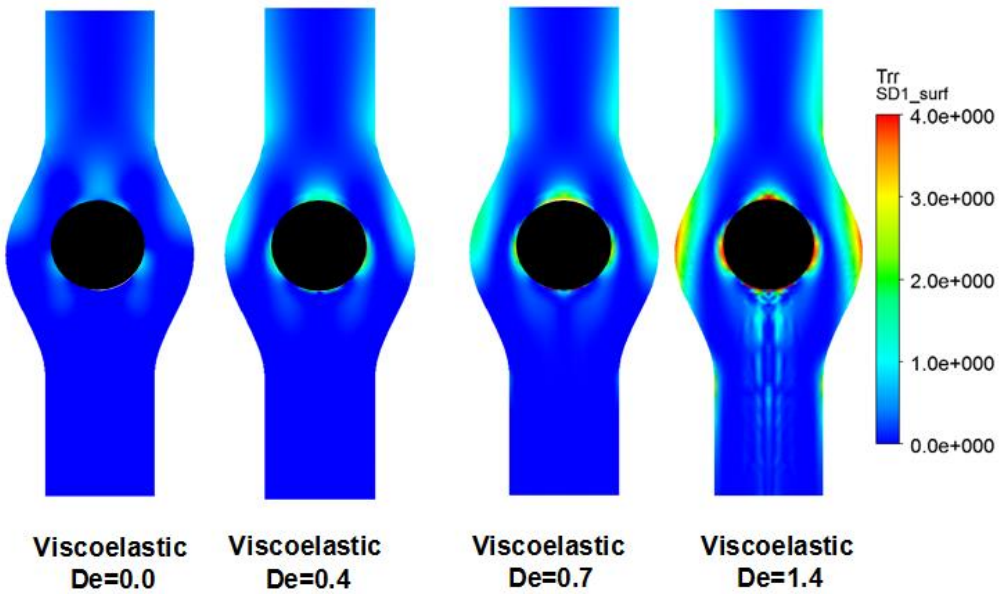

Figure 4.4 Normal stress field in the pore throat for (a) Newtonian fluid (*De* = 0), (b) Viscoelastic fluid (*De* = 0.4), (c) Viscoelastic fluid (*De* = 0.7) (b) Viscoelastic fluid (*De* =1.4)

Table 4.1 Summary of micro-forces presented on an oil droplet in the presence of Newtonian and viscoelastic fluids for the pore-centered geometry and fixed flow rate boundary condition

	VE, De=1.4	VE, De=0.7	VE, De=0.4	Newtonian
Overall Pressure Drop (Pa)	16.50	14.37	13.49	13.36
Pressure Drop across oil droplet (Pa)	28.88	21.38	9.86	6.05
Pressure Force (N)	4.82E-10	3.28E-10	2.91E-10	2.69E-10
Normal Stress Force (N)	2.65E-10	6.00E-11	7.33E-12	1.72E-11
Total (N)	7.47E-10	3.88E-10	2.98E-10	2.87E-10

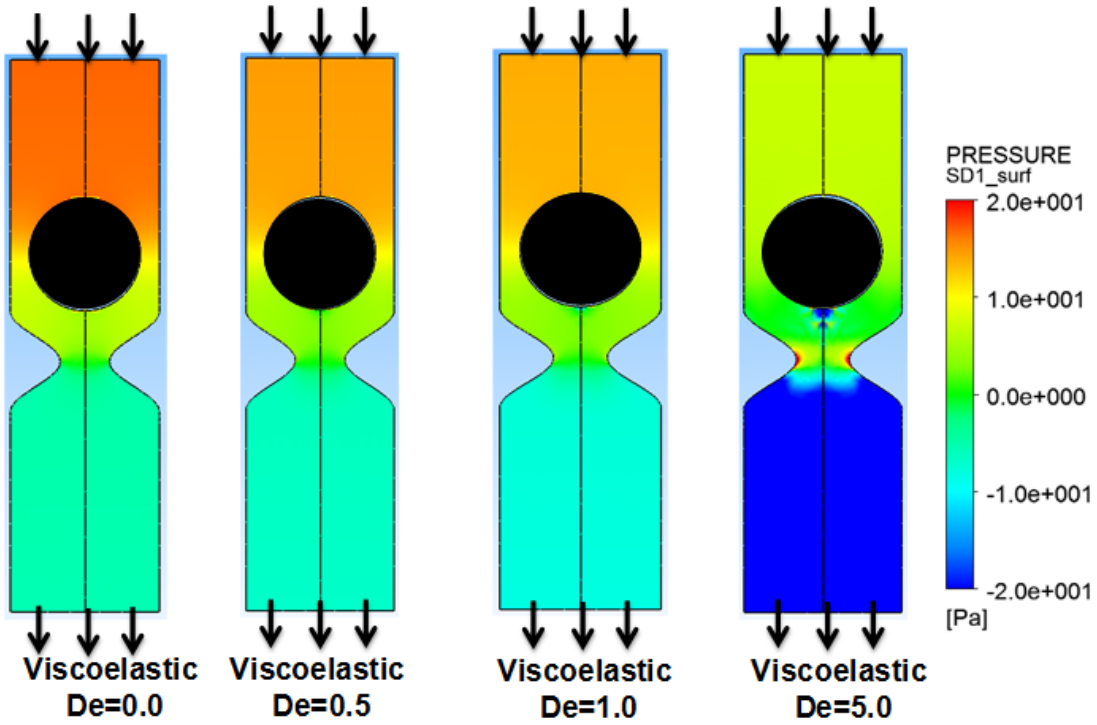

Figure 4.5 Pressure field in the pore throat for a (a) Newtonian fluid, (b) Viscoelastic fluid (*De* = 0.5), (c) Viscoelastic fluid (*De* = 1.0), and (d) Viscoelastic fluid (*De* =5.0)

Table 4.2 Summary of micro-forces presented on an oil droplet in the presence of Newtonian and viscoelastic fluids for the constricted geometry and constant flow rate boundary conditions

	VE, De=5.0	VE, De=1.0	VE, De=0.5	Newtonian
Overall pressure drop (Pa)	37.46	19.33	18.95	19.72
Pressure drop across oil droplet (Pa)	150.15	29.29	14.71	12.88
Pressure force (N)	7.84E-10	1.01E-09	1.06E-09	1.08E-09
Normal stress force (N)	1.00E-09	1.33E-10	1.07E-10	8.49E-11
Total (N)	1.78E-09	1.14E-09	1.17E-09	1.17E-09

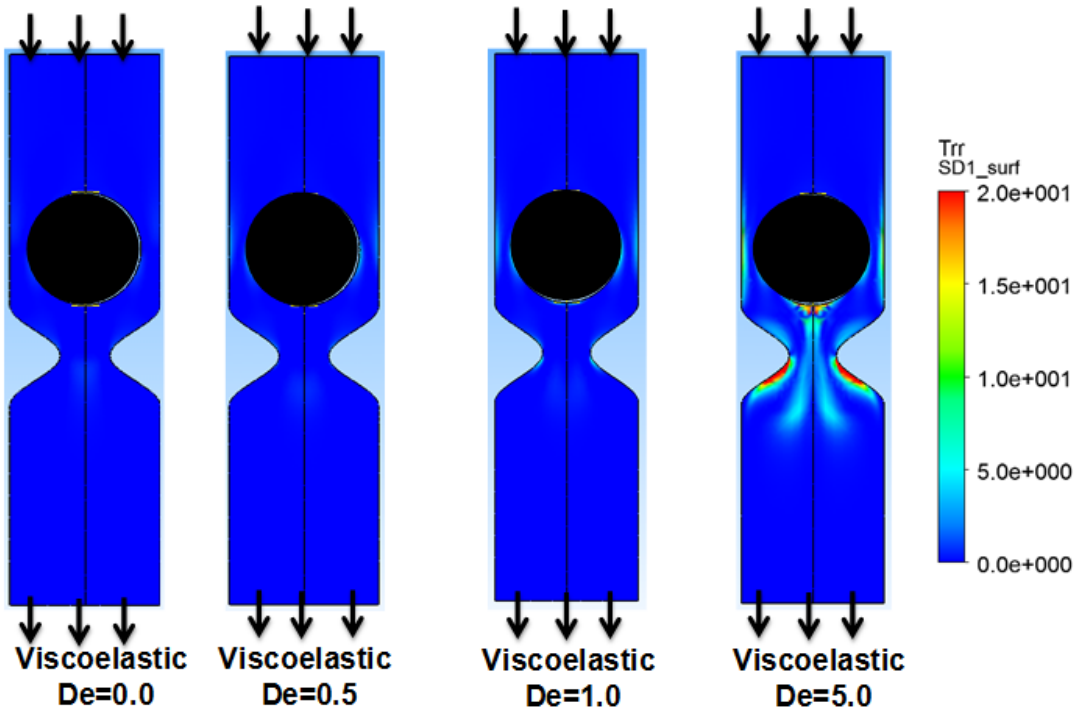

Figure 4.6 Normal stresses in the pore throat for a (a) Newtonian fluid, (b) Viscoelastic fluid, (*De* =0.5) (c) Viscoelastic fluid (*De* =1.0) and (d) Viscoelastic fluid (*De* =5.0). The uni is Pa.

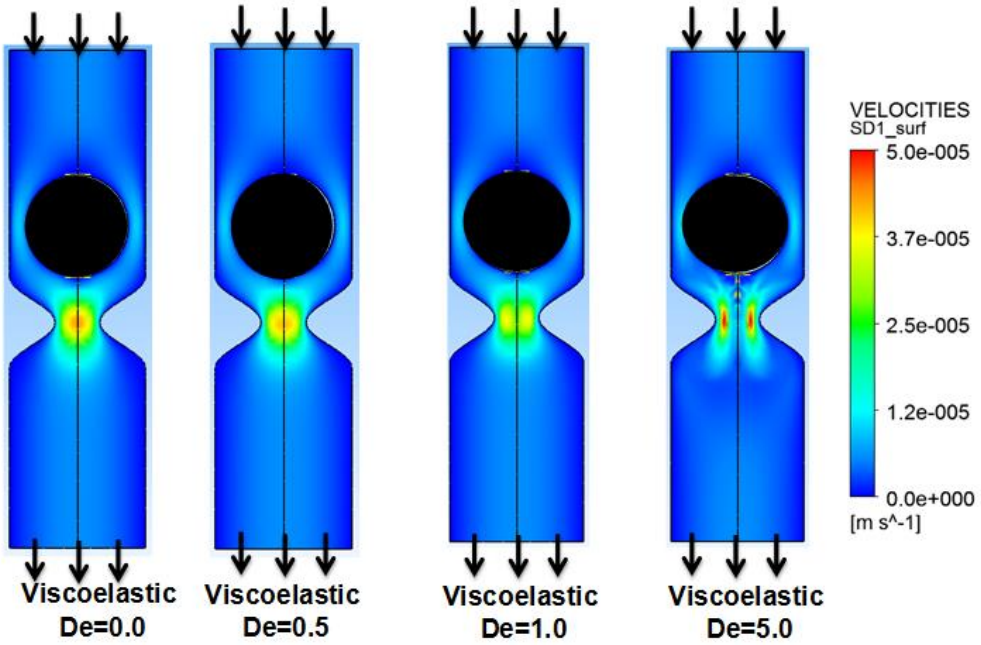

Figure 4.7 Velocity field in the pore throat for a (a) Newtonian fluid, (b) Viscoelastic fluid (*De* = 0.5), (c) Viscoelastic fluid (*De* = 1.0) and (d) Viscoelastic fluid (*De* = 5.0)

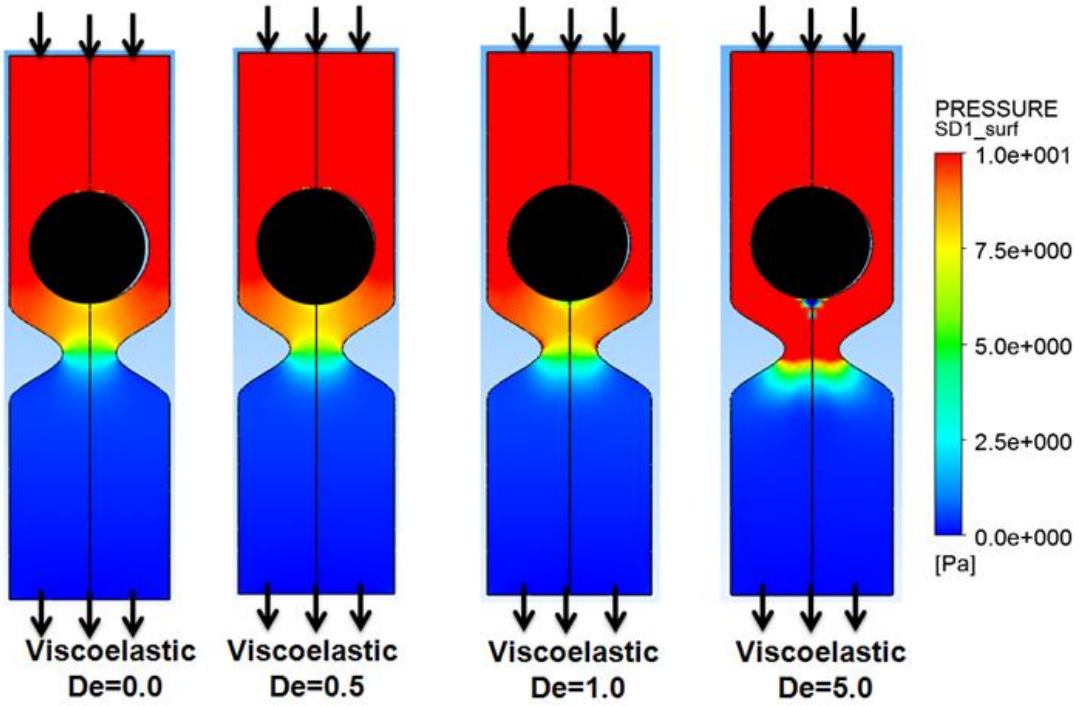

Figure 4.8 Pressure field in the pore throat for a constant pressure boundary condition in the constriction geometry for a (a) Newtonian fluid, (b) Viscoelastic fluid, De = 0.27, (c) Viscoelastic fluid, De = 0.54, and (d) Viscoelastic fluid, De = 2.68

Table 4.3 Summary of micro-forces presented on an oil droplet in the presence of Newtonian and viscoelastic fluids for a constant pressure boundary condition in the constriction geometry

	VE, De=2.7	VE, De=0.53	VE, De=0.27	Newtonian
Inlet flow rate (m^3/s)	2.6E-16	4.1E-16	4.1E-16	4.0E-16
Pressure Drop across oil droplet (Pa)	56.89	18.63	18.63	9.41
Pressure Force (N)	5.97E-10	8.97E-10	8.97E-10	8.95E-10
Normal Stress Force (N)	4.39E-10	1.38E-10	1.35E-10	6.92E-11
Total (N)	10.36E-10	10.35E-10	10.32E-10	9.64E-10

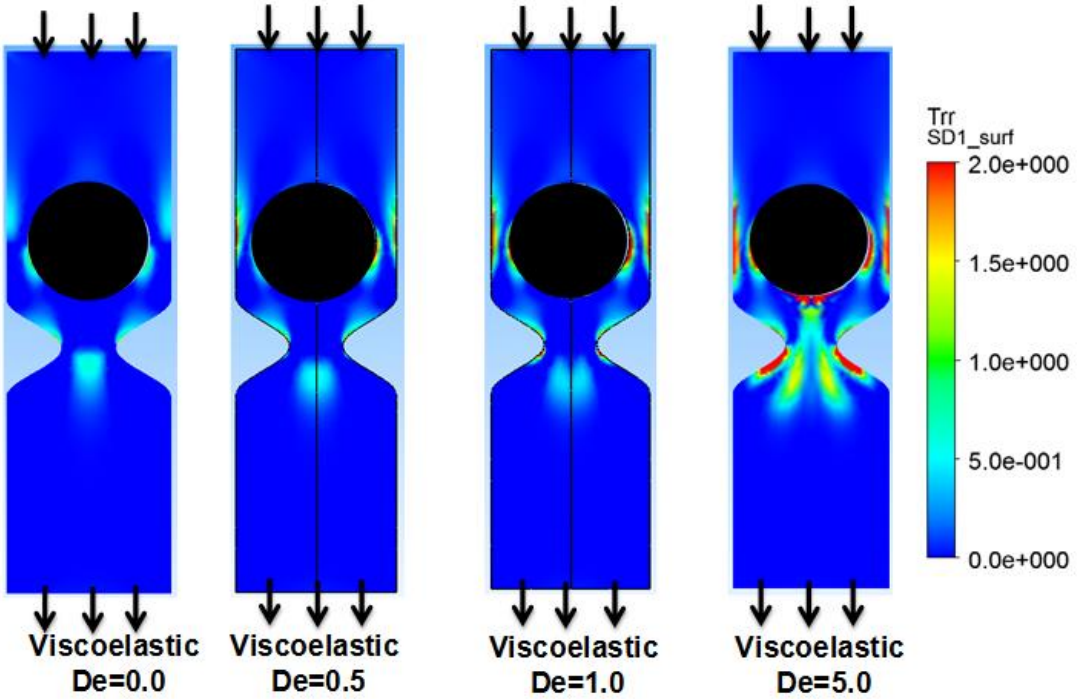

Figure4.9 Normal stresses in the pore throat for a constant pressure boundary condition in the constriction geometry for a (a) Newtonian fluid, (b) Viscoelastic fluid (*De* = 0.27) (c) Viscoelastic fluid (*De* = 0.54) and (d) Viscoelastic fluid (*De* = 2.68)

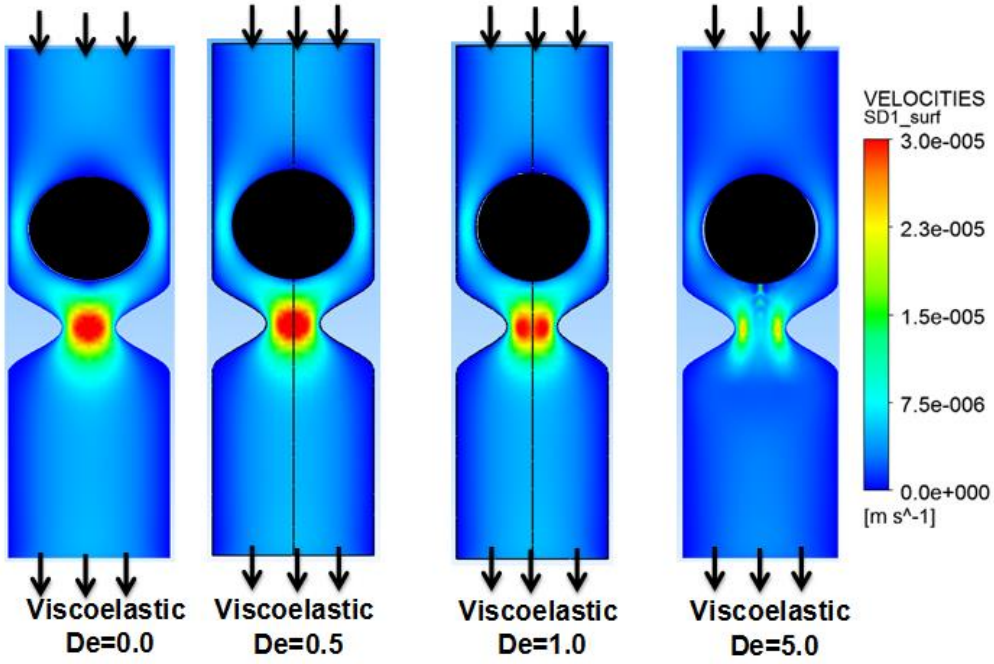

Figure 4.10 Velocity field in the pore throat for a constant pressure boundary condition in the constriction geometry for a (a) Newtonian fluid, (b) Viscoelastic fluid (*De* = 0.27) (c) Viscoelastic fluid (*De* = 0.54) and (d) Viscoelastic fluid (*De* =2.68)

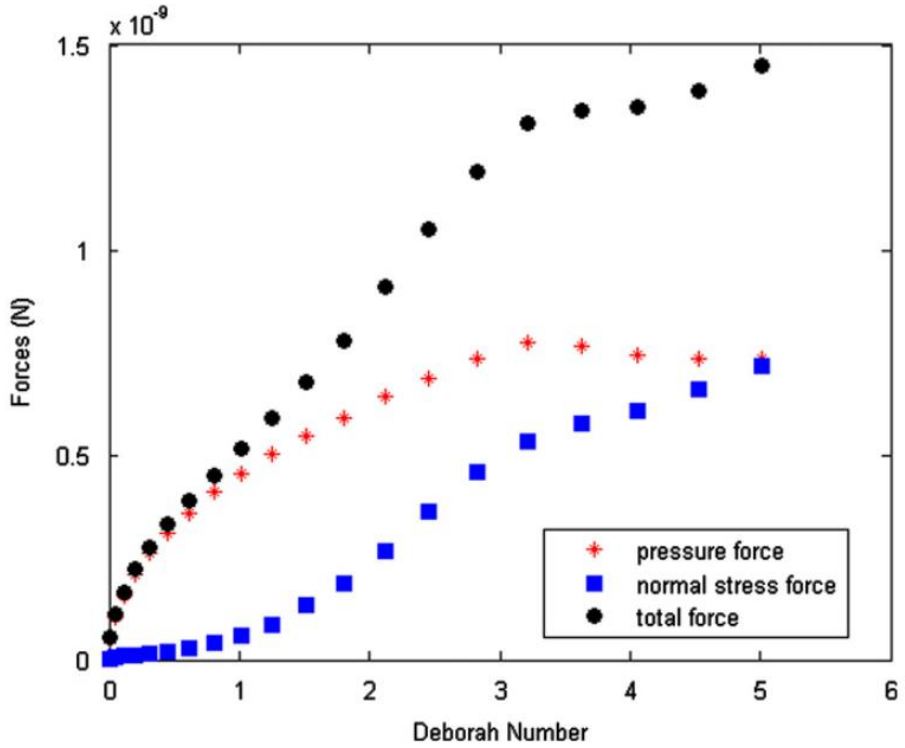

Figure 4.11 pressure force, normal stress force and total normal force vs. *De* number for constriction geometry and fixed flow rate inlet/outlet boundary condition

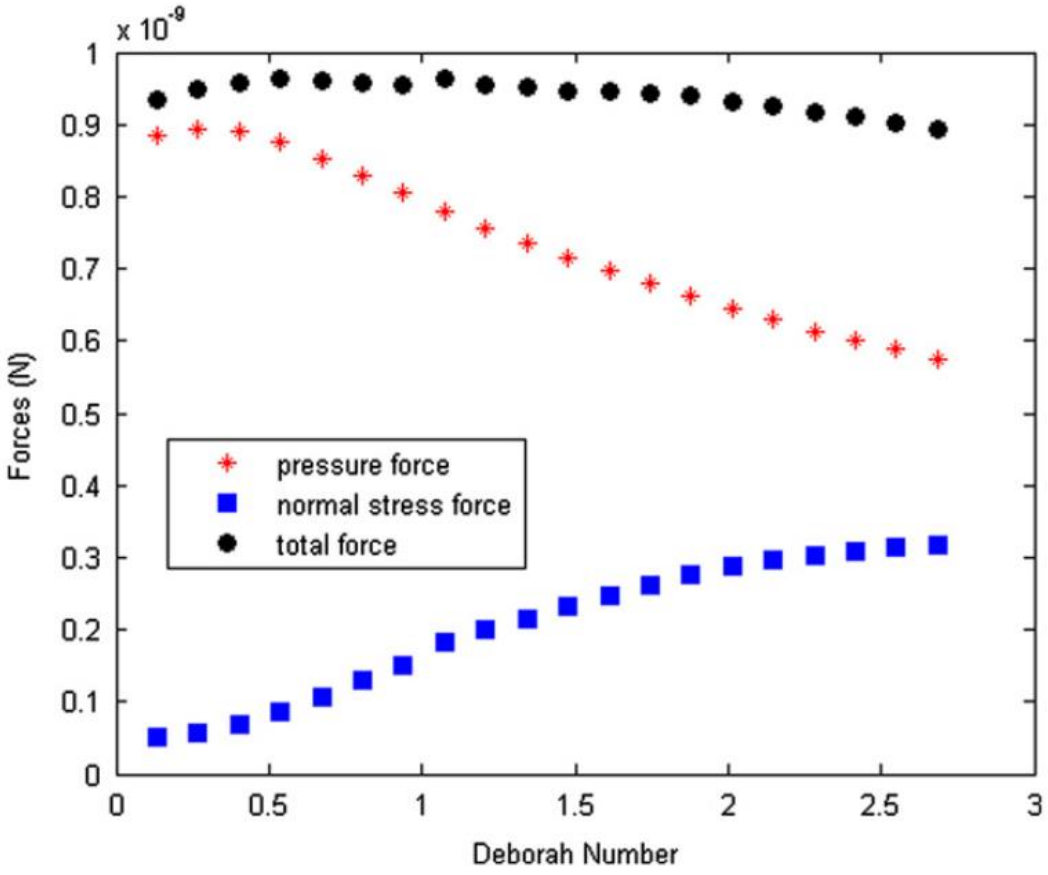

Figure 4.12 pressure force, normal stress force and total normal force vs. *De* number for constriction geometry and fixed pressure inlet/outlet boundary condition

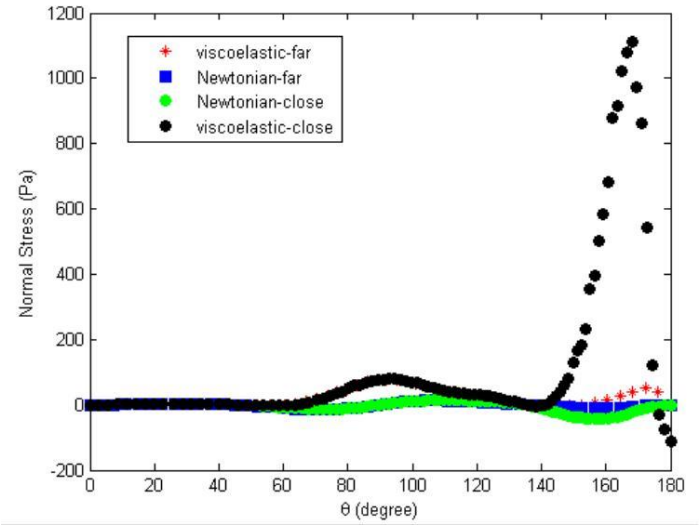

Figure 4.13 Normal stresses around droplet (function of θ). Stresses are much higher for viscoelastic especially for the droplet close to the throat

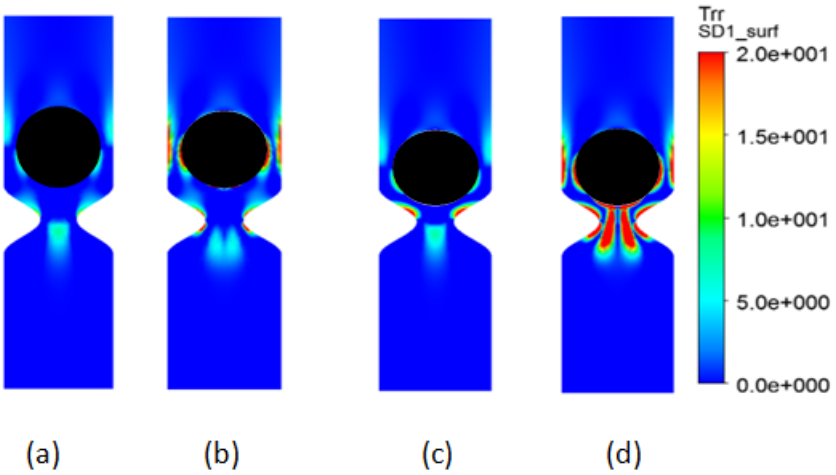

Figure 4.14 Normal stress field around droplet for (a) Newtonian, far from throat, (b) VE, far from throat, (c) Newtonian close to throat, and (d) VE close to throat

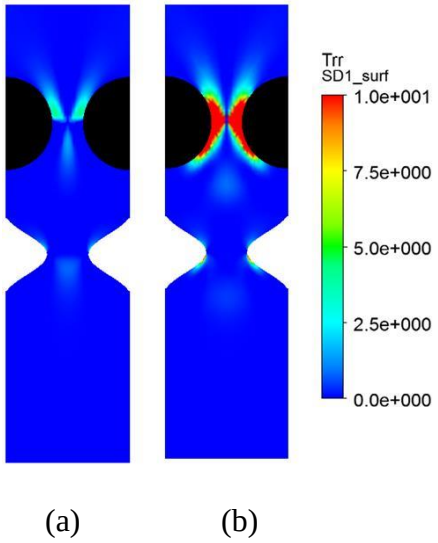

Figure 4.15 Normal stress field around droplet for (a) Newtonian and (b) viscoelastic fluids (De = 1.5)

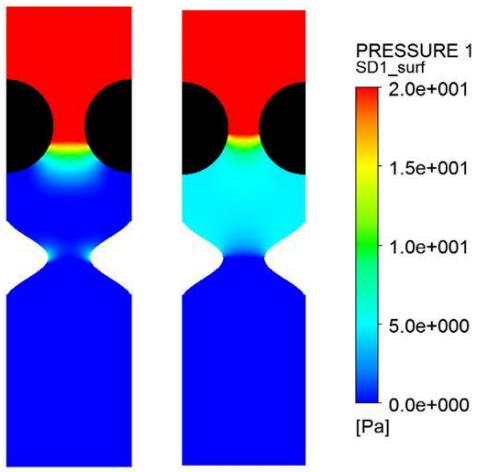

Figure 4.16 Pressure field around droplet for (a) Newtonian and (b) viscoelastic fluids (De = 1.5)

Chapter 5: Dynamic CFD Modeling of Viscoelastic Flow and Validation against Micro-Scale Experiments in Dead-End Pores[1]

In this study, existing micro-scale experiments were used to validate models and prove or disprove the hypothesis of a viscoelasticity pulling-effect to remove residual oil saturation. Steady-state (static) CFD modeling was performed in the dead ends of a channel to analyze the flow characteristics of viscoelastic polymer. The streamlines, velocity contours, and normal stress contours are discussed here. Both, experimental and steady-state simulation results show that the oil can be barely mobilized in normal reservoir conditions mimicked by the micro-scale experiments.

Additionally, transient (dynamic) CFD modeling was performed to gain a better understanding of oil droplet movement and deformation in a dead-end geometry. The Arbitrary Lagrangian-Eulerian (ALE) finite-element formulation is used to keep track of the interface between oil and the displacing fluid. The dynamic simulation results are in agreement with static simulations and experimental results.

This study shows that with typical properties of viscoelastic polymers, the pulling-effect is not a primary mechanism for reducing residual oil saturation. However, methods for increasing of the Deborah number through potential means, such as using polymer with higher relaxation time, may result in a more significant pulling effect and thereby recover residual oil. It is shown using dynamic simulations that the amount of deformation of the oil droplet is greatly

[1] This chapter is published in two papers as listed below: (1) Afsharpoor, A., Balhoff, M.T., "Static and Dynamic CFD Modeling of Viscoelastic Polymer; Trapped Oil Displacement and Deformation at the Pore-Level," Annual Technical and Conference Exhibition, SPE 166114-MS, New Orleans, Louisiana, October 2013. Balhoff, M.T. has contributions on the main idea and the geometry has been studied. (2) Afsharpoor, A., Ma, K., Mateen, K., Duboin, A., Jouenne, A., Cordelier, P., "Micro-Scale Experiment and CFD Modeling of Viscoelastic Polymer; Trapped Oil Displacement and Deformation at the Dead-End, " 19th SPE IOR Symposium Polymer session, SPE 169036-MS, Tulsa, Oklahoma, April 2014. The experimental work has been done by Jouenne. Ma, Mateen, and Cordelier have contributions on the main idea and the geometry has been studied.

affected by the elasticity of the displacing fluid. These results are promising and provide a theoretical foundation for the laboratory and field observations of reduced residual oil.

5.1 Methodology

5.1.1 Governing Equations

Polymers have elastic properties to varying degrees. A viscoelastic fluid has intrinsic rheological properties which make it behave as a viscous liquid as well as an elastic solid. The most commonly used polymer in chemical EOR/IOR projects, Partially Hydrolyzed Polyacrylamide (HPAM), is a straight-chained polymer of acrylamide monomers, some of which have been hydrolyzed which has an elastic characteristics (Sorbie, 1991). To measure the effect of polymer elasticity, a dimensionless group called Deborah number (*De*) is used as discussed before. In this study the Upper-Convected Maxwell equation (equation 2.24) is used to model strong extensional flow effect to relate the shear stress with the shear rate.

5.1.2 Steady-State (Static) Simulations

In this study two approaches were employed to understand the polymer elasticity effect at the pore-level. The first approach was steady-state simulations. Steady-state simulations performed in this study presumed a stationary oil droplet (e.g., a solid obstacle with rigid surface). In figure 5.1 the dead-end geometry is shown as one type of residual oil distribution (Wang, 2000).

The hypothesis to reduce S_{or} during the injection of viscoelastic polymer due to the pulling effect at a dead-end pore is investigated here. In this chapter, experimental studies were done by colleagues at *Total* and simultaneously the modeling performed (Afsharpoor et al., 2014), and interesting observations are reported. Steady-state simulations were done for the dead-end geometry in a 2D-planar scheme and the mesh configurations are shown in figure 5.2.

In most cases an unstructured mesh was developed to obtain better accuracy for the part where the more complicated physics occurred. The fluid flowed from left to right in figure 5.2 (a) and (b) and no-slip boundary conditions were employed for the walls. In figure 5.2(a) the triangular dead-end geometry has 200 μm in width and 270 μm in depth, and the flowing channel is 200 μm in width. In figure 5.2(b) the square dead-end geometry has 200 by 200 μm, and the flowing channel is 200 μm in width. The oil droplet inside the dead-end geometry was assumed to be stationary, so it did not move or deform. To perform the sensitivity analysis other geometries were investigated as discussed in the results and discussion section. Polymer properties from the experiments were chosen as a base case and other parameters were studied to have a better understanding on key parameters and the condition that we are able to observe the trapped oil being mobilized. The problem was solved using the finite element method (FEM) with DEVSS-SU formulation. In this study, Ansys Polyflow software was used to solve this complicated numerical problem. Sensitivity analysis is necessary to determine the best mesh network. The fluid elasticity was modeled by the upper-convected Maxwell model (UCM) with rheological properties of λ = 0 to 0.25 s and μ = 40 cp (0.04 Pa·s). The *De* number can be controlled by changing either the relaxation time (done here) or the inlet/outlet flow rate across the throat.

5.1.3 Transient (Dynamic) Simulations

The second approach was to perform transient simulations in which the oil droplet could be mobilized and the interface between oil and aqueous phases could be deformed due to the forces acting on it. The static modeling method is a steady state simulation to evaluate the behavior of viscoelastic fluid passing around the oil droplet; the oil droplet is stationary and the oil/displacing fluid interface does not deform. However, the dynamic modeling performed here is transient which keeps track of oil droplet movement and deformation.

5.1.3.1 Straight Capillary Tube

The geometry is again 2D axisymmetric for the two phase system. Conservation equations (continuity and momentum) have been solved for both the oil phase as well as for displacing fluid phase (water or water-based fluid). The oil droplet is a Newtonian fluid as is water, but an Oldroyd-B model is employed when the displacing fluid is viscoelastic. No slip boundary conditions for all wall boundaries and fixed inlet/outlet flow rate has been chosen. The geometry is shown in figure 5.2(d) and is a simple capillary tube. Although this geometry is extremely simple, and does not depict a throat constriction, it does provide insight into the deformation of a droplet when inelastic and elastic fluids flow past it.

A moving interface boundary condition is used for the interface between oil droplet and displacing fluid to be able to capture the interface deformation and movement. Due to the droplet movement and the interface deformation, mesh configuration plays an important role. Thus, a re-meshing technique is used for the moving interface. The purpose of re-meshing is to relocate internal mesh nodes according to the displacement of boundary nodes. Re-meshing techniques control mesh deformation in order to avoid unacceptable element shape. There are different re-meshing methods, in order to satisfy the re-meshing requirements for a variety of flow problems such as method of spines, Euclidean method, Thompson transformation, elastic method, and so on (Ansys Polyflow User's Guide, 2012). Re-meshing rules that are topologically general (i.e. Thompson transformation and elastic method) will require more CPU time and memory than those that apply only to specific topologies, because they involve the wider coupling between the position variables and the other solution fields. Each re-meshing techniques is designed to work well for a certain class of problem. Different re-meshing methods have been tested; finally elastic re-meshing is chosen to be the best for this problem. Generally, elastic method is

recommended for cases where the inherent topological complexity makes it difficult or even impossible to apply topologically-regular methods.

In a transient simulation, the mesh elements will be deformed and stretched such that they require re-meshing through the process. Therefore, a mesh at the start of the simulation is no longer adequate later on the simulation. The adaptive meshing technique has been applied to address this issue. When adaptive meshing is used, the quality of the mesh is evaluated at regular intervals during the transient simulation. For each element, if the current quality is below a specified threshold, then the element is selected for refinement and displacement.

5.1.3.2 Converging-Diverging geometry

The boundary condition was similar to that in steady-state simulations except for a new boundary condition on the interface between the oil droplet and the displacing fluid. The pore geometry was a converging-diverging tube. A moving interface on the interface between oil and polymer fluids was used rather than a fixed interface. For a moving interface, a kinematic condition was added to the system of equations in order to solve for the position of the interface. The geometries and finite element meshes for simulations of converging-diverging geometry are shown in figure 5.2(c). In figure 5.2(c) the tube has 40 μm in radius, however because the scheme is axi-symmetric along the center of tube, only half of the geometry is shown, and the radius at the constriction is 30.5 μm. The mesh around the moving oil droplet is much finer to be able to capture the interface precisely. The converging-diverging geometry was selected to investigate how the droplet was deformed and passed through the constriction, and whether snap-off would occur in different fluid properties by specifically comparing viscoelastic fluids with Newtonian fluids.

5.1.4 Free Surface and Free Boundary Tracking

In transient flows the movement of an interface occurs. Accurately capturing the interface and keeping tracking the movement and deformation of the free interface is a challenge in FEM. In general there are two methods to capture the free surface: Eulerian and Lagrangian methods. We briefly introduce them here.

In Eulerian flow fields and mesh techniques, meshes are stationary and fixed. The mesh nodes are fixed and material flows through the mesh. Eulerian coordinates of nodes are fixed and coincide with spatial points, and spatial coordinate of material points vary with time as shown in figure 5.3.

The material point at a given quadrature point changes with time, which makes it difficult to deal with history-dependent materials. Boundary nodes and material boundaries may not coincide. Therefore, boundary conditions and interface conditions are difficult to apply. There is no mesh distortion because the mesh is fixed in space. However, the domain that needs to be modeled is larger compared with Lagrangian approach because we do not want the body to leave the domain. In contrast, in Lagrangian flow fields and mesh technique, the mesh is moving and attached to the material as shown in figure 5.4.

Lagrangian coordinate of nodes moves with the material and the material coordinate of material points are time invariant. No material passes through the elements. Element quadrature points remain coincident with material points. More importantly, boundary nodes remain on the boundary in order to keep track of the interface more precisely. Therefore, boundary conditions and interface conditions are easily applied. The disadvantage of this method is that severe mesh distortions can occur because the mesh deforms with the material. To overcome the mesh distortion, a re-meshing technique can be applied. The purpose of a re-meshing technique is to relocate internal nodes according to the displacement of boundary nodes. Re-meshing techniques

control mesh deformation in order to avoid unacceptable element shapes. There are different re-meshing methods according to the physics of the problem. Elastic re-meshing methods has been selected for this study (Ansys Polyflow User's Guide, 2012). The Arbitrary Lagrangian-Eulerian (ALE) method takes advantage of both Lagrangian and Eulerian approaches. The mesh movement is arbitrary to have an optimum shape of element to track the boundaries and interfaces precisely. It can model the wettability; however, it cannot simulate capillary pressure like when a droplet is immersed in another liquid. The limitation of this method is that it is not good for abrupt topology changes and splitted interfaces. All dynamic (transient) simulations in this study used ALE method.

5.1.5 Dead-End Microfluidic Experiments

5.1.5.1 Micro-fabrication

All experiments were performed in microfluidic systems to model the dead-end geometry (Afsharpoor et al., 2014) and performed by colleagues. The microsystem is composed of a main channel (width, w = 200 μm) and a dead-end pore connected to the main channel through one side only. By varying both the angle α and the length L_P of the pore, we obtained 4 different shapes: square, deep rectangle, short triangle, deep triangle (see figure 5.5). The whole system height is h = 60 μm.

The microsystems are made by conventional PDMS replica molding of a photolithographied SU-8 mold (SU-8 2100, Microchem) (Duffy et al., 1998). Briefly, PDMS was poured on the mold and submitted to thermal curing for two hours in an oven at 70 °C. Then the replica is removed from the mold, drilled and treated with oxygen-plasma before sealing by a glass coverslip. To get a water-wet condition the system is used immediately after sealing, whereas for an oil-wet condition, the systems is placed in the oven at 70 °C for at least 24 hours before use.

5.1.5.2 Experimental Sequence

The system is connected through small tubing (Tube PEEK 1548, Idex Health and Science) to a syringe pump (Pump 11 Elite, Harvard Apparatus) in order to inject the fluids at a constant flow rate, typically between 0.2 and 100 µL/min. A 2-entry-valve (V-100 L valve, Idex Health and Science) placed between the syringe pump and the system allows to perform sequential flooding and to avoid air bubble troubles. The system is placed on an illumination lamp and observed from above through an optical length connected to a color camera (PixeLINK) allowing image sequence acquisition.

In order to investigate oil recovery processes in dead-end geometries, each experiment requires three steps as shown in figure 5.6. First of all, the investigators performed oil flooding to fill out the geometry. Then, we inject an aqueous solution to trap oil in the pore (oil trapping assays). Finally, a complex fluid solution is injected to investigate the trapped oil recovery from the dead-end geometry (oil detrapping assays).

5.1.5.3 Fluid Properties

The aqueous solutions used in the trapping assays are deionized water (DW) and a 1% v/w sodium dodecyl sulfate aqueous solution (SDS) (L6026, Sigma Aldrich). The complex fluid solution is a 4,000 ppm or 8,000 ppm polyethylene oxide solutions (PEO) (M_w = 5 MDa, 189472, Sigma-Aldrich). To prepare the PEO solution, the polymer powder is homogeneously dispersed during a few seconds in a vortex of 200 mL of water created by magnetic stirring. The solution is then gently agitated on a moving table during overnight to achieve dispersion of the polymer without breaking the molecules. The solution is finally homogenized by magnetic stirring during two hours at 100 rpm. The oil phase is commercial fluorinated oil (FC-40 Fluorinert, 3M) that does not swell the PDMS. So as to ease visualization, aqueous solution is

colored with water-soluble dyes: fluorescein (yellow) (46955, Sigma Aldrich) or methylene blue (blue) (M9140, Sigma Aldrich).

5.1.5.4 Characteristic Number of the Flows

In order to compare all the different experimental conditions, the flow is characterized by three dimensionless numbers. The capillary number *Ca* is describe by equation 5.1, where μ is the zero-shear-rate viscosity of the injected fluid, *U* is the mean velocity of the flow, and γ the interfacial tension between the two fluids. *Ca* expresses the balance between the capillary forces that are responsible for the trapping phenomena of oil in the reservoirs and the viscous forces which account for the dragging effect of oil by the injected fluid. In our experimental condition, we are able to approach a range of capillary numbers close to the typical one encountered in oil reservoir.

$$Ca = \frac{\mu U}{\gamma} = \frac{\mu}{\gamma}\frac{Q}{wh} \tag{5.1}$$

The Deborah number (or Weissenberg Number (*Wi*), equivalently) is described by equation 5.2 as introduced previously. The reciprocal of t_r is expressed here as *U*/*L* in equation 5.2 as an estimation of the shear rate applied to the polymer chain in the flow. *L* is the characteristic length of the elongation represented by the width of the main channel here.

$$De = Wi = \lambda\frac{U}{L} = \lambda\frac{U}{w} = \lambda\frac{Q}{w^2 h} \tag{5.2}$$

While *De* << 1 the characteristic time of the elongation is larger than the characteristic time of the polymer chain: the chain fully relaxes the strain and no elastic effect is observed. When *De* > 1, the polymer chain is stretched and the elastic effect should be observed. In addition, the Reynolds number (*Re*) is defined as the ratio of inertia forces to viscous forces as shown below:

$$Re = \frac{2\rho Q}{\mu(w+h)} \tag{5.3}$$

where ρ is fluid density, Q is volumetric flow rate, and μ is fluid viscosity.

5.2 Results and Discussion

5.2.1 Steady-State (Static) Simulations

Figure 5.7 shows the velocity streamlines for three different cases. In all cases the displacing fluid (generally, polymer) displaces the trapped oil droplet as shown in black color. Case (a) is the Newtonian base case with a flow rate of 100 μL/min, a Reynolds number of 0.53, a Newtonian displacing phase (relaxation time (λ) equals zero) viscosity of 23 mPa.s, and a displaced phase viscosity of 24 mPa.s. Case (b) is the viscoelastic base case in which the fluid properties are the same as the Newtonian base case, but the displacing fluid relaxation time is 0.35 sec. Case (c) is the viscoelastic case with 48 times higher flow rate than the viscoelastic base case (case (b)).

Table 5.1 summarizes the fluid properties and experimental parameters. Note that *Ca* is not calculated because single-phase flow is investigated here and the oil droplet is treated as a stationary obstacle. As shown in figure 5.7, the velocity streamlines in case (a) and (b) are very similar to each other and they do not go through the dead-end part and barely touch the trapped oil droplet.

Figure 5.8 shows the velocity contours for the same three cases as those in figure 5.7. As it shows the velocity contours for case (a) and (b) are similar. By comparing the results for case (a) and (b) we can conclude that the experiment condition corresponding to case b with viscoelastic behavior is very similar to case a with Newtonian behavior, so lack of enough pulling effect to extract oil from the dead-end section is expected. The pulling forces is calculated and for case (a) the total pulling force is 1.321E-10 N, and for case (b) is 1.315E-10

N. As expected the total pulling forces for both case (a) and (b) are very close and for both cases (a) and (b) the pulling force due to normal stress itself is negligible (4.75E-14 N).

However, by increasing the flow rate we observe a more pronounced pulling effect as shown in case c of figure 5.8, where the velocity contours invade toward the oil droplet. This increase in the flow rate results in an increase in *De*; alternatively, one can also increase *De* by increasing the elastic property of polymer through an increase in the relaxation time.

Figure 5.9 shows the normal stress contours for the Newtonian base case by comparing the tension and compression components of normal stresses. As it shows, tension and compression components are almost similar and are very close to zero based on the given scale bar; therefore, the pulling effect does not occur for the Newtonian case.

However, the normal stress components are different for case c as shown in figure 5.10. As figure 5.10 shows the tension component is much higher than the compression component, causing net tension forces and the pulling effect observed for this case.

Figure 5.11 shows the normal stress contours for case (b). As it shows it is consistent with our previous observation that the pulling effect is negligible in case (b) because the tension and compression components of normal stress cancel each other.

Figure 5.12 shows the difference in all three cases and how the tension is dominant for case (c), which explains why in experiments the pulling effect is not observed for case (b). In general the driving fluid used for the viscoelastic base case is the polymer with a high relaxation time (PEO 4000 ppm, relaxation time = 0.35 s). Another dead-end geometry investigated in this study is the shallow square. The reason to model this geometry is that it may have a sudden change in flow path which leads to a higher elasticity, and if so how significant the effect would be. Thus this level of elasticity may possibly be able to extract the trapped oil in the dead-end

part. Figure 5.13 shows the normal stress contours for the Newtonian base case to compare the tension and compression components of normal stresses. As it shows, tension and compression components are almost similar; therefore, the pulling effect does not occur for the Newtonian case with a square dead-end geometry either.

Figure 5.14 shows the normal stress contours for case (b). As it shows it is consistent with our previous observation of the negligible pulling effect in case (b) because the tension and compression components of normal stress cancel each other in the square geometry as well. Therefore, not being able to extract the trapped oil from this geometry in lab condition is reasonable.

Figure 5.15 shows the tension component is much higher than the compression component, resulting in a net tension effect and the pulling effect observed for this case.

Figure 5.16 shows the difference in all three cases and how the tension is dominant for case (c). As a result, in experiments the pulling effect is not observed for case (b).

However, comparing the normal forces acting on an oil droplet in the square geometry is more effective compared with the triangular geometry. The CFD modeling has been done for deep triangular and rectangular dead-end geometries and the results are consistent with shallow geometries; however, it is obviously more difficult for the viscoelastic polymer to reach the bottom of dead-end section compared with shallow geometries.

5.2.2 Experimental Results

5.2.2.1 Oil Trapping Assays

Our aim was to study the recovery process on residual oil in dead-ends. Thus, the first thing was to trap oil in a reproducible manner. We observe three main types of results during oil trapping assays: no trapping, partial trapping, full trapping (results are gathered in Table 5.2). It

turns out that our ability to trap oil depends on the wetting properties of the system and the shape of the pore (see figure 5.17). The wetting property of the system is quantified by the contact angle θ measured at the triple contact point between the water/oil meniscus and the wall of the system. Moreover, the behavior of this meniscus near the pore depends on the angle α (see figure 5.17(g) and 5.22(h)).

In fully water-wet systems, that is when we use SDS as the aqueous solution and $\theta = 0$ degree, a wetting film of SDS appears on the walls of the system. If this film propagates quicker than the meniscus in the system, oil is completely drained out from the pore. That explains why oil is completely de-trapped in short triangle or square pores (figure 5.17(a) and 5.17(b)) whereas it is trapped in deep triangle or deep rectangle (figure 5.17(e) and 5.17(f)).

When there is no surfactant in the aqueous solution, θ takes a finite value between 0 and 180°: we speak of partial wetting and we distinguish hydrophilic partial wetting ($0 < \theta < 90°$) from hydrophobic partial wetting ($90 < \theta < 180°$). In both hydrophilic and hydrophobic partial wetting, when the meniscus reaches the pore, it encounters an abrupt slope change. Furthermore, the contact angle on the wall of the main channel must be equal to the one on the wall of the pore. To satisfy this condition at the anchoring point at the entry of the pore (point A on figure 5.17(g)), the apparent angle θ_{APP} takes all values between θ and θ_{max} ($\theta_{max} = \theta + \pi - \alpha$) before the triple contact line enters the pore. It is trapped at the point A and its penetration in the pore depends on the angles θ and α, and also on the time spent by the meniscus to reach the exit point of the pore (point B on figure 5.17(g)).

In partially water-wet systems (partial hydrophilic wetting) (figure 5.17(c)), the triple contact line can penetrate in the pore before the meniscus reaches the exit point of the core, leading to a partial trapping of oil in the pore. The amount of oil trapped in the pore depends only

on the angle α and the flow rate of the water solution: the smaller α, the more oil is trapped; the higher Q, the more oil is trapped. Thus the amount of oil trapped is greater in square pores than in short triangle pores.

In partially oil-wet systems (partial hydrophobic wetting) (figure 5.17(d)), the meniscus advances in the main channel in a piston-like manner and reaches the exit point of the pore before the trapped triple line could enter it, resulting in oil trapping in the pore.

5.2.2.2 Oil Detrapping Assays with Tertiary Polymer Flooding

We study the effect of polymer flooding on oil recovery of oil trapped in dead-ends, in fully water-wet and partially oil-wet systems, using respectively deep pore geometries and short pore geometries. As the presence of the pore induces an expansion-contraction in the section of the channel where the polymer solution flows, we expect streamline modifications on the sides of the pore due to elastic effects (Evans and Walters, 1986; Boger, 1987; Rodd et al., 2005; Rodd et al., 2007). Hence the polymer solution should develop normal forces near the pore and enter deeply in the pore which helps to drag out oil from the pore (Yin et al., 2006). However, despite varying the injection flow rates and the concentrations of the polymer solution, we never observe positive recovery effects of polymer solution (see figure 5.18). In our lab conditions, the amount of oil trapped in the pore is not affected by a tertiary polymer flooding.

The Weisenberg number calculated from our flow conditions are summarized in Table 5.3. Despite the fact *Wi* is greater than 1, we observe no effect of polymer on oil recovery in dead-end geometries. In all those experimental configurations, the capillary numbers are very low, due to low flow rates and the low scales involved by microfluidics. Thereby, the capillary forces, that are responsible for the oil trapping, dominate over the elastic forces that could have risen due to the non-linear behavior of the polymer solutions.

5.2.3 Transient (Dynamic) Numerical Simulations

5.2.3.1 Straight Capillary Tube

Although the static results are interesting and further support the hypotheses that elasticity provides additional forces that can mobilize residual oil (Chapter 4), the simulations were conducted in over-simplified geometries. Moreover, they involve steady flow around a static, snapped-off oil droplet. Many experimental data sets suggest that reduction in residual oil occurs in secondary and not tertiary floods (i.e. it is only effective before oil has snapped off). In this work, we have conducted preliminary dynamic simulations to study the effect of elasticity on the movement of an oil droplet.

The geometry used here is a cylindrical tube and is mathematically modeled in 2D axial symmetry. An oil droplet is placed at the center of the tube and the wetting fluid (water or oil) is injected from top to bottom. Figure 5.19 shows the normal stresses for (a) water and (b) viscoelastic fluid. The inelastic water deforms the oil droplet, while the elastic polymer adds some stability and the droplet remains virtually in its initial spherical shape. Note that the viscosity of both the polymer and water are the same.

The chosen geometry is kept simple, largely because of the strong nonlinearities of the problem, but work is recommended to model flow in geometries more representative of real pores throats (converging/diverging and non-axisymmetric 3D). In addition to the qualitative observations presented here, a goal is for future investigators to use the CFD simulations to develop up-scaled equations that can be later substituted into a pore-scale network model. The network model would then be used to model multiphase flow and then be validated against experimental data in core flood experiments that have shown reduced residual oil in the presence of viscoelastic polymer. Network models approximate a porous medium as an interconnected network of pores and pore throats. Much of the critical physics of multiphase flow in porous

media is due to the interaction among the pore throats and bodies of the network, which cannot usually be solved analytically. Hence, computational simulation of the network is required to understand the flow behavior of these systems. Quantitative techniques have been developed to model behavior in porous media ranging from single-phase Newtonian flow (Bryant et al., 1993) to multiphase (Baake and Oren, 1997) and non-Newtonian (Lopez et al., 2003; Balhoff and Thompson, 2004, 2006; Sochi, 2009) flows.

5.2.3.2 Converging-Diverging Tube and Dead-End Pores

The results show the deformed oil droplet, placed at the center of the constriction, in order to analyze how the ALE method can handle this problem numerically. The results shown here are only for demonstration of the ALE method and its numerical difficulty for the application of simulation of snap-off. When using the ALE method for interface tracking, some numerical and mesh problems are encountered. As discussed in the methodology section, the mesh in the ALE method can be distorted (figure 5.20) and it is fine until the distortion level reaches to a threshold value beyond which the simulation no longer continues. The threshold value for the mesh element can be chosen based on different applications. The criteria for bad element mesh conditions at which the simulation stops in the transient simulation in this study include interior angle, aspect ratio, bend, and skew of mesh element. The value of each parameter can be selected based on the physics of the problem. The interior angle is between 5 to 170 degrees, the aspect ratio is below 1.0, the maximum bend is 0.8, and the maximum skew is 10. The simulation will not continue until all of these criteria are met. In other words, the bad mesh elements are too bended, too stretched, and non-convex. Note that the more stringent the criteria, the more iteration are required. In some cases, a solution that respects a particular criterion may not even be found (Braes, 2000; Cruchaga, 2006; Ansys Polyflow User's Guide,

2012). The mesh needs to be recovered first before the simulation in the next time step can be carried on.

Figure 5.20 shows that the mesh around the interface between the oil droplet (blue mesh lines) and the displacing fluid (black mesh lines) is in good condition initially (t = 0 s). Then as the oil phase travels and the interface deforms the mesh network needs to be adjusted to capture the precise boundary between two phases by re-shaping the mesh element shape. This process is known as re-meshing as introduced previously. In some ideal cases, re-meshing will continue till the end of the simulation. However, due to the complex geometry in this example the re-meshing of mesh elements cannot continue at some point as shown in figure 5.20(b) because the meshes around the interface become too stretched, and the criteria for continuing re-meshing are not met anymore. As a result the simulation is crashed due to bad mesh elements. In addition, Figure 5.20 (b) and (c) compares the droplet deformation for viscoelastic and Newtonian fluids at t = 0.041 s; as expected much less deformation occurs in the viscoelastic case (figure 5.20 (c)). From these results, there are two hypotheses for which more investigation is recommended. First, if initially there is an oil ganglion in multi-pore media, the viscoelastic fluid prevents oil from being snapped off. Second, if there is an already snapped-off oil droplet the Newtonian surrounding fluid can squeeze it more to push it through the constriction.

Figure 5.21 shows the mesh before and after the meshing treatment for t = 0.041 s. The simulation crashes (figure 5.21a) because the cells are too stretched. When a bad mesh element is formed, the re-meshing technique cannot continue. Under the condition in figure 5.21(a) the simulation crashes because the criteria to continue re-meshing cannot be met. Therefore, we need to generate an entirely new mesh network for the whole existing geometry. This mesh treatment in figure 5.21 is different from the re-meshing technique. To conduct the mesh treatment, the

simulation result at t = 0.041 s is imported into a new simulation setup with a re-generated mesh and a simulation restart is carried out from 0.041 s. And again the re-meshing continues till one of the criteria for bad mesh elements are met, and then a new mesh network is generated for another simulation restart. Figure 5.21b shows the mesh after re-generation and now the mesh is in good condition to continue the simulation. This process needs to be repeated if the simulation crashes again at a later time. The geometry in figures 5.20 and 5.21 are the same as figure 5.2(c) and the fluid properties are the same as case (a) in Table 5.1.

In addition, to understand in which condition the oil droplet begins to be mobilized in dead-end pores, steady-state CFD modeling was performed for viscoelastic flow in a dead-end pore structure. The steady-state simulation is a preliminary step for dynamic (transient) modeling at that dead-end geometry. The dynamic simulation was done on the triangular dead-end geometry with wider dead-end section to make it easier to mobilize the oil droplet. Figure 5.22 shows the oil droplet before and after deformation and that the simulation stops at the point which needs more mesh refinement. The fluid is Newtonian for this case and fluid properties are the same as case (a) in Table 5.1. The geometry of the triangular section in figure 5.22 is 105 μm in depth and 300 μm in width, and the flowing channel has a radius of 50 μm. In the future, sensitivity analysis is recommended in order to understand under which conditions the oil droplet will be mobilized.

5.3 Conclusions

Dynamic simulations show strikingly different behavior between elastic and inelastic fluids; oil droplets are deformed over time when an inelastic fluid is injected but the droplet does not deform in the presence of elastic fluids. This work provides a preliminary numerical and theoretical explanation for the observed laboratory and field studies. It also suggests that

additional oil could potentially be recovered using viscoelastic polymers in secondary or tertiary recovery methods. Recommended future work should focus on additional dynamic modeling in more complex geometries for the purpose of upscaling flow equations for viscoelastic flow that could be then substituted into a pore-network model and validated against experimental data in cores.

In this study, CFD simulations were performed in geometries aiming at representing pore structure and geometry at which the residual oil can be trapped. CFD modeling was performed on both triangular and rectangular dead-end geometries. It shows that the viscoelastic effect is not significant under the condition chosen for our micro-scale experimental study, and that it needs to be modified to increase the elasticity of polymer either by using other polymers with a higher relaxation time or increasing the flow rate. Tensional force increase when increasing the elasticity of polymer; then pulling effect will occur to mobilize the trapped oil droplet in the dead-end part.

The microfluidic experiments were conducted in various geometries. This work provides a numerical and theoretical explanation for the acquired laboratory data. Results also suggest that, provided the relaxation time of the polymer could be sufficiently increased to make the pulling-effect significantly high, additional oil could potentially be recovered using viscoelastic polymers in secondary or tertiary recovery methods. Pre-emption of deformation and eventual snapping of the oil droplet with viscoelastic polymers could also help recover some of the residual oil reduction reported in the literature. The simulation results in the dead-end geometry indicate that the pulling effect is not likely mechanism acting at the pore-level to reduce residual oil saturation, at least with current polymer properties at actual reservoir conditions.

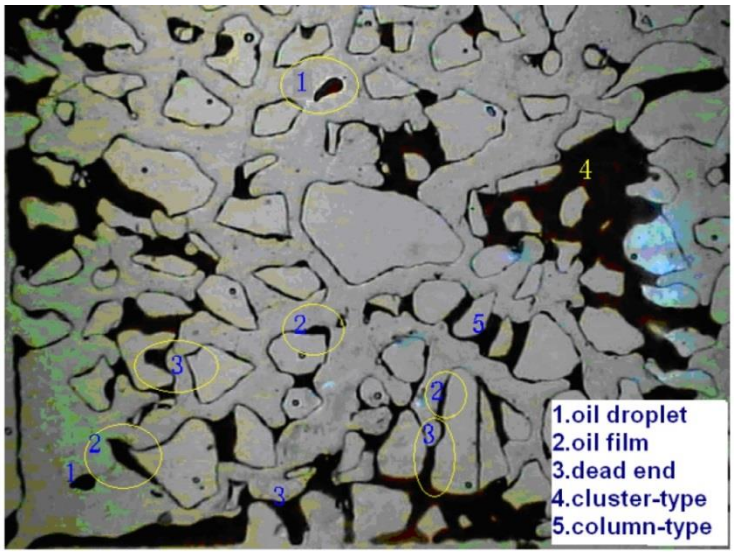

Figure 5.1 Types of residual oil distribution; oil droplet, oil film, dead end, cluster-type, and column-type (Wang, 2000)

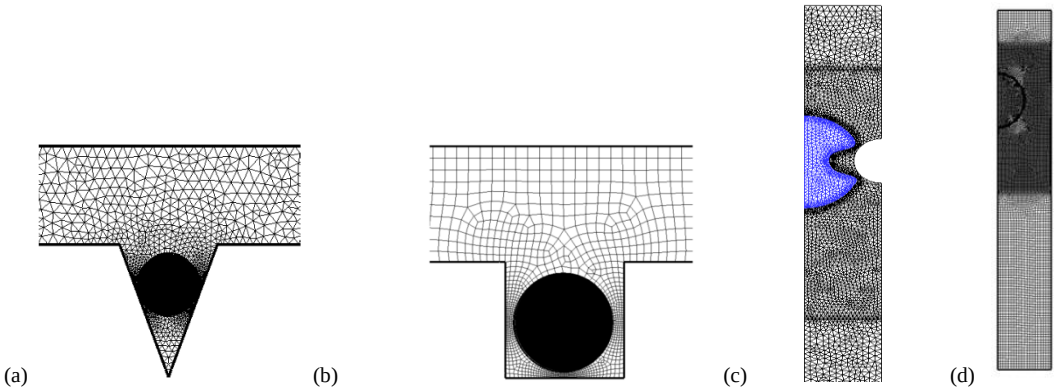

Figure 5.2 Mesh configurations for shallow dead-end geometry (a) triangular, (b) square, (c) converging-diverging geometry, and (d) dynamic simulation in a capillary tube

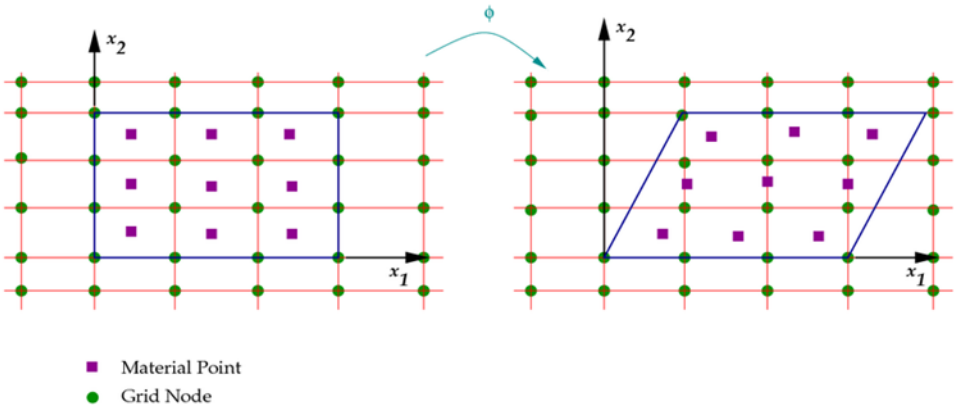

Figure 5.3 Eulerian flow fields and mesh techniques

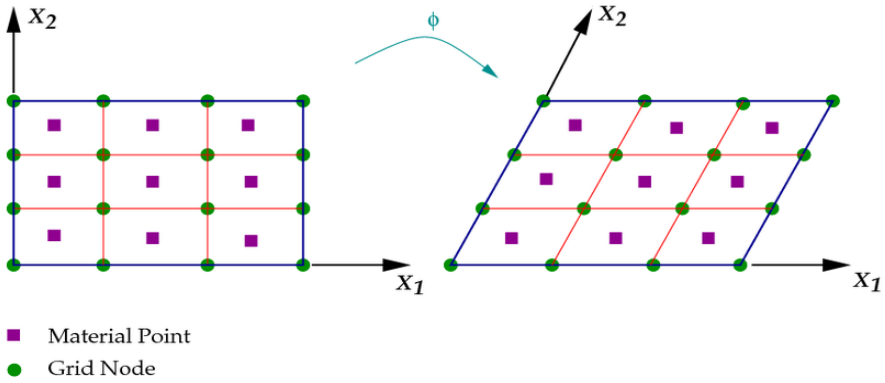

Figure 5.4 Lagrangian flow fields and mesh techniques

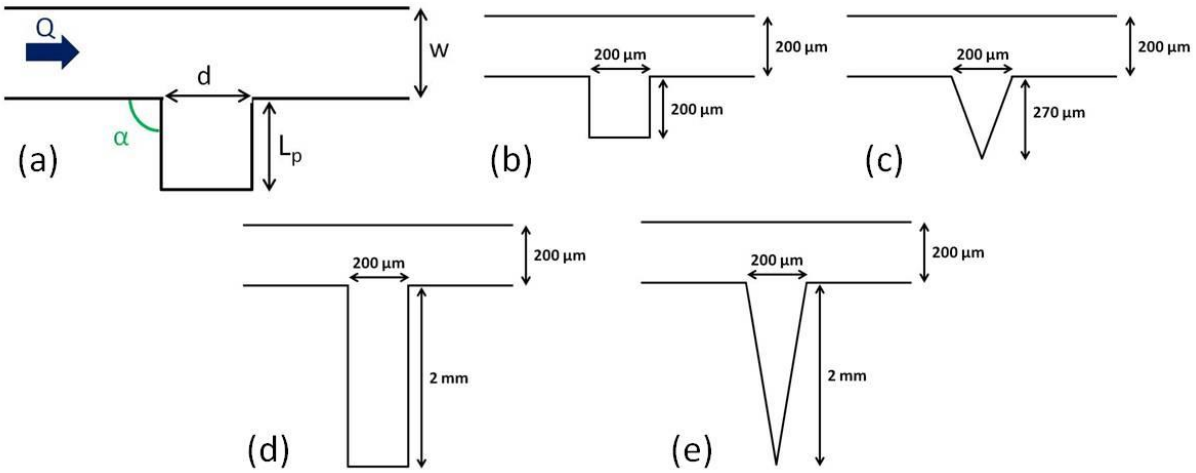

Figure 5.5 Sketches of the experimental microsystems (a) A main channel is laterally connected to a dead end of pore; varying the length L_P of the pore and the angle α, we get different shapes: (b) square, (c) short triangle, (d) deep rectangle, (e) deep triangle (Duboin, A., 2013)

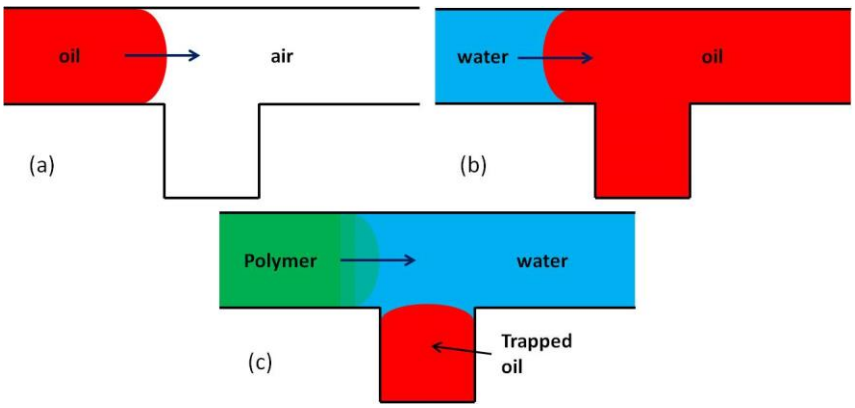

Figure 5.6 Description of the experimental sequence (here for a partially water wet system). The system is connected through tubing to a syringe pump allowing injecting the fluids at a constant flow rate (a) we first fill the system with oil, (b) then, a secondary water flood is used to trap oil in the pore, (c) and finally a tertiary flood of polymer is performed to study oil recovery (Duboin, A., 2013)

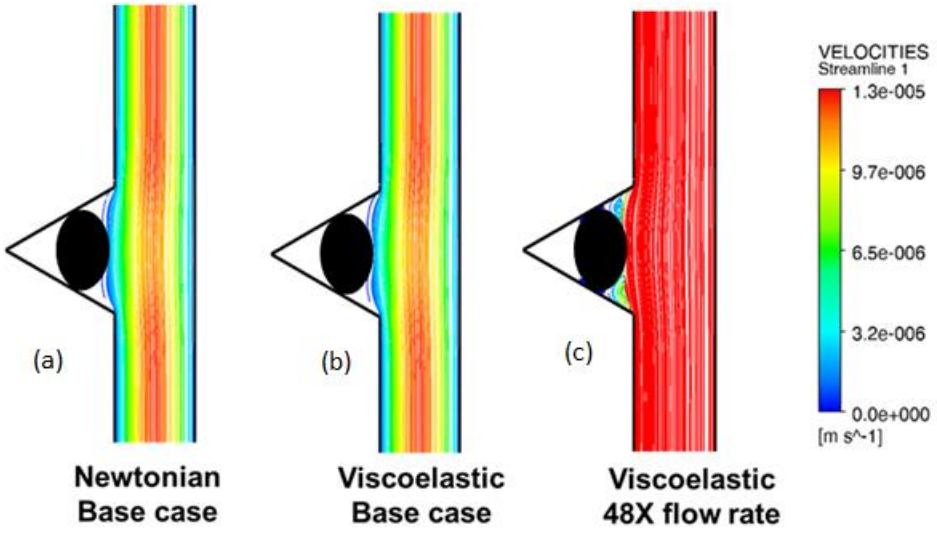

Figure 5.7 Velocity streamlines for (a) Newtonian base case, (b) viscoelastic base case, and (c) viscoelastic with 48 time higher flow rate than viscoelastic base case

Table 5.1 Summary of fluid properties

	$\mu_{displacing}$ (mPa.s)	$\mu_{displaced}$ (mPa.s)	λ (sec)	Flow rate (µL/min)	Re	Wi
Case (a)	23	24	0	100	0.53	0
Case (b)	23	24	0.35	100	0.53	486
Case (c)	23	24	0.35	4800	25.44	23328

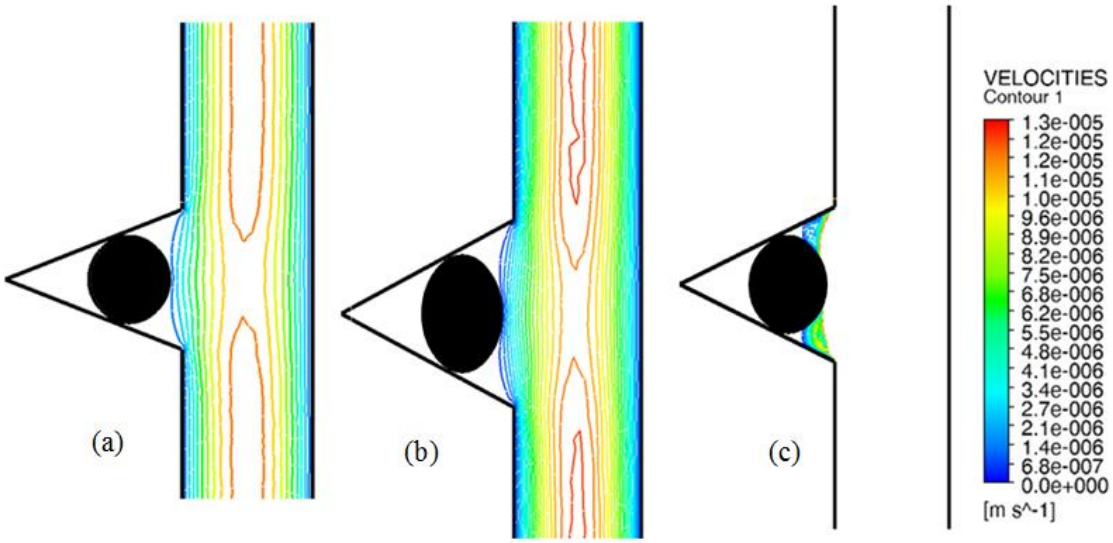

Figure 5.8 Velocity contours for (a) Newtonian base case, (b) viscoelastic base case, and (c) viscoelastic with 48 time higher flow rate than viscoelastic base case

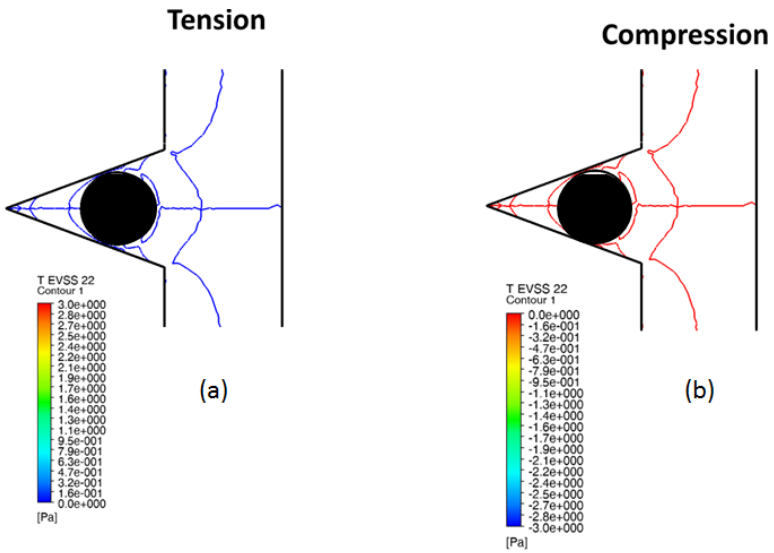

Figure 5.9Normal stress contours for Newtonian base case (case a) (a) positive normal stress (tension), and (b) negative normal stress (compression)

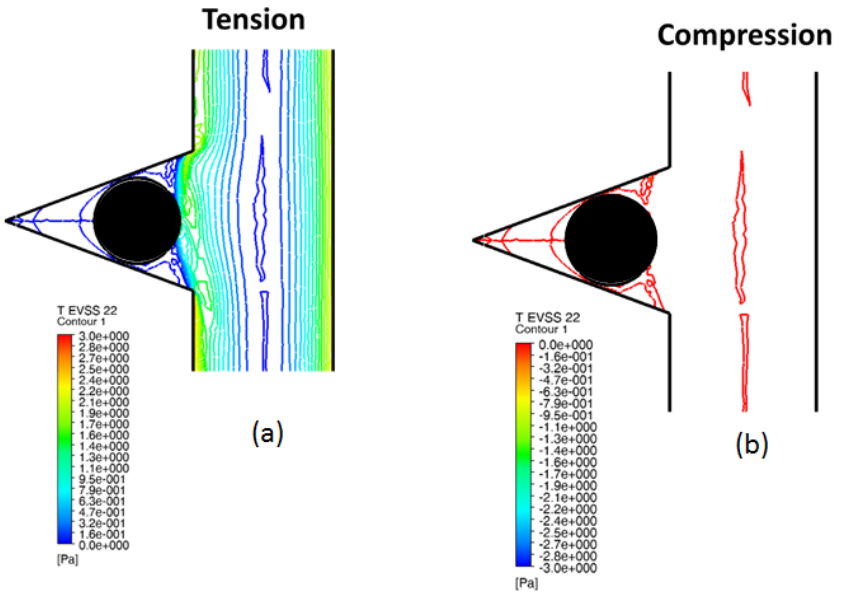

Figure 5.10 Normal stress contours for viscoelastic with 48 time flow rate compared with base case (case c) (a) positive normal stress (tension), and (b) negative normal stress (compression)

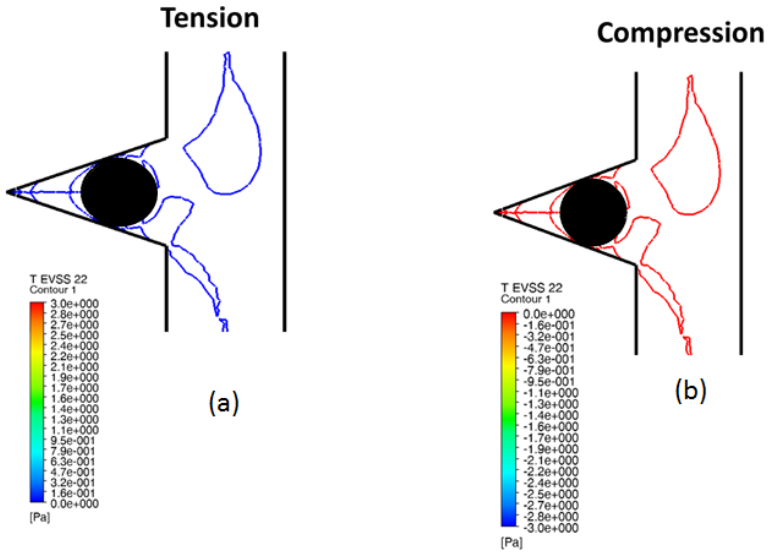

Figure 5.11 Normal stress contours for viscoelastic base case (case b) (a) positive normal stress (tension), and (b) negative normal stress (compression)

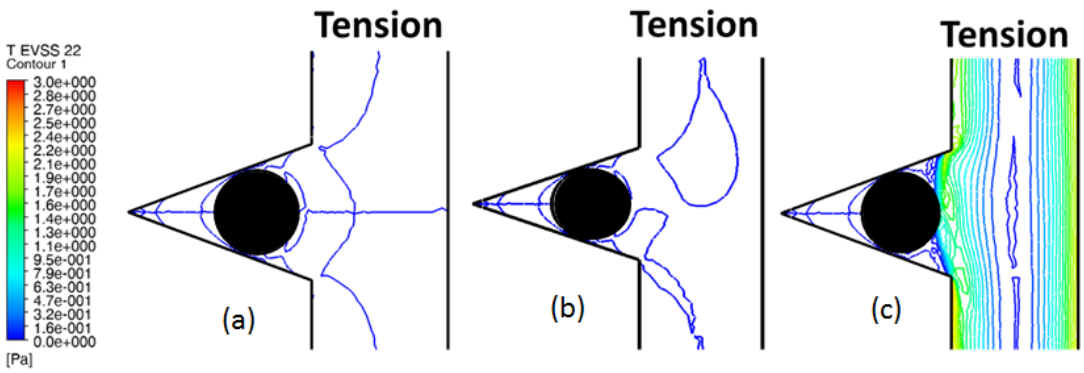

Figure 5.12 Tension component of normal stress contours for (a) case a, (b) case b, and (c) case c

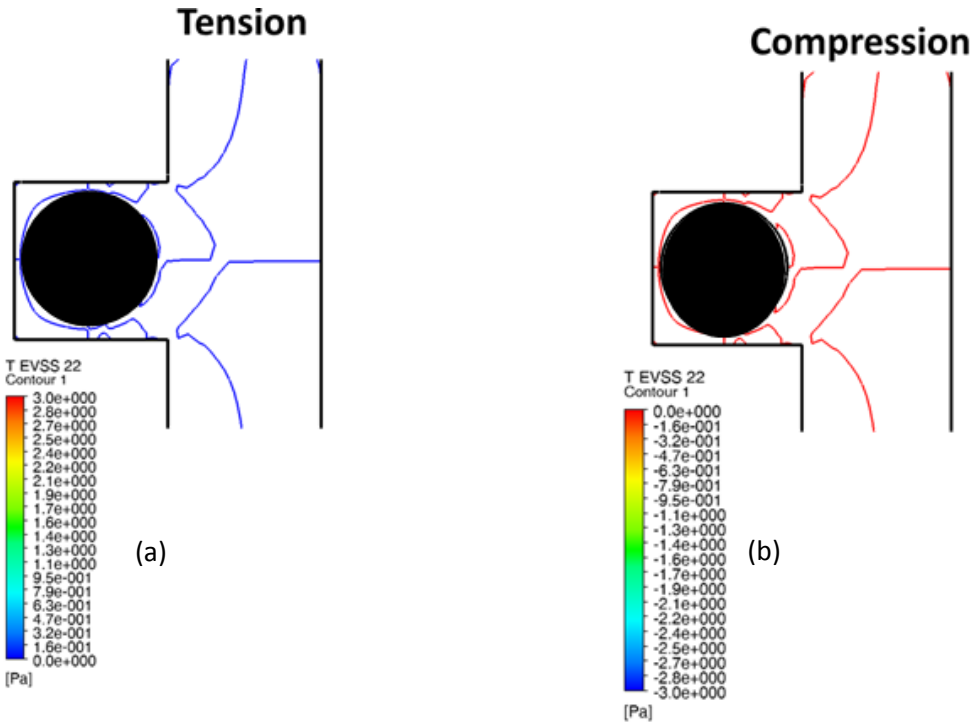

Figure 5.13 Normal stress contours for Newtonian base case (case a) (a) positive normal stress (tension), and (b) negative normal stress (compression)

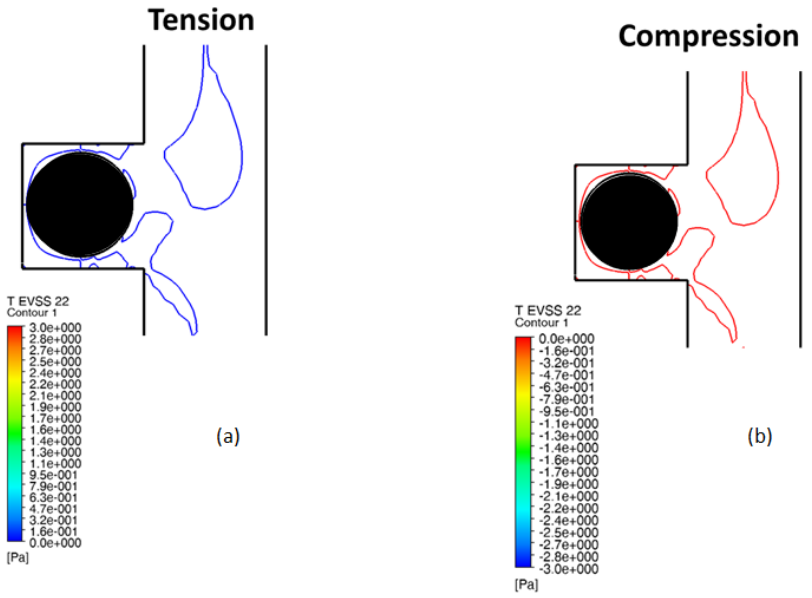

Figure 5.14 Normal stress contours for viscoelastic with 48 time flow rate compared with base case (case b) (a) positive normal stress (tension), and (b) negative normal stress (compression)

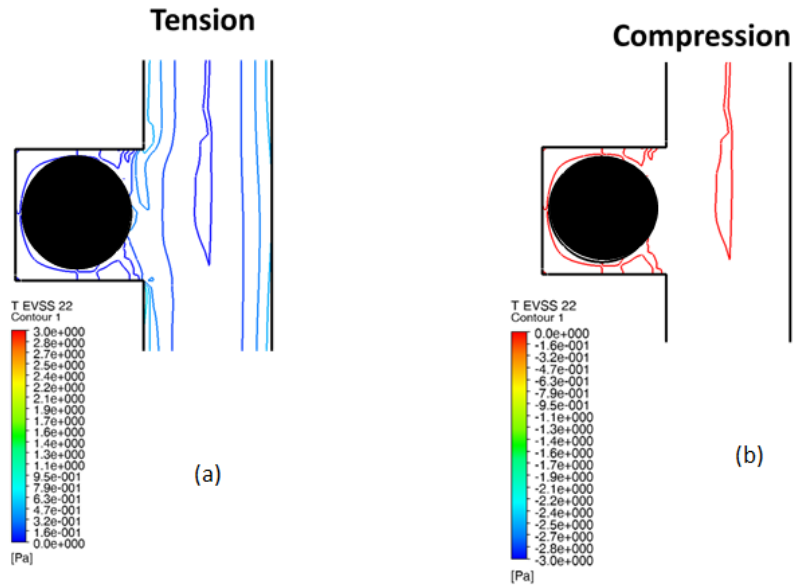

Figure 5.15 Normal stress contours for viscoelastic with 48 time flow rate compared with base case (case c) (a) positive normal stress (tension), and (b) negative normal stress (compression)

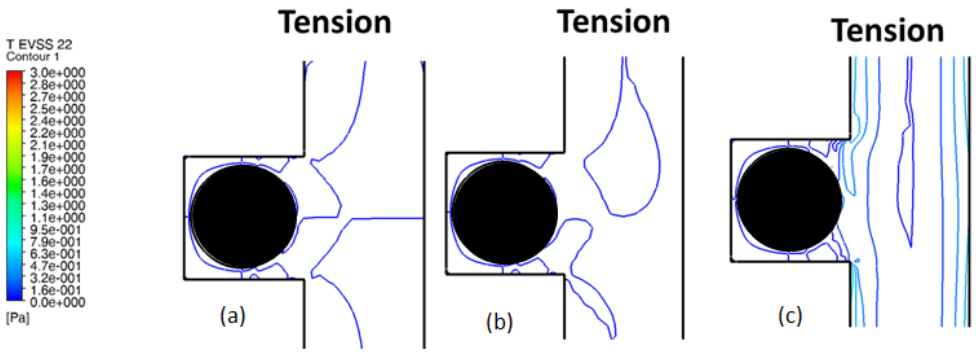

Figure 5.16 Tension component of normal stress contours for (a) case a, (b) case b, and (c) case c

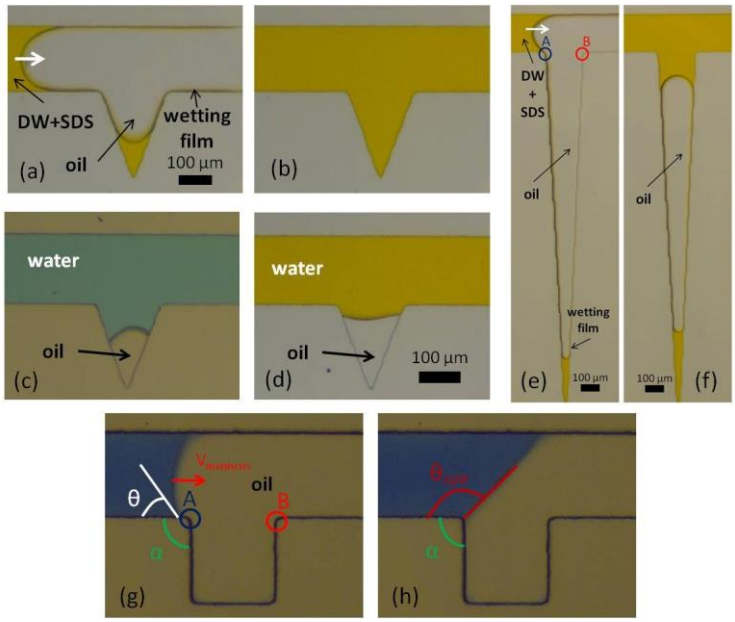

Figure 5.17 Experimental results of trapping assays. Depending on the wetting conditions and the shape of the pore, we observe three kinds of trapping results. In full water-wet systems there is no trapping in short geometries (a-b) and trapping in deep ones (e-f). In partially water-wet systems we get partial trapping (c), whereas in partially oil-wet systems we obtain trapping (d). The way the water/oil/PDMS contact line enters in the pore depends on the wetting contact angle θ, the angle α and the injection flow rate Q. (Duboin, A., 2013)

Table 5.2 Summary of oil trapping assays (Experiment) (Duboin, A., 2013)

Injection solution	Wetting property	Pore shape	Trapping result
DW + SDS	fully water-wet	square	no trapping
DW + SDS	fully water-wet	short triangle	no trapping
DW + SDS	fully water-wet	deep triangle	trapping
DW + SDS	fully water-wet	deep rectangle	trapping
DW	partially water-wet	square	partial trapping
DW	partially water-wet	short triangle	partial trapping
DW	partially oil-wet	square	trapping
DW	partially oil-wet	short triangle	trapping

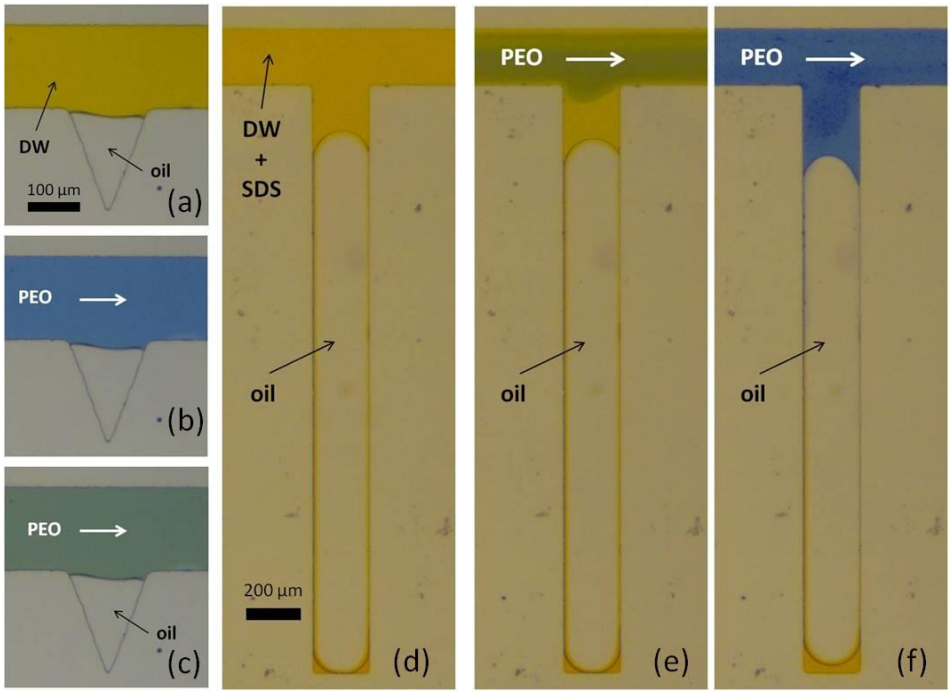

Figure 5.18 Experimental results of detrapping assays with a tertiary flood of 4, 000 ppm PEO aqueous solution injected at a constant flow rate Q = 100 µL.min^{-1}. We observe oil detrapping neither in partially oil-wet pore (a-c) nor in fully water-wet deep pore (d-f). (Duboin, A., 2013)

Table 5.3 Characterization of oil detrapping assays. (Duboin, A., 2013)

Tertiary flood	Wetting property	Pore shape	C_m (ppm)	Q (µL/min)	h (µm)	Ca	We	De-trapping result
PEO	partially oil-wet	short triangle	4, 000	0.2	60	10^{-4}	0.5	no detrapping
PEO	partially oil-wet	short triangle	8, 000	0.2	60	2.10^{-3}	1.4	no detrapping
PEO	fully water-wet	deep triangle	4, 000	100	60	8.10^{-2}	243	no detrapping
PEO	fully water-wet	deep rectangle	4, 000	100	60	8.10^{-2}	243	no detrapping
PEO	fully water-wet	deep rectangle	8, 000	10	60	10^{-1}	70	no detrapping

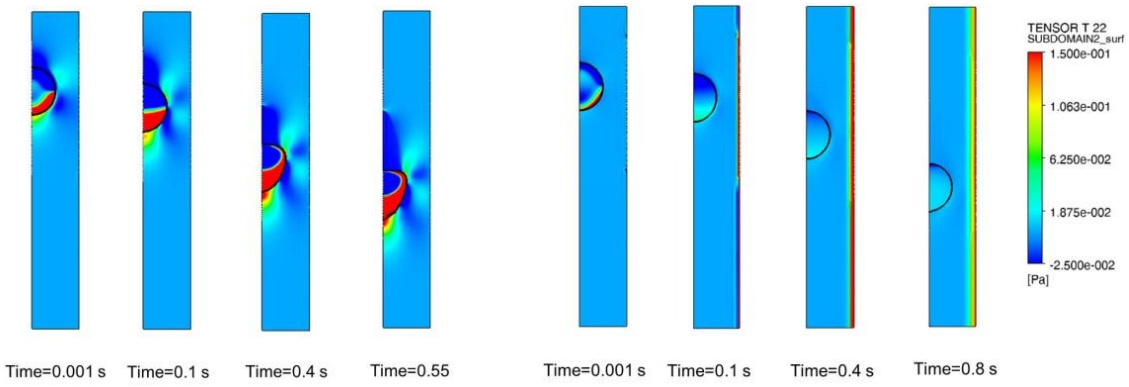

(a) (b)

Figure 5.19 Dynamic simulations of wetting fluid flowing around a spherical oil droplet at various snapshots in time. The simulations are for an injecting fluid of (a) inelastic water and (b) elastic polymer

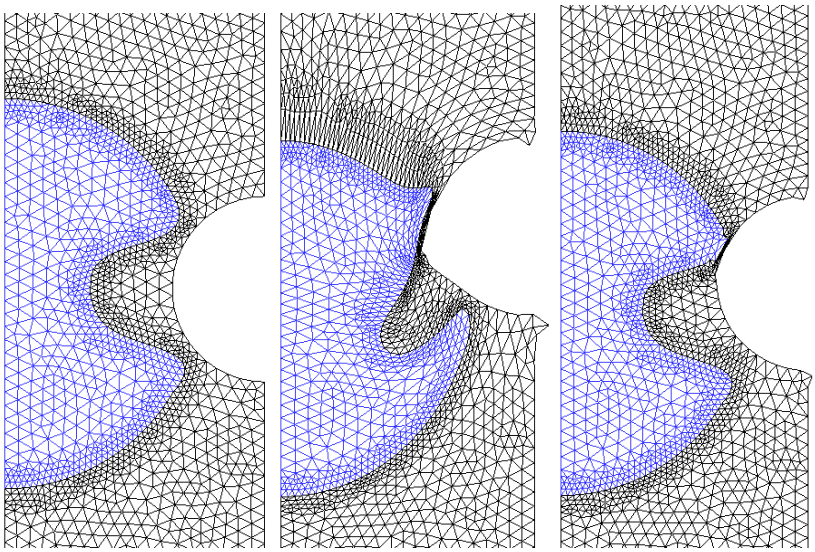

Figure 5.20 The mesh configuration for (a) initial time for both Newtonian and viscoelastic (t = 0), (b) Newtonian at t = 0.041 s, and (b) viscoelastic at t = 0.041 s

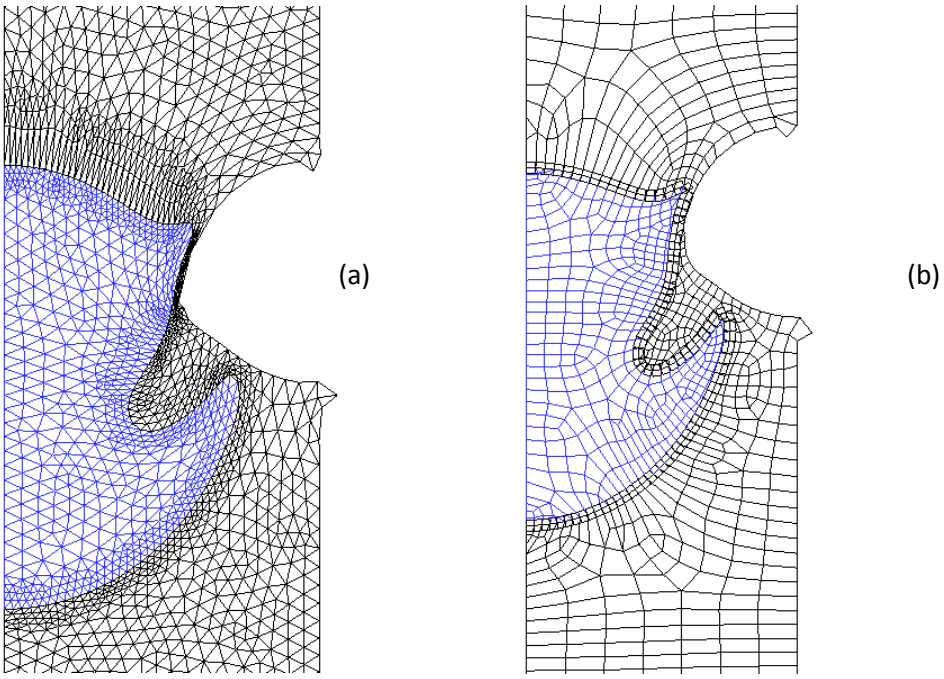

Figure 5.21 The mesh configuration for t = 0.041 (a) before mesh treatment, and (b) after mesh treatment

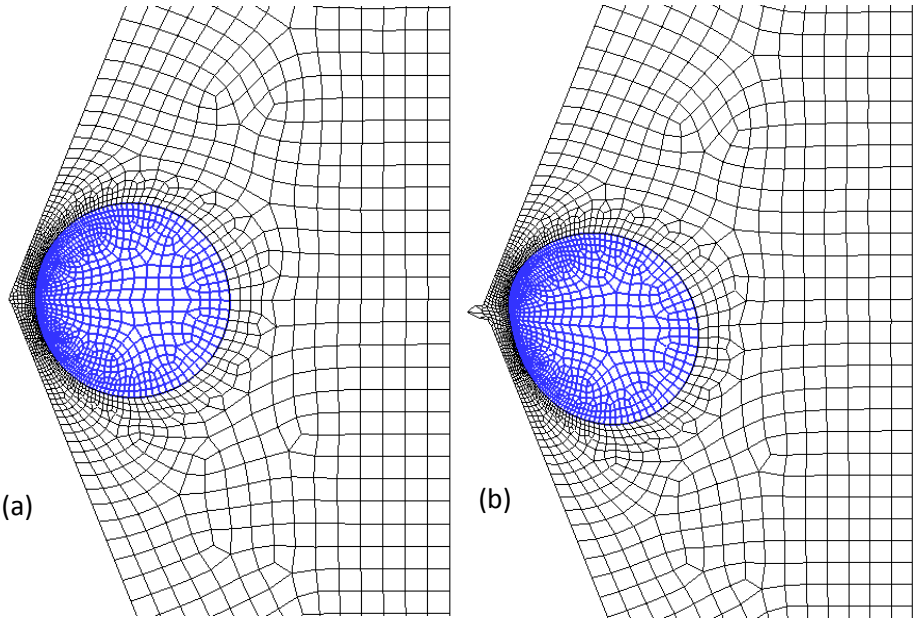

Figure 5.22 The mesh configuration for dead-end geometry at (a) initial time (t = 0), (b) t = 0.09 s

Chapter 6: Conclusions and Future Work

6.1 Conclusions

This study investigates the effect of polymer elasticity in reduction of the residual oil recovery and pore-network simulation of single-phase viscoelastic fluid flow through porous media has been developed. Several conclusions of this work are listed below.

1. CFD modeling has been performed for much converging-diverging geometry of various dimensions and a closed-form equation for viscoelastic fluid through these ducts has been developed. The fitted closed-form equation (3.9) from CFD simulation is similar to Wissler's (1971) equation which he solved analytically using some simplifications and assumptions. The new equation shows shear thickening behavior which has been observed experimentally by many authors. It also includes terms for shear-thinning behavior at low De.
2. The Upper-Convected Maxwell model was used to describe the fluid rheology for simplicity. The CFD simulation results showed shear-thinning behavior at moderate shear rate, consistent with other numerical studies in the literature. This shear-thinning behavior (in the absence of a shear-thinning rheological model) is not fully-understood, but may be due to entrance pressure effects which are not fully developed in the converging-diverging geometry.
3. A single phase pore-network model was developed for viscoelastic flow. The closed-form equation obtained from CFD simulation has been implemented into the pore-network model. The developed pore network simulations capture many viscoelastic effects observed in core-flood experiments such as a shear-thickening regime at high apparent shear rate.
4. The developed pore-network modeling for single-phase viscoelastic polymer has been validated against some experimental results. The computer-generated sphere packing pore-

network has been compare with bead-pack cores and they are largely in good agreement. However for some experiments, the model does not match the data at high apparent shear rates, which could be due to shear-degradation at these high shear rates.

5. CFD modeling has been performed in multiphase systems in such a way that the oil-phase is stationary and not deforming or moving (referred to herein as static simulations). The oil droplet behaves as a solid object and fluids (water or viscoelastic) flow around the droplet. Fluid dynamics are investigated in the geometry and more specifically the forces acting on the oil droplet. Simulations show that as the fluid becomes more and more elastic the fluid dynamics properties become more asymmetric. The CFD simulations show this asymmetric behavior leads to form additional forces due to normal stress on the objects which is negligible for Newtonian fluid. As the relaxation time (and therefore *De*) increase, the fluid elasticity increases and the calculated forces due to normal stress are larger. However because of numerical difficulty, a higher Deborah number could not be obtained, but the trend shows the normal stress force increases monotonically and could be large enough at high *De* to eventually push the trapped oil droplet out of the constriction in a pore structure.
6. For Newtonian flow around the oil droplet, the pressure profile is symmetric and no eddies are observed in front or behind the oil droplet. However, for viscoelastic flow, and specifically for higher Deborah numbers, as the fluid becomes more elastic the pressure profile becomes more asymmetric and eddies form ahead of the oil droplet. As a result of the eddy, a low pressure pocket forms in front of the oil droplet which leads to higher local pressure gradient to mobilize the oil droplet. Finally, by adding viscoelastic polymer into aqueous phase, the viscosity increases, the additional force due to normal stress, and higher

local pressure gradient due to low-pressure packet in front of the oil phase may help to mobilize the trapped oil phase and reduce the residual oil saturation in polymer flooding.

7. Since many reservoir rocks are mixed-wet and oil-wet, CFD modeling for mixed-wet media has been conducted to analyze the viscoelastic fluid behavior. The geometry utilized for static simulations was half of a sphere (oil droplet) adhered to the wall, and the CFD simulation results were compared with Newtonian results. It showed as the fluid becomes more elastic, the normal stresses became more pronounced, similar to the observed behavior for water-wet media.
8. CFD simulations were performed for cases in which oil droplet distance from the constriction is closer and then compared the results with Newtonian fluid. The same behavior has been observed which the normal stress increases as the fluid becomes more elastic by increasing the Deborah number. It shows as the oil droplet pushes toward the throat constriction due to the more converging-diverging geometry formed around the oil droplet, the viscoelastic fluid experiences more elasticity which leads to higher normal stresses. Then eventually the forces can overcome the entry capillary pressure and the oil droplet will be squeezed and pass through the constriction.
9. In transient CFD simulations, an oil phase along with an aqueous phase moved and the interface between phases deformed. Simulations were performed for an oil droplet moving at the center of capillary tube as a preliminary simulation results and the simulations for Newtonian and viscoelastic fluid were interesting. The dynamic results in straight capillary results show the viscoelastic fluid deforms the oil droplet less compared to a Newtonian displacing fluid. These models might explain the experimental observations that suggest viscoelastic polymer increases the resistance for oil phase to snap-off. The experiments show

more residual oil saturation reduction in secondary polymer flooding compared to tertiary polymer flooding. The hypothesis is that during secondary polymer flooding, the elasticity of polymer prevents snap-off from occurring so the oil-phase remains connected which is easier to recovery rather than snapped-off and disconnected oil phase in tertiary polymer flooding. This preliminary results needs to be extended to more complicated geometry like converging-diverging geometry and investigate if the viscoelastic fluid can or cannot prevent snap-off in actual core-flood experiments.

10. CFD modeling was performed for geometries that included trapped oil in dead-end pores and compared to existing experimental data in microfluidic channels. The modeling results were consistent with the experiments, in that no pulling effect was observed. However, hypothetically, if the polymer has around 1-2 order of magnitude higher relaxation time compare to the typical relaxation time (0.35 s), a pulling effect is observed. The conclusion is that the pulling effect is not the dominant mechanism to recover the trapped oil phase and reduce the residual oil saturation.
11. Viscoelastic polymer has several effects which could help to reduce residual oil saturation and increase the recovery as discussed above. However the combination of those effects could help to reduce the residual oil saturation and more analysis needs to be performing to analyze the importance of each effect as descried more in recommendation section.

6.2 Recommendations for Future Work

1. The single-phase pore-network model developed in this study was validated against old existing experimental data in bead packs using polymers no longer implemented in the field. For future work, new core flood experiments should be performed for various types of new polymer solutions (such as HPAM). A full rheological study on the fluids should be

performed and fit to VE rheological models. Additionally, experiments in other cores, such as Berea or Boise sandstones, are recommended to validate the single-phase pore-network model and use for field predictions. This will help determine whether the pore-scale equations implemented are applicable for imaged-based network model obtained from X-ray Microtomography (XMT) of actual cores and not the computer-generated sphere-packed pore-network. Several other complexities in actual core such as different pore-throat shape can be analyzed and check if the developed pore-network model can get a good-agreement with experimental results.

2. The pore-network used in this study was from computer sphere packing which approximates a beadpack in terms of pore structure. However for more heterogeneous cores which has more complicated pore structure such as Bentheimer, Berea, and Boise sandstone, the visualization of pore structures need to be performed. Before conducting the coreflood experiments, the core needs to be imaged to capture the pore structure for the core. After making the digitalized core, the pore-network simulations can be performed and then compared the results with polymer flood experiments.
3. The pore-network model should be extended to include multiphase flow. Although network models exist for Newtonian, multiphase flow, this problem is more challenging since the interaction between phases are unknown are for viscoelastic fluids. Therefore, first additional two-phase dynamic CFD simulations need to be performed and used to obtain local capillary pressure and relative permeability curves for viscoelastic phase as a displacing fluid.
4. The closed-form equation for viscoelastic flow was developed for a single converging-diverging duct and periodic fixed pressure boundary condition. In future work, CFD results for fixed flow rate boundary condition should be done to verify the CFD simulation results

and obtain a more universal equation since for various applications; different boundary condition will be required. Performing CFD modeling for consecutive converging-diverging ducts will allow for verification of the periodic boundary condition for both pressure and flow rate boundary conditions.

5. CFD simulations should be conducted in more complex geometries; for example, a series of constricting throats in a row or a pore connected to several throats because it can investigate the memory-effect of viscoelastic polymer. They can be used to improve the closed-form equation for flow in a throat.
6. The strong nonlinearities in the viscoelastic problems prevent modeling at large *De*. Here, a UCM model and a DEVSS SU numerical method were primarily used in Polyflow. It is recommended to investigate other rheological models outside the Oldroyd- B family such as PTT model. The PTT model is one of the most realistic viscoelastic models which can model the shear-thinning behavior of polymer. For PTT model the total stress tensor is calculated from equation 2.22 at which $\boldsymbol{T_2}$ component is calculated by equation 2.23 like Oldroyd-B model, but $\boldsymbol{T_1}$ is calculated from equation 6.1.

$$exp\left(\frac{\varepsilon\lambda}{\eta}\boldsymbol{tr}(\boldsymbol{T_1})\right)\boldsymbol{T_1} + \lambda\left[\left(1-\frac{\xi}{2}\right)\boldsymbol{T_1}^{upper} + \frac{\xi}{2}\boldsymbol{T_1}^{lower}\right] = 2\eta\boldsymbol{D} \qquad (6.1)$$

Where T_1^{uppr} and T_1^{lower} is upper-convected time derivative and lower-convected time derivative, ε is a material parameter which controls the elongational behavior, ξ is another material parameter which controls shear viscosity behavior. Using PTT model has been recommended for more realistic polymer behavior. The rheological measurement can be conducted for viscoelastic polymer at different concentrations. Afterwards, the curve-fitting can be performed on the experimental data and model parameter for PTT model (e.g., *ε, and* ξ for equation 6.1) can be calculated using Ansys Polymat software.

7. More investigation into the applicability of DEVSS SU is recommended. The results presented using this numerical approach is consistent with our fundamental understanding of viscoelastic flow and with experimental observations. The method has been used by other authors (Guenette and Fortin, 1995). However, other comparable methods such as Streamline Up-winding Petrov-Galerkin (SUPG), Discontinuous Galerkin methods give very different results and some authors question the applicability of DEVSS SU (Brooks, 1982; Marchal and Crochet, 1987; Luo, 1989; Rajagopalan, 1990, Kumar, 2014).
8. Dynamic simulation for multi-phase flow needs to be performed to better understand pore-level behavior. These results need to be up-scaled for input to a network model. Polyflow Ansys finite element software was used in this study but is better geared to single-phase flow; it has limited multi-phase applications. Polyflow does not include surface tension/capillary pressure and also encounters problems with mesh configuration; it was not able to simulate snap-off at the constriction. Ansys Polyflow software can be used to solve the momentum equations; however it does not have the extra equation for the interface (which is defined in a source term). This term is more active and is come to the point at the vicinity of the interface. Other multi-phase software such as Ansys Fluent and GOMA has this ability. In this work, a method was not found to account for the dispersion term either using Polyflow; instead the momentum equation itself was solved, and then velocity, stress, and forces due to viscous and inertia forces were solved. Other finite element software packages, such as GOMA developed by Sandia National Lab, should be used to conduct more dynamic simulations and observe the effect of polymer elasticity on snap-off mechanism.

9. The micro-fluidic experiments conducted by Total in dead-end pores were good evidence of how important the pulling-effect is on reducing the residual oil recovery; however it is recommended to conduct more experiments for different polymers such as HPAM because the PEO polymer used is very sensitive to shear-degradation. One possible explanation the pulling-effect was not observed, is that the polymer degraded, decreasing the elasticity of polymer. Similar microfluidic experiment need to be performed for other hypotheses for S_{or} reduction, including additional force due to polymer elasticity to mobilize disconnected oil droplet and effect of polymer elasticity on snap-off mechanism. For instance, to analyze the additional force due to polymer elasticity, the single pore-throat can be made for a microfluidic system and test when the viscoelastic polymer injected whether it can overcome the capillary pressure and mobilize oil droplet through the constriction.
10. It is recommended to conduct more core-flood experiments to better understand the effect of polymer elasticity on S_{or}. Polymer core floods for purely viscous and also viscoelastic polymer with similar viscosity should be performed and then analyzed to determine whether the capillary desaturation curve is different. Furthermore it is recommended to conduct CT-scans on core-floods to isolate macroscopic effects such as heterogeneity. This helps to better understanding how the polymer elasticity helps to either improve sweep efficiency and pore-scale displacement.

Appendices

Appendix A: Geometry Parameters for the Sinusoidal Functions

Geometry parameters for the sinusoidal functions (Λ and α and dimensionless quantities. All other parameters are in SI unit)

Table A1 Geometry parameters for $\Lambda = 0.79$

$\Lambda = 2\pi h/l$	Case	$\alpha = \varepsilon/h$	$r_{\max}$	$r_{\min}$	ϵ	h	l	L^*
0.79	1	0.1	5.5E-05	4.5E-05	5E-06	5E-05	4.0E-04	2.0E-03
	2	0.3	6.5E-05	3.5E-05	1.5E-05	5E-05	4.0E-04	2.0E-03
	3	0.5	7.5E-05	2.5E-05	2.5E-05	5E-05	4.0E-04	2.0E-03
	4	0.7	8.5E-05	1.5E-05	3.5E-05	5E-05	4.0E-04	2.0E-03

Table A2 Geometry parameters for $\Lambda = 1.57$

$\Lambda = 2\pi h/l$	Case	$\alpha = \varepsilon/h$	$r_{\max}$	$r_{\min}$	ϵ	h	l	L^*
1.57	5	0.1	5.5E-05	4.5E-05	5E-06	5E-05	2.0E-04	2.0E-03
	6	0.3	6.5E-05	3.5E-05	1.5E-05	5E-05	2.0E-04	2.0E-03
	7	0.5	7.5E-05	2.5E-05	2.5E-05	5E-05	2.00-04	2.0E-03
	8	0.7	8.5E-05	1.5E-05	3.5E-05	5E-05	2.0E-04	2.0E-03
	9	0.9	9.5E-05	5.5E-05	3.5E-05	5E-05	2.0E-04	2.0E-03

Table A3 Geometry parameters for $\Lambda = 3.14$

$\Lambda = 2\pi h/l$	Case	$\alpha = \varepsilon/h$	$r_{\max}$	$r_{\min}$	ϵ	h	l	L^*
3.14	10	0.1	5.5E-05	4.5E-05	5E-06	5E-05	1.00E-04	2.00E-03
	11	0.3	6.5E-05	3.5E-05	1.5E-05	5E-05	1.00E-04	2.00E-03
	12	0.7	8.5E-05	1.5E-05	3.5E-05	5E-05	1.00E-04	2.00E-03
	13	0.9	9.5E-05	5.5E-05	3.5E-05	5E-05	1.00E-04	2.00E-03

* The duct was extended to make sure that the flow is fully developed. *L* is the entire length of the duct subtracted by *l*.

Appendix B: Pressure, Velocity Field and Streamline for Selected CFD Simulations

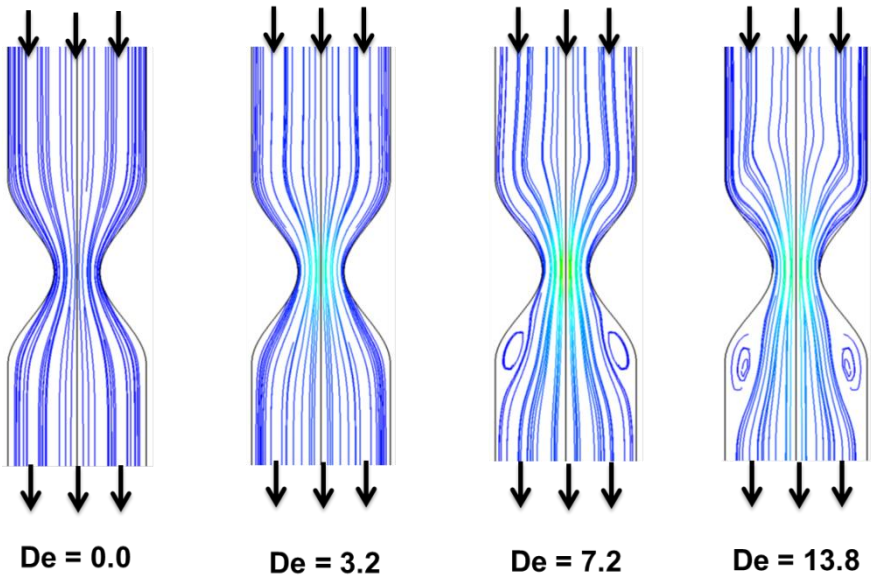

Figure B1 Streamline of flow through sinusoidal channel from CFD simulation at selected Deborah number De=0.0, 3.2, 7.2, and 13.8. The dimensionless parameters for the channel is α=0.5 and Λ=1.57. Only the middle portion of the channel is shown

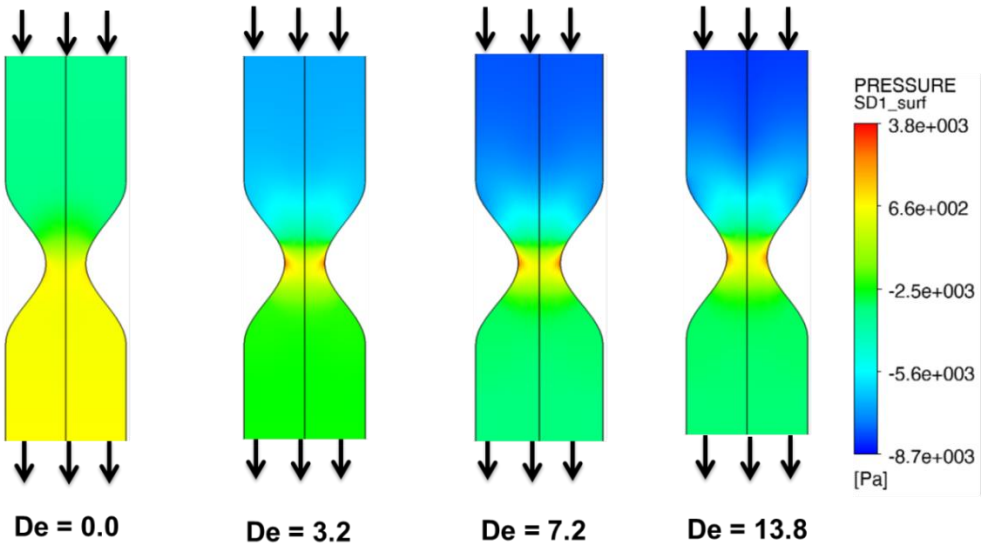

Figure B2 Pressure distribution of flow through sinusoidal channel from CFD simulation at selected Deborah number De=0.0, 3.2, 7.2, and 13.8. The dimensionless parameters for the channel is α=0.5 and Λ=1.57. Only the middle portion of the channel is shown

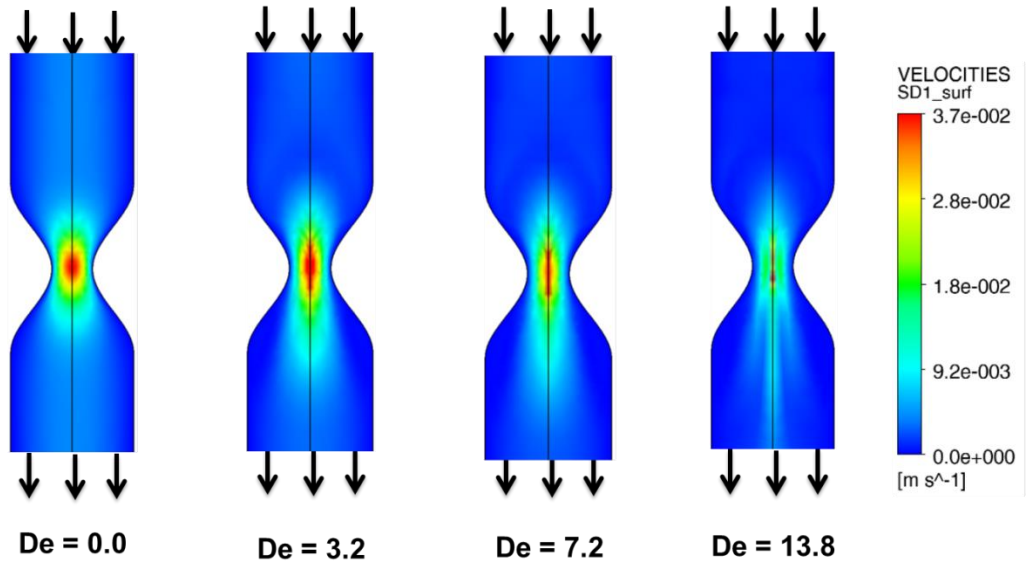

Figure B3 Velocity field of flow through sinusoidal channel from CFD simulation at selected Deborah numbers De=0.0, 3.2, 7.2, and 13.8. The dimensionless parameters for the channel is α=0.5 and Λ=1.57. Only the middle portion of the channel is shown

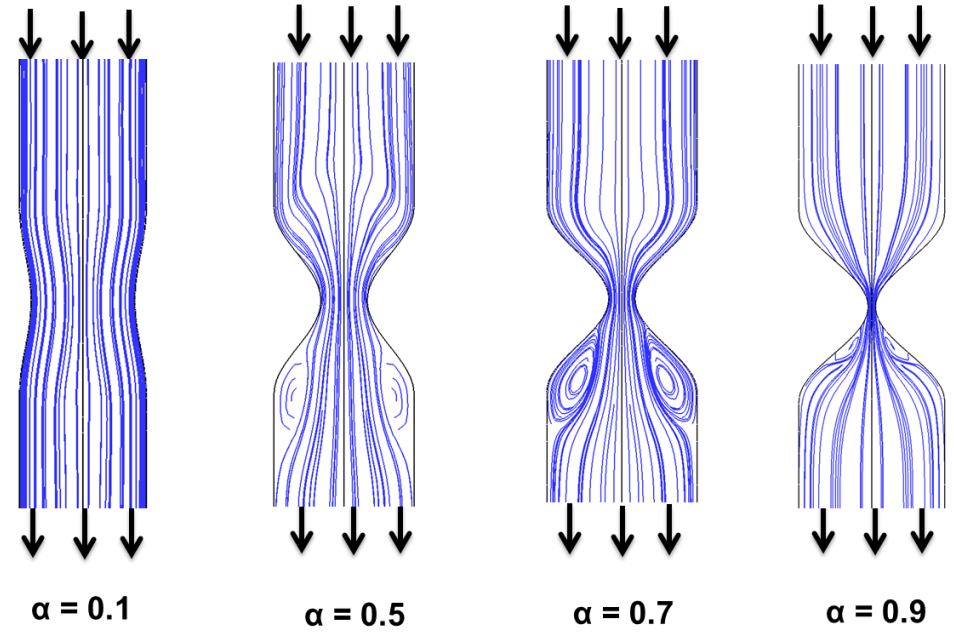

Figure B4 Streamline of flow through sinusoidal channel from CFD simulation at De=10 with dimensionless parameters Λ=1.57 and *a* = 0.1, 0.5, 0.7, and 0.9. Only the middle portion of the channel is shown

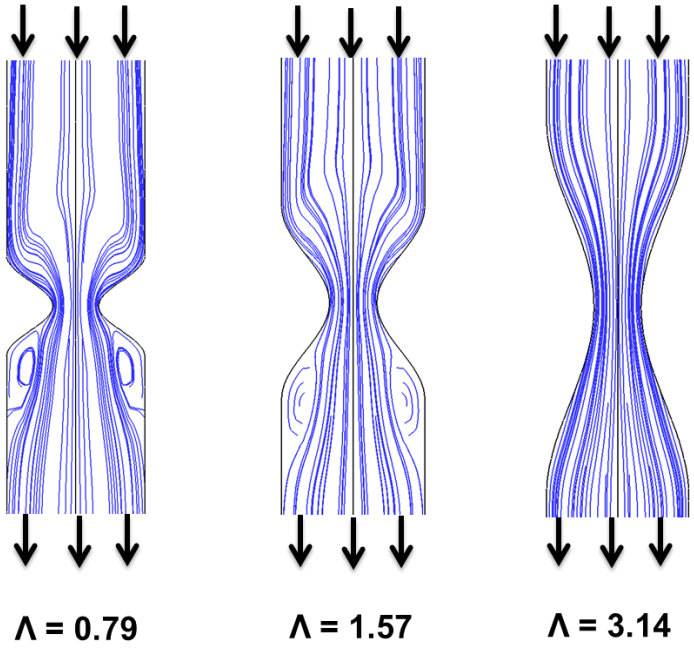

Figure B5 Streamline of flow through sinusoidal channel from CFD simulation at De=10 with dimensionless parameters a = 0.5 and Λ=0.79, 1.57, and 3.14. Only the middle portion of the channel is shown

Appendix C: Derivation of the Fitted Flow Resistance Equation from CFD Modeling

To obtain equation 3.9, we fitted the μ_{app}/μ_{shear} vs. *De* data for the channels and find *a* and *b* for each geometry aspect ratio. The next step is to correlate *a* and *b* with the geometry parameters α and Λ. It turns out that *a* only depends on α, while *b* depends on both α and Λ. Figure C1(a) gives plots of a vs. α and figure C1(b) shows *b* vs. α and Λ. The correlation for $a = a(\alpha)$ and $b = b(\alpha, \Lambda)$ were found as

$$a = a(\alpha) = 0.42\alpha \tag{C.1}$$

$$b = b(\alpha, \Lambda) = b_1 \Lambda^{b_2} \alpha^{b_3} \tag{C.2}$$

where $b_1 = 1.78 \times 10^{-4}$, $b_2 = 2.384$ and $b_3 = -0.655$. Figure C2 shows a plot of equation 3.9 against CFD simulation for channel geometry of α =0.5 and Λ =1.57. The good agreement indicates that equation 3.9 is valid.

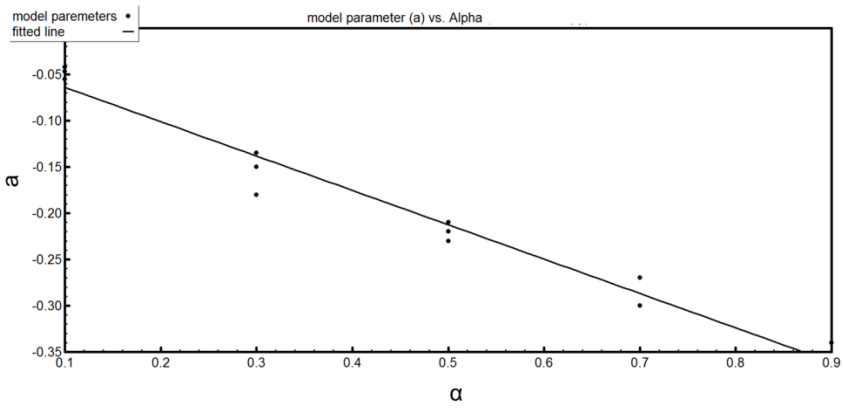

(a)

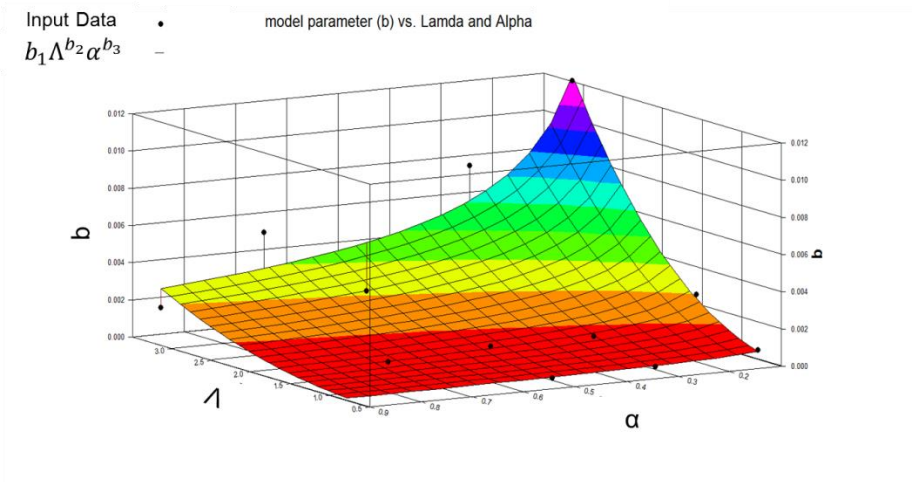

(b)

Figure C1 Curve-fitting for *a* and *b* model parameters for the flow resistance expression equation 3.9. (a) *a* versus α, (b) *b* versus α and Λ

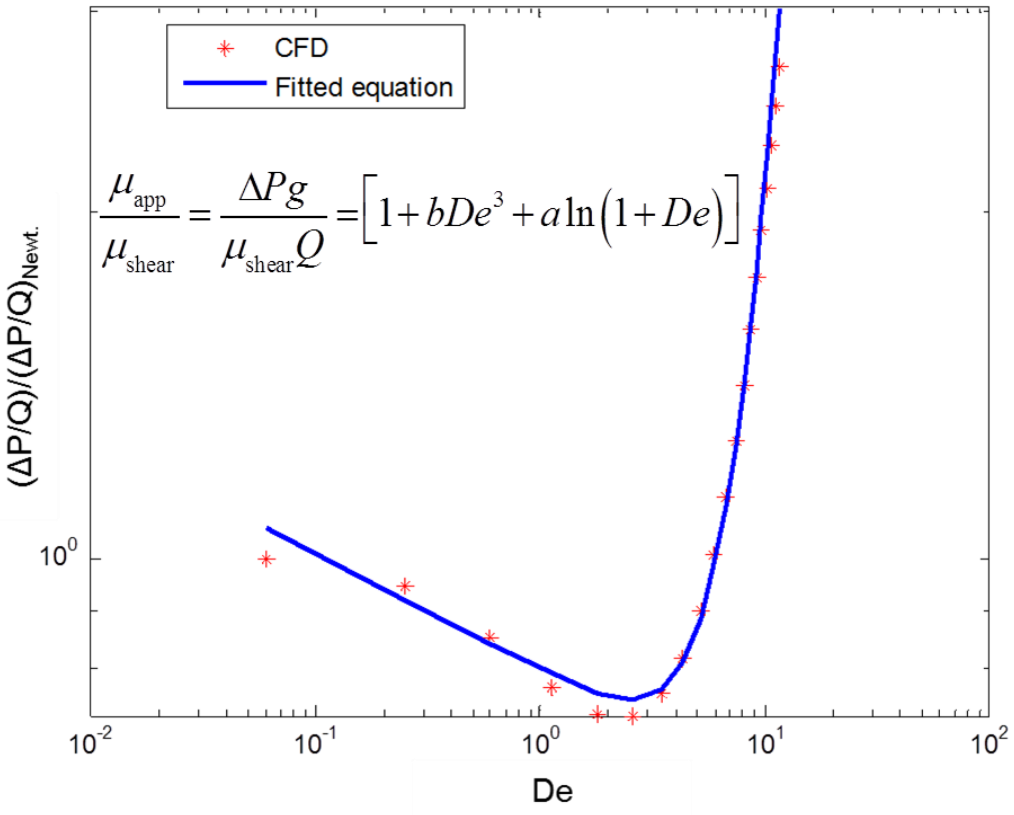

Figure C2 The fitted flow resistant expression equation 3.9 against CFD solutions for channel geometry with aspect ratio of α=0.5 and Λ=1.57

References

Adler, P. M., Jacquin, C. G., Thovert, J., 1992, "The formation factor of reconstructed porous media," Water Res. 28(6), 1571–1576

Adler, P. M.,, Thovert, J., Bekri, S., Yousefian, F. 2002, "Real Porous Media: Local Geometry and Transports," J. Engr Mech. 128(8), 829-839

Al-Gharbi, M. S., Blunt, M. J., 2005, "Dynamic Network Modeling of Two-Phase Drainage in Porous Media," Phys Rev E Stat Nonlin Soft Matter Phys. 71, 016308

Al-Raoush R., Thompson, K. E., Willson, C. S., 2003, "Comparison of Network Generation Techniques for Unconsolodated Porous Media," Soil Sci. Soc. Of America J. 67(6), 1687-1700

Aguayo, J. P, Tamaddon-Jahromi, H. R., Webster, M. F., 2010. "Excess Pressure-Drop Estimation in Contraction and Expansion Flows For Constant Shear-Viscosity, Extension Strain-Hardening Fluids," Journal of Non-Newtonian Fluid Mechanics

Balhoff, M., Thompson, K., 2004, "Modeling the Steady Flow of Yield-stress Fluids in Packed Beds," AIChE Journal, Vol. 50, Issue 12, 3034–3048

Balhoff, M., Thompson, K., 2006, "A Macroscopic Model for Shear-thinning Flow in Packed Beds Based on Network Modeling," Chemical Engineering Science, Vol. 61, Issue 2, 698-719

Balhoff, M. T., Wheeler, M. F., 2009, "A Predictive Pore Scale Model of Non-Darcy Flow in Porous Media," SPE J., vol. 14(4), 579-587

Balhoff, M.T., Schmidt, K., 2010 "Beyond Reluctance: Promoting Learning through an Unconventional Approach to Office Hours," Journal of Applications and Practices in Engineering Education, vo1(2), 55-69

Balhoff, M.T., Schmidt, Kathy, 2010 "Deeper Thinking: One Approach for Teaching Computer Programming to Undergraduates in Numerical Methods Courses", presented at the 2010 ASEE GSW Annual Conference, March

Bakke, S., Oren, P. E., 1997, "3-D Pore-scale Modelling of Sandstones and Flow Simulations in the Pore Networks," SPE J. 2(2), 136–149

Barnes, H. A., Hutton, J. F., Walters, K., 1989, "An Introduction to Rheology," Elsevier

Bird, R. B., Stewart, W. E., Lightfoot, E. N., 2006, "Transport Phenomena," revised second Edition, John Wiley & Sons, Inc.

Bear, J., 1972, "Dynamics of Fluids in Porous Media," Elsevier, New York

Binding, T. M., Phillips, P. M., Phillips, T. N., 2006, "Contraction/Expansion Flows: The Pressure Drop and Related Issue," J. Non-Newton. Fluid Mech. 137, 31–38

Bird, R. B., Armstrong, R. C., Hassager, O., 1987, "Dynamics of Polymeric Liquids," 2nd ed., Wiley, New York

Brooks, A. N., Hughes, T. J. R., 1982, "Streamline Upwind/Petrov-Galerkin Formulations for Convection Dominated Flows with Particular Emphasis on the Incompressible Navier-Stokes Equations," Comput. Methods Appl. Mech. Eng. 32, 199

Bryant, S. L., Mellor, D. W., Cade, C. A., 1993, "Physically Representative Network Models of Transport in Porous Media," AIChE Journal, 39, 387-396

Cannella, W. J., Huh, C., Seright, R., 1988, "Prediction of Xanthan Rheology in Porous Media," SPE 18089, proceedings of the 63rdAnnual Technical Conference and Exhibition, Houston, TX

Canic et al., 2006, "Blood Flow in Compliant Arteries: An Effective Viscoelastic Reduced Model, Numerics, and Experimental Validation," Annals of Biomedical Engineering, 34(4), 575-592

Carreau et al., 1979, "An Analysis of the Viscous Behaviour of Polymeric Solutions," Canadian Journal of Chemical Engineering, vol. 57, 135-140

Carreau, P. J., De Kee, D. C. R., Chhabra R. P., 1997, "Rheology of Polymeric Systems," Hanser/Gardner Publications, Inc., Cincinatti

Chambers, R. S., 1992, "Numerical Integration of the Hereditary Integrals in a Viscoelastic Model for Glass," J Am Ceram Soc. 75(8). 2213-2218

Chaveteau, G., Moam, M., 1981, J. Phys. - Lett. 42, 201

Chaveteau, G., 1986, "Fundamental Criteria in Polymer Flow through Porous Media: And Their Importance in the Performance Differences of Mobility-Control Buffers," Water-Soluble Polymers: Beauty with Performance, Advances in Chemistry Series, 227-267

Choi, H. (1991). Relaxtion Time of Polymer Solutions from Rod-Climbing Height. Korean Journal of Chemical Engineering, 8(1), 18–22.

Choi, H., Kim, H., 1992, "Relaxation time of polymer solutions from rod-climbing height (part 2)," Korean Journal of Chemical Engineering, 9(2), 74–82

Clemeur, N., Rutgers, R., Debbaut, B., 2003, "On the Evaluation of some Differential Formulations For The Pom-Pom Constitutive Model," Rheol Acta. 42(1), 217-231

Crochet, M. J., Delvaux, V., Marchal, J. M., 1990, J. Non-Newt. fluid Mech. 34, 261

Crochet, M. J., Legat, V., 1992, J. Non-Newt. fluid Mech. 42, 283

Deiber, J. A., Schowalter, W. R., 1979, "Flow Through Tubes with Sinusoidal Axial Variations in Diameter," AIChE Journal, Vol. 25, Issue 4, 638–645

Deiber, J. A., Schowalter, W. R., 1981, "Modeling the Flow of Viscoelastic Fluids through Porous Media," AIChE Journal, Vol. 27, Issue 6, 912–920

Delshad et al., 2008, "Mechanistic Interpretation and Utilization of Viscoelastic Behavior of Polymer Solutions for Improved Polymer-Flood Efficiency," SPE 113620-MS, SPE/DOE Symposium on Improved Oil Recovery, Tulsa, Oklahoma, USA

Demin, W., Jiecheng, C., Huifen, X., Qun, L., Jingping, S., 2001, "Viscous-Elastic Fluids Can Mobilize Oil Remaining after Water-Flood by Force Parallel to the Oil-Water Interface," SPE Asia Pacific Improved Oil Recovery Conference, Kuala Lumpur, Malaysia

Dias, M. M., Payatakes, A. C., 1986, "Network Models for Two-Phase Flow in Porous Media Part 1. Immiscible Microdisplacement of Non-Wetting Fluids," J. Fluid Mechanics, 164, 305-336

Duboin, Aurelien, 2013, "Écoulements de fluides complexes en presence d'interfaces dans des systèmes microfluidiques," PhD Dissertation, The University Pierre and Marie CURIE (UPMC)

Ehrenfried, D., 2013, "Impact of Viscoelastic Polymer on Residual Oil Saturation in Sandstones," MSc Thesis, The university of Texas at Austin

Flemming, P. D., 1983, "An Interpretation of the Petrophysical Properties of Reservoir Rocks Based on Percolation Theory," SPE 12515

Frenot, A., Chronakis, S., 2003, "Polymer Nanofibers Assembled by Electrospinning," Current Opinion in Colloid and Interface Science 8, 64–75

Guenette, R., Fortin, M., 1995, " A New Mixed Finite Element Method for Computing Viscoelastic Flows," Journal of Non-Newtonian Fluid Mechanics, 60, 27-52

Gupta, R. K., Sridhar, T., 1985, "Viscoelastic Effects in non-Newtonian flows through porous media," Rheologica Acta, 24, 148-151

Hayat, T., Shahzad F., Ayub M., 2007, "Analytical Solution for the Steady Flow of the Third

Grade Fluid in a Porous Half Space," Applied Mathematical Modelling 31, 2424–2432

Guénette, R., Fortin, M., 1995, "A new mixed finite element method for computing viscoelastic flow," J Non-Newtonian Fluid Mech., 60(1), 27-52

Heiba, A. A., Davis, H. T., Scriven, L. E., 1984, "Statistical Network Theory of Three-Phase Relative Permeabilities," SPE 12690, SPE/DOE Symposium on Enhanced Oil Recovery, Tulsa, Oklahoma, USA

Hughes, R. G., Blunt, M. J., 2000, "Pore Scale Modeling of Rate Effects in Imbibition," Trans. in Por. Media 40, 295-322

Huh, C., Pope, G. A., 2008, "Residual Oil Saturation from Polymer Floods: Laboratory Measurements and Theoretical Interpretation," SPE 113417, Improved Oil Recovery Symposium, Tulsa, Oklahoma, USA

Huifen, X., Demin, W., Junzheng, W., 2004, "Elasticity of HPAM Solutions Increases Displacement Efficiency Under Mixed Wettability Conditions," SPE Asia Pacific Improved Oil Recovery Conference, Perth, Australia

Inkson, N. J., McLeish, T. C. B., Harlen, O. G., Groves, D. J., 1999 "Predicting low density polyethylene melt rheology in elongational and shear flows with "pom-pom" constitutive equations," J Rheol., 43(4), 873-89

Joekar-Niasar, V., Hassanizadeh, S. M., Leijsne, A., 2008, "Insights into the Relationships among Capillary Pressure, Saturation, Interfacial Area, and Relative Permeability Using Pore-Newtok Modeling," Transport in Porous Media 74(2), 201-219

Joekar-Niasar, V., Hassanizadeh, S. M., Dahle, H. K., 2010a, "Non-Equilibrium Effects in Capillarity and Interfacial Area in Two-Phase Flow: Dynamic Pore-Network Modeling," J. Fluid Mech. 655, 38-71

Jones, D., Walters, K., Williams, P., 1987, "On the Extensional Viscosity of Mobile Polymer Solutions," Rheologica acta, 30, 20–30

Keunings, 2001, "Numerical Simulation of Branched Polymer Melts in Transient, Complex Flow using Pom-Pom Model," Journal of Non-Newtonian Fluid Mechanics, 97, 267-281

Kozicki, W., Kuang, P. Q., 1994, "Cake Filtration of Suspensions in Viscoelastic Fluids," The Canadian Journal of Chemical Engineering 72(5), 828–839

Kumar, V., 2014, Ansys Polyflow software Group, open discussion

Lake, L., 1989, "Enhanced Oil Recovery," Prentice Hall, New Jersey

Lekakou, C., Bader, M.G., 1998, "Mathematical Modelling of Macro- and Micro-infiltration in Resin Transfer Moulding (RTM)," Composites Part A, 29A, 29-37

Leonov, A. I., 1992, "Analysis of Simple Constitutive Equations for Viscoelastic Liquids," J Non-Newtonian Fluid Mech. 42. 323-350

Liang, Z., Ioannidis, A., Chatzis, I., 2000, "Permeability and Electrical Conductivity of Porous Media from 3D Replicas of the Microstructure," Chemical Engineering Science 55, 5247-5262

Lindquist, W. B., Lee, S., Coker, D. A., Jones, K. W., Spanne, P., 1996, "Medial Axis Analysis of Void Structure in Three-Dimensional Tomographic Images of Porous Media," Journal of Geophysical Research 101(B4), 8297–8310

Lindquist, W. B., Venkatarangan, A., Dunsmuir, J., Wong, T., 2000, "Pore and Throat Size Distributions Measured from Synchrotron X-ray Tomographic Images of Fontainebleau Sandstones," Journal of Geophysical Research 105 (B9), 21509-21528

Londergan, J. T., Meinardus, H. W., Manner, P. E., Jackson, R. E., Brown, C. L., Dwarakanath, V., Pope, G. A., Ginn, J. S., Taffinder, S., 2001, "DNAPL Removal from a Heterogeneous Alluvial Aquifer by Surfactant- Enhanced Aquifer Remediation," Ground Water Monitoring & Remediation, 21(3), 71-81

Lenormand, R., Touboul, E., Zarcone, C., 1988, "Numerical Models and Experiments on Immiscible Displacements in Porous Media," J. Fluid Mech. 189, 165-187

Lopez, X., Valvatne, P. H., Blunt, M. J., 2003, "Predictive Network Modeling of Single-Phase non-Newtonian Flow in Porous Media," J. Colloid Interface Sci., 264(1), 256

Lu, Y., 1994, "A Study of Residual Oil Saturation in Heterogeneous Sandstone Experiments," MS Thesis, University of Texas at Austin

Luo, X. L., Tanner, R. I., 1989, "A Decoupled Finite Element Streamline-Upwind Scheme for Viscoelastic Flow Problems," Journal of Non-Newtonian Fluid Mechanics, 31, 2, 143-162

Macosko, C. 1994, "Rheology: Principles, Measurements, and Applications," VCH Publishers, Minneapoils

Magueur, A., Moan, M., Chaveteau, G., 1985, "Effect of Successive Contractions and Expansions on the Apparent Viscosity of Dilute Polymer Solutions," Chem. Eng. Commun., vol. 36, 351-366

Man, H. N., Jing, H. D., 2000, "Pore-Network Modelling of Electrical Resistivity and Capillary Pressure Characteristics," Transport in Porous Media 41(3), 263-285

Marchal, J. M., Crochet, M. J., 1987, "A New Mixed Finite Element for Calculating Viscoelastic Flow," Journal of Non-Newtonian Fluid Mechanics, 26, Issue 1, 77–114

Marshall, R. J., Metzner, A. B., 1967, "Flow of Viscoelastic Fluids through Porous Media," Industrial and Engineering Chemistry Fundamentals, vol. 6, No. 3, 393-400

McLeish, T. C. B., Larson, R. C., 1988, "Molecular Constitutive Equations For a Class of Branched Polymers:The Pom-Pom Polymer," J Rheol., 42(1), 82-112

Metzner, A., White, J., Denn, M., 1966, "Constitutive Equations For Viscoelastic Fluids For Short Deformation Periods and For Rapidly Changing Flows: Significance of The Deborah Number," AIChE Journal, 12(5), 863–866

Nigen, S., Walters, K., 2002, "Viscoelastic Contraction Flows: Comparison of Axisymmetric And Planar Configurations," J. Non-Newton. Fluid Mech., 102, 343–359

Ostwald, W., 1925, "Uber die Geschwindigkeits funktion der Viskositat Disperser Systeme," Kolloid-Zeitschrift 36, 99-117

Park, H. C., 1972, "The Flow of Non-Newtonian Fluids through Porous Media," Ph.D. Thesis, Department of Chemical Engineering, Michigan State University

Peters, E. J., 2012, "Advanced Petrophysics"

Preziosi, L., Joseph, D., Beavers, G., 1996, "Infiltration of Initially Dry, Deformable Porous Media," Int. Journal of Multiphase Flow, 22(6), 1205-1222

Putz, A. G., Lecourtier, J. M., Bruckert, L., 1988, "Interpretation of High Recovery Obtained in a New Polymer Flood in the Chateaurenard Field," SPE 18093, SPE 63rd Annual Technical Conference and Exhibition, Houston, Texas, USA

Rajagopalan, D., 1990, "Finite Element Methods for Calculation of Steady, Viscoelastic Flow using Constitutive Equations with a Newtonian Viscosity," Journal of Non-Newtonian Fluid Mechanics, 36, 159–192

Reeves, P. C., Celia, M. A., 1996, "A Functional Relationship between Capillary Pressure, Saturation, and Interfacial Area as Revealed by a Pore-Scale Network Model," Water Resources Research, 32, 2345-2358

Rojas, H., 2007, "Numerical Implementation of Viscoelastic Blood Flow in a Simplified Arterial Geometry," Medical Engineering and Physics, 29, 491-496

Roylance, D., 2001, "Engineering Viscoelasticity," Cambridge, MA 02139: Massachusetts Institute of Technology

Rubinstein, M., Colby, R., 2003, "Polymer Physics," Oxford University Press.

Sadowski, T. J., 1963, "Non-Newtonian Flow through Porous Media," Ph.D. Thesis, University of Wisconsin, Madison

Sahimi, M., 1993, "Nonlinear Transport Processes in Disordered Media," AIChE J., 39(3), 369

Schaefer, C. E., Dicalro, D. E., Blunt, M. J., 2000, "Experimental Measurement of Air-Water Interfacial Area during Gravity Drainage and Secondary Imbibitions in Porous Media," Water Resources Research. 36(4), 885-890

Seright, R.S., Seheult, M., Talashek, T., 2008, "Injectivity Characteristics of EOR Polymers," SPE Annual Technical Conference and Exhibition, Denver, Colorado, USA

Shah, C. B., Kharabaf, H., Yortsos, Y. C., 1995, "Flow and Displacement of Bingham Plastics in Porous Media," presented at Proc. Unitar Conf. On Heavy Oils and Tar Sands, Houston, Texas

Shah, C. B., Yortsos, Y. C., 1995, "Aspects of Flow of Power-Law Fluids in Porous Media," AIChE J., 41, 1099

Shah, C. B., Kharabaf, H., Yortsos, Y. C., 1998, "Immiscible Displacements Involving Power-Law Fluids in Porous Media," presented at Proc. Unitar Conf. On Heavy Oils and Tar Sands, Beijing, China

Simhambhatla, M., Leonov, A. I., 1995, "On the Rheological Modeling of Filled Polymers with Particle-Matrix Interactions," Rheol Acta., 34, 329-338

Simhambhatla, M. V., 1994, "The Rheological Modeling of Simple Flows of Unfilled and Filled Polymers," PhD Thesis, University of Akron, Akron, Ohio

Skartis, L., Kohomani, B., Kardos, J., 1992, "Polymeric Flow through Fibrous Media," Journal of Rheology, 36(4), 589-619

Sochi, T., Blunt, M. J., 2008, "Pore-Scale Network Modeling of Ellis and Herschel–Bulkley Fluids," Journal of Petroleum Science and Engineering, Vol. 60, Issue 2, 105-124

Sochi, T., 2009, “Pore-Scale Modeling of Viscoelastic Flow in Porous Media Using a Bautista–Manero Fluid,” International Journal of Heat and Fluid Flow, 30, 1202–1217

Solomon, M. J., Muller, S. J., 1996, “The Transient Extensional Behavior of Polystyrene-Based Boger Fluids of Varying Solvent Quality and Molecular Weight”, Soc. Rheol., 40(5), 837-856

Sorbie, K. S., Clifford, P. J., Jones, E. R. W., 1989, “The Rheology of Pseudoplastic Fluids in Porous Media Using Network Modeling,” J.Colloid Interf. Sci., 130, 508

Sorbie, K. S., 1991, “Polymer-Improved Oil Recovery,” Blackie, Glasgow and London

Sridhar, T., Tirtaatmadja, V., Nguyen, D. A., Gupta, R. K., 1991, ‘‘Measurement of Extensional Viscosity of Polymer Solutions,’’ J. Non-Newt. Fluid Mech., 40, 271–280

Thurston, G., 1974, “Elastic Effects in Pulsatile Blood Flow,” Microvascular Research, V9

Thompson, K. E., 2002, “Pore-scale Modeling of Fluid Transport in Disordered Fibrous Materials,” 48(7), 1369-1389

Valvatne, P. H., Blunt, M. J., 2003, “Predictive Pore-Scale Modeling,” SPE 84550

Van Schaftingen, J. J., Crochet, M. J., 1984, “A Comparison of Mixed Methods for Solving the Flow of a Maxwell Fluid,” International Journal of Numerical Methods Fluids, 4, 1065-1081

Vogel, P., Pusch, G., 1981, “Some Aspects of the Injectivity of Non- Newtonian Fluids in Porous Media,” Proceedings of the First European Symposium on EOR in Bournemouth, UK

Wang, D., Cheng, J., Xia, H., Li, Q., Shi, J., 2001, "Viscous-Elastic Fluids Can Mobilize Oil Remaining after Water-Flood by Force Parallel to the Oil-Water Interface,” Kuala Lumpur, Malaysia

Wilkinson, D., Willemsen, J. F., 1983, “Invasion Percolation: A New Form of Percolation Theory,” J. Phys. A 16, 3365-3376

Willhite, G. P., Green, D. W., 1998, “Enhanced Oil Recovery,” first edition, SPE text book series, Richardson, Texas

Wissler H. E., 1971, “Viscoelastic Effects in the Flow of Non-Newtonian Fluids through a Porous Medium,” Industrial and Engineering Chemistry Fundamentals, vol. 10, No. 3, 411-417

Wreath, D. G., 1989, "A Study of Polymer Flooding and Residual Oil Saturation," M.S. Thesis, University of Texas at Austin

Yin et al., 2006, “Study on Flow Behaviors of Viscoelastic Polymer Solution in Micropore with Dead End,” SPE 101950-MS, SPE Annual Technical Conference and Exhibition, San Antonio, Texas, USA

Yuan, M., 1981, “A Rheological Study of Polymer and Microemulsion in Porous Media” MS Thesis, University of Texas at Austin